
Studies of Optical Wireless Communications: Random Orientation Model, Modulation, and Hybrid WiFi and LiFi Networks

Ardimas Andi Purwita



A thesis submitted for the degree of Doctor of Philosophy.
The University of Edinburgh.
October 30, 2020

Lay Summary

This thesis' primary goal is to quantify the contribution of light fidelity (LiFi) in hybrid WiFi and LiFi networks. Hybrid WiFi and LiFi networks are wireless technologies that combine both a radio frequency (RF) communication and LiFi, which is an optical wireless communication (OWC) technology. The study of LiFi's contribution is important as future wireless networks, such as 5G, envision hybrid networks to mitigate the lack of RF spectrum required to accommodate an increasing number of users. LiFi is a great candidate to accompany RF communications, as the optical spectrum is an unlicensed spectrum, and LiFi does not interfere with RF communications. Moreover, WiFi has been carrying most of the global mobile traffic for the last few years, and more mobile data is predicted to be transferred over WiFi in the future. Therefore, this thesis aims to determine how many bytes of data that LiFi carries compared to the total bytes that is generated by hybrid WiFi and LiFi networks. This ratio is referred to as an offloading efficiency.

In order to get an accurate result, realistic models need to be made first. LiFi channel models are first investigated; for example, a random orientation model of mobile devices is required to capture users' random behavior. Similarly, a random blockage model is also important and considered, as opaque objects block LiFi signals. The modulation technique is chosen based on the ongoing LiFi standardization, i.e., IEEE 802.11bb, which is part of the IEEE 802.11 WiFi working group. With the help of an emulation tool from the Linux operating system, large virtual hybrid networks that are connected to real website servers, can be emulated. By using these methods, the offloading efficiencies are calculated over many realizations for different scenarios. For a residential scenario, the offloading efficiency is 64.54%. Meanwhile, for an enterprise scenario, the offloading efficiency is 75.85%. These offloading efficiencies show that LiFi can play an important role in future hybrid networks.

Abstract

Cisco has predicted that by 2022, as a result of the emerging internet-of-things traffic, there will be an internet protocol (IP) traffic explosion. An increasing amount of radio frequency (RF) spectra has been allocated to accommodate this mobile data surge, such as the recently allocated sub 6 GHz band for WiFi. A further prediction is that by the year 2035, all RF spectra will be fully utilized. This means there is a need for additional spectrum, such as the optical spectrum. One vision of future wireless networks is to aggregate multiple wireless access technologies. For example, optical wireless communications (OWC) that have narrow coverage, but a very high area spectral efficiency, can potentially complement RF communications to provide a higher peak data rate. A hybrid WiFi and light fidelity (LiFi) network is one of these examples. Compared to other OWC technologies, such as visible light communications or optical camera communications, LiFi supports bidirectional and multi-user communications. These features are also the main features of WiFi, and WiFi is predicted to carry the majority of global mobile data traffic in the future. Based on this prediction, the primary question in this thesis is how much LiFi supports WiFi in efficiently handling mobile data traffic in hybrid WiFi and LiFi networks. This is answered by calculating an offloading efficiency, which is the ratio of data that is transferred over LiFi compared to the total data.

Even with the current advancements in LiFi, a few intermediate studies are needed.

- The first contribution of this thesis is to model randomly-oriented mobile devices. A random orientation is needed in order to capture users' behavior while they move and operate mobile devices. In addition, a random blockage model must be investigated as LiFi signals can be blocked by opaque objects. The main purpose of considering the random orientation and random blockage models is to ensure that the offloading efficiency is evaluated by using realistic assumptions.
- The second contribution of this thesis fall under studies of single-carrier and multi-carrier modulations. The conventional pulse amplitude modulation and single-carrier with frequency domain equalization (PAM-SCFDE) is improved by adding non-linear filters or index modulation. In the low-to-moderate spectral efficiency region, up to 3 dB gain can be achieved by means of these improvements. In the high spectral efficiency region, an

Abstract

orthogonal frequency division multiplexing (OFDM)-based system, which is based on the common mode of the physical (PHY) layer of the ongoing LiFi standardization, i.e., IEEE 802.11bb, is used. By exploiting the fact that the wireless optical channel has a low-pass filter characteristic, an in-phase and quadrature wavelength division division multiplexing (IQ-WDM) system that uses the PHY of IEEE 802.11bb is proposed. Up to 2 dB gain can be obtained by IQ-WDM compared to the common mode PHY of IEEE 802.11bb.

- For the final contribution of this thesis, the OFDM system from IEEE 802.11bb is abstracted to emulate large-scale networks and to calculate the offloading efficiency. A real transport control protocol (TCP)/IP stack, which has multipath TCP (MPTCP) to support multi-connectivity between WiFi and LiFi networks, is also deployed to emulate real traffic. By calculating the offloading efficiency with such methodology over many channel realizations considering the proposed random orientation and blockage models, average offloading efficiencies of 64.54% and 75.85% are obtained for residential and enterprise scenarios, respectively. These results show the significant potential of OWC to complement RF communications.

Declaration of Originality

I hereby declare that the research recorded in this thesis and the thesis itself was composed and originated entirely by myself in the Institute for Digital Communications School of Engineering at The University of Edinburgh.

Ardimas Andi Purwita

Edinburgh, UK

October 30, 2020

Acknowledgements

First and foremost, praise is to ALLAH, the Almighty, on whom I rely for the guidance and His mercy. May also the peace and blessing be upon the noblest Prophet Mohammad, his family, and all of his companions.

I would also like to express my gratitude to my parents. They are so far, yet their support feels so close and warm.

This thesis would never be finished without the help of my wife (Nanda), my son (Rayhan), and my daughter (Raisha). A thousand legos, boxes of skin conditioners, and any spoken word are not enough to express how grateful I am, having you three by my side.

I would also like to thank Prof. Haas for his inspiring words and tolerance. (I know that I am not always on my best behavior and performance.)

I am also grateful for having Dr. Safari as my second supervisor and an engaging discussion partner.

I would also like to thank Hannah Brown for all her helps. I thank my friends and colleagues in the LiFi R&D Center, e.g., Anil, Tezcan, Cheng, Yinzhou, Rui, Mohammad, Mohamed, *et al.*

Last but not least, I would like to express my appreciation to the Indonesian Ministry of Finance for granting me as an awardee of the Indonesia Endowment Fund for Education (LPDP). Indeed, I could not have enjoyed my studies and life in Edinburgh without the funding.

Contents

Lay Summary	ii
Abstract	iii
Declaration of Originality	v
Acknowledgements	vi
Contents	vii
List of Figures	x
List of Tables	xiv
Acronyms and Abbreviations	xv
List of Principal Symbols	xx
1 Introduction	1
1.1 Motivations	1
1.2 Contributions and Thesis Layout	3
1.3 Publication Lists	5
1.4 Summary	8
2 LiFi Channel and System Models	11
2.1 Introduction	11
2.2 LiFi Channel Model	12
2.2.1 Transmitter Model	13
2.2.2 Optical Wireless Channel Model	13
2.2.3 Receiver Model	15
2.3 LiFi System Model	16
2.3.1 Frontend Model	16
2.3.2 Channel Model	19
2.3.3 A Simple Office Environment	21
2.4 Summary	23
3 Random Orientation Model	25
3.1 Introduction	25
3.2 Contributions of This Chapter	26
3.3 Related Works	26
3.4 Data Collection and Assumptions	28
3.5 Random Orientation Model	30
3.5.1 Noise Estimation: n_θ and n_ω	30
3.5.2 Tilted Angle Estimation: μ_θ	31
3.5.3 Small-Signal Estimation: θ_0 and ω_0	32
3.6 Coherence Time of Indoor LiFi Channels	35
3.6.1 System Model	35
3.6.2 Simulation Environments	36
3.6.3 Specific Case: A Realization of A User's Random Mobility	37
3.6.4 Coherence Time of The Specific Case	42

3.6.5	Results and Discussions	45
3.7	Summary	48
4	Modulation: Single-Carrier and Multi-Carrier	49
4.1	Introduction	49
4.2	Contributions of This Chapter	50
4.3	Related Works	51
4.4	Improving PAM-SCFDE with Non-Linear Equalizers	52
4.4.1	Linear Region of Light Emitters	53
4.4.2	PAM-SCFDE with LE	53
4.4.3	PAM-SCFDE with LE and DFE	57
4.4.4	PAM-SCFDE with LE and THP	57
4.4.5	MMSE-Based Equalizers	60
4.5	SC-GTIM: PAM-SCFDE with IM	64
4.5.1	Motivations	64
4.5.2	Transmission Model	65
4.5.3	Construction of a Good Set $\mathcal{S}^{\text{GTIM}}$	70
4.6	IEEE 802.11bb-Compliant OFDM Systems	84
4.6.1	The Common Mode of IEEE 802.11bb	84
4.6.2	IQ-WDM	86
4.7	Performance Comparison	88
4.8	Summary	90
5	Hybrid WiFi-LiFi: Determining the LiFi Offloading Capability	91
5.1	Introduction	91
5.2	Contributions of This Chapter	92
5.3	Related Works	92
5.4	Problem Formulation	94
5.5	Channel Model	95
5.5.1	Scenario	95
5.5.2	WiFi Channel Model	96
5.5.3	LiFi Channel Model	98
5.6	Traffic Model	98
5.7	Link-to-System Mapping	101
5.8	Performance Evaluation	103
5.9	Summary	105
6	Conclusions and Future Research	109
6.1	Conclusions	109
6.2	Future Research	111
A	owcsimpy: A Library for Generating Wireless Optical CIRs	115
A.1	Introduction	115
A.2	Key Features of <code>owcsimpy</code>	116
A.3	Generating Geometry Models	118
B	Brief Overview of Lomb-Scargle Periodograms	121

C Brief Overview of the IEEE 802.11ax	123
C.1 Introduction	123
C.2 Features	123
References	125

List of Figures

2.1	Responsivities of four different Silicon-based photodiodes (PDs) taken from [Edmund Optics®, 2020]. (Please refer to [Edmund Optics®, 2020] for more detailed information on the corresponding curves. Note that details are removed for clarity purposes.)	12
2.2	A transceiver model of IM/DD systems.	12
2.3	A transmitter model.	14
2.4	(a) The partitioning of an arbitrary 2D plane into smaller planes, and (b) the geometry model.	14
2.5	A receiver model.	16
2.6	(a) Measurement setup for the Tx frontend, and (b) the Tx frontend model. Note that DSP stands for digital signal processor and VGA stands for variable gain amplifier.	17
2.7	A bandpass magnitude response of the Tx frontend model based on a 30mW LC850-0030AR VCSEL (850 nm), where the red dashed lines show the cutoff frequencies, i.e., 2.6×10^5 Hz and 2.34×10^8 Hz.	17
2.8	(a) Measurement setup for the Rx frontend, and (b) the Rx frontend model. Note that AGC stands for automatic gain controller.	18
2.9	A bandpass magnitude response of the Rx frontend model based on SAR1500H4 Si APD, where the red dashed lines show the cutoff frequencies, i.e., 4.8×10^4 Hz and 2.6×10^8 Hz.	18
2.10	The $P - I$ curve of the 30mW LC850-0030AR VCSEL.	18
2.11	(a) An example of a 3D object as a collection of 2D faces, and (b) a human model as a collection of square faces.	20
2.12	Illustration of blockage event in <code>owcsimpy</code> for a link between two red planes and a blocking object, i.e., the black plane.	21
2.13	(a) A 3D model of a small office environment, and (b) its corresponding model used in <code>owcsimpy</code>	21
2.14	Three different realizations of a small office environment.	23
2.15	CIRs of configurations shown in Figure 2.14.	24
3.1	An illustration of human models using their mobile devices in a position that is not directly facing upwards.	25
3.2	Definitions of orientation of a mobile device using spherical coordinates, and activities that are carried out by the participants.	28
3.3	An illustration of the components of the noisy measurement $m_\theta(t)$, i.e., μ_θ , $\theta_0(t)$, and $n_\theta(t)$	29
3.4	Samples of noisy measurement: (a) $m_\theta(t)$ and (b) $m_{\omega \tilde{\omega}}(t)$ for the sitting activity, (c) $m_\theta(t)$ and (d) $m_{\omega \tilde{\omega}}(t)$ for the walking activity.	30
3.5	A sample of noise measurements for (a) $n_\theta(t)$ and for (b) $n_\omega(t)$	31

3.6 (a) PSD of the sample shown in Figure 3.5(a), and (b) PSD of the sample shown in Figure 3.5(b). The red curves are generated by taking the averages of periodograms of many zero-mean white noises with the variances of 0.0011 and 1.0257, respectively.	31
3.7 PDFs of μ_θ for each activity, where μ and σ denote the mean and the standard deviation, respectively.	32
3.8 (a) The power spectrum of a window function taken from one of the $m_\theta(t)$ measurements from the sitting activity. (b) The power spectrum of the corresponding data.	33
3.9 (a) A PS of the measurement whose PS is shown in Figure 3.8(b) after being filtered. (b) Its corresponding autocorrelation function.	33
3.10 (a) The reading activity and (b) the calling activity.	37
3.11 (a) A geometry model for the open office environment. The red human model represents the user of interest doing a calling activity. (b) The top view of the open office environment, where the pink area illustrates the mobility area of people.	38
3.12 (a) A realization of random mobility in the small office environment. (b) The corresponding speed vs. time graph. (c) LoS of the CIR.	39
3.13 (a) Another realization for a comparison with Figure 3.12(a). (b) The corresponding speed vs. time graph. (c) LoS of the CIR.	40
3.14 The discrete-time channel impulse responses (CIRs) (DTCIRs) w.r.t. the mobility sample shown in Figure 3.12(a) with (a) $B = 20$ MHz and (b) $B = 80$ MHz.	41
3.15 Normalized magnitude response of wireless optical channel corresponded to the mobility sample shown in Figure 3.12(a).	41
3.16 Collinearity of the discrete-time CIRs shown in Figure 3.14(a), i.e., $B = 20$ MHz.	44
3.17 Collinearities at different time instances, i.e., (a) $t = 0.25$ s and (b) $t = 1.27$ s. The shaded areas denote T_{stat} , where $T_{\text{stat}} = 0.359$ s for (a) and $T_{\text{stat}} = 0.608$ s.	45
3.18 (a) The stationary time, and (b) its CDF.	45
 4.1 The comparisons of different modulation techniques at different spectral efficiencies taken from [Nuwanpriya <i>et al.</i> , 2015].	50
4.2 An abstraction of linear region, where the black line with a shaded region denotes the linear region, and the red lines denotes the non-linear curves.	53
4.3 Pulse amplitude modulation (PAM)-single-carrier with frequency domain equalization (SCFDE) with linear equalizer (LE).	54
4.4 The block diagram of the channel matrix \mathbf{H} , which models: a cyclic prefix (CP) addition block, a parallel-to-serial (P/S) conversion, a CIR of a transmitter's frontend $h_{\text{txfe}}(t)$, a laser diode (LD) ($h_{\text{ld}}(t)$), a light fidelity (LiFi) CIR ($h_{\text{woc}}(t)$), a PD ($h_{\text{pd}}(t)$), a transimpedance amplifier (TIA) ($h_{\text{tia}}(t)$), a CIR of a receivers's frontend ($h_{\text{rxf}}(t)$), a serial-to-parallel (S/P) conversion, and a CP removal block.	56
4.5 PAM-SCFDE with LE and decision feedback equalization (DFE).	58
4.6 PAM-SCFDE with LE and Tomlinson-Harashima precoder (THP).	58
4.7 The modulo operation for the THP system.	58
4.8 An equivalent model for THP.	59

4.9	The system model of SC-generalized time index modulation (GTIM).	65
4.10	The working principle of $f_{S^{\text{SCTIM}}}$ with (4.29).	67
4.11	Vector representations: (a) SC-PAM with $M = 2$ and the Gray code and without index modulation (IM) ($\eta = 1$), (b) SC-time index modulation (TIM) with $K = 1$ and $J = 2$ ($\eta = 1$) and (c) SC-GTIM with $J = 2$ ($\eta = 1$). The circle markers show the symbols that can be chosen and labeled with binary vectors. The other markers show the chosen symbols.	69
4.12	(a) The first, (b) the second and (c) the third steps of the set partitioning algorithm.	73
4.13	$\text{SP}(\cdot)$ with: (a) $M = 3, B = 3$ and $\eta = 1.5$; (b) $M = 3, B = 4$ and $\eta = 2$; (c) $M = 4, B = 4$ and $\eta = 2$; (d) $M = 5, B = 5$ and $\eta = 2.5$	78
4.14	An illustration for the proposed algorithm with $(3, 6, 3, 2)$	80
4.15	(a) An output of Algorithm 1 with $(4, 4, 2, 1)$ and (b) a modified construction of Figure 4.13(c) if $ m_0 - I_0 < m_i - m_j , \forall i \neq j \in \{0, 1, \dots, M - 1\}$	81
4.16	BER comparisons of single carrier modulation systems with respect to the scenarios depicted in Figure 2.14(a) and Figure 2.14(c).	83
4.17	The mandatory PHY of IEEE 802.11bb: frequency up-and-down conversion method.	85
4.18	The spectrum mask of the IEEE 802.11ax orthogonal frequency-division multiplexing (OFDM) waveform [IEEE P802.11 TGax, 2018]. B denotes the signal bandwidth, where $B \in \{20, 40, 80, 160\}$ MHz.	86
4.19	The normalized magnitude responses of the CIRs shown in Figures 2.15(b), (d), and (f).	87
4.20	PERs of PHY of IEEE 802.11bb over the channel depicted in Figure 4.18 for case 3, 64-QAM, and the coding rate of 3/4. Note that the PER performance of IQ-WDM is	87
4.21	Aliasing phenomenon of the PHY common mode IEEE 802.11bb.	87
4.22	The block diagram of in-phase and quadrature (IQ)-wavelength division multiplexing (WDM).	88
4.23	Performance comparisons of different modulation techniques at BER of 10^{-5}	89
5.1	(a) The residential scenario: a five-story building with 2×10 apartments in each floor, and the dimensions of each apartment are $10 \text{ m} \times 10 \text{ m} \times 3 \text{ m}$. (b) The enterprise scenario that comprises 8 offices whose dimensions are $20 \text{ m} \times 20 \text{ m} \times 3 \text{ m}$ per office.	95
5.2	(a) A floor plan of a realization of the interior of an apartment in the residential scenario. (b) A floor plan of a realization of the interior of an office in the enterprise scenario. (c) The 3D realization of the apartment using <code>owcsimpy</code> . (d) The 3D realization of the office using <code>owcsimpy</code>	97
5.3	The ON-OFF model for modeling the web traffic.	99
5.4	A description to emulate traffic models.	100
5.5	The PHY link-to-system mapping work flow.	101
5.6	Link level simulations for the residential scenario: simulated vs. abstracted. Note that the abstraction scenario refers to the use of the effective signal-to-interference-plus-noise ratio (SINR) mapping (ESM) function.	103
5.7	Link level simulations for the enterprise scenario: simulated vs. abstracted. Note that the abstraction scenario refers to the use of the ESM function.	104

5.8	(a) A sample of realizations in the residential scenario, where the legends of the mobility of the user follows those of Figure 3.12 and Figure 5.2. The laptop and phone icons show the existence of other users in the sample. (b) The measured data rate of the mobile user.	105
5.9	Average data rate (Mbps) in: (a) the residential scenario for the LiFi networks, (b) the residential scenario for the WiFi networks, (c) the enterprise scenario for the LiFi networks, and (d) the enterprise scenario for the WiFi networks.	106
5.10	Offloading efficiency.	106
6.1	An aircraft cabin model that can be modeled by <code>owcsimpy</code>	111
6.2	The emulated image that is captured by one of the closed-circuit televisions (CCTVs).	112
A.1	Description of <code>owcsimpy</code> v0.0.1. Note: attr. is short for attributes, and geo. is short for geometry.	117
A.2	(a) An example of the Delaunay triangulation to an arbitrary 3D object, and (b) a blocky and pixelated human model.	118
A.3	An example of a cuboid whose sides are partitioned into 2×2 planes.	119
A.4	(a) A 3D model of a small office environment, and (b) its corresponding model used in <code>owcsimpy</code>	119

List of Tables

2.1	Reflectivities of materials over visible light (VL) and infrared (IR) spectrum.	22
3.1	Average values of the estimated parameters $\{A, f, \sigma_v\}$ in (3.4) and (3.5).	34
3.2	Coherence time of the small office environment.	46
3.3	Coherence time of the open office environment.	47
4.1	Optimal filters for PAM-SCFDE with LE, DFE, and THP.	62

Acronyms and Abbreviations

3GPP	3 rd generation partnership project
ACF	autocorrelation function
ACO	asymmetrically clipped optical
ADC	analog-to-digital converter
AGC	automatic gain controller
AP	access point
APD	avalanche photodiode
ATSSS	access traffic steering, switching and splitting
AWGN	additive white Gaussian noise
BER	bit error ratio
CAD	computer-aided design
CCTV	closed-circuit television
CDF	cumulative distribution function
CIR	channel impulse response
CLI	command-line interface
CSMA/CA	carrier sense multiple access with collision avoidance
CP	cyclic prefix
DASH	dynamic adaptive streaming over hypertext transfer protocol
DAC	digital-to-analog converter
DC	direct current
DFE	decision feedback equalization
DFT	discrete Fourier transform
DPSS	discrete prolate spheroidal sequences
DSP	digital signal processor
DQO	decomposed quadrature optical
eU	enhanced unipolar
E/O	electrical-to-optical
EESM	exponential effective signal-to-interference-plus-noise ratio metric
ESM	effective signal-to-interference-plus-noise ratio mapping

FCC	federal communications commission
FDE	frequency-domain equalization
FEC	forward error correction
FFT	fast fourier transform
FIR	finite impulse response
FoV	field-of-view
FST	fast session transfer
FTP	file transfer protocol
FWHM	full width at half maximum
GTIM	generalized time index modulation
HetNets	heterogeneous networks
HPF	high-pass filter
HTML	hypertext markup language
HE	high efficiency
HTTP	hypertext transfer protocol
IaaS	infrastructure as a service
IDFT	inverse discrete Fourier transform
IEC	International Electrotechnical Commission
IEEE	Institute of Electrical and Electronics Engineers
IID	identically independently distributed
IM	index modulation
IM/DD	intensity modulation and direct detection
IP	internet protocol
IQ	in-phase and quadrature
IR	infrared
ISI	inter-symbol interference
ITU-T	International Telecommunication Union - Telecommunication Standardization Sector
KSD	Kolmogorov-Smirnov distance
LC	light communications
LD	laser diode
LDPC	low-density parity-check
LE	linear equalizer
LED	light emitting diode

LiFi	light fidelity
LoS	line of sight
LPF	low-pass filter
LSB	least significant bit
LSF	local scattering function
LSSA	least-squares spectral analysis
LTI	linear time-invariant
LUT	lookup table
MAC	medium access control
MCS	modulation and coding scheme
MIESM	mutual information effective signal-to-interference-plus-noise ratio metric
MIMO	multiple-input, multiple-output
MMSE	minimum mean square error
MPDU	MAC protocol data unit
MPTCP	multipath transmission control protocol
MSB	most significant bit
MSE	mean square error
NIC	network interface card
OAM	orbital angular momentum
OOC	optical camera communications
OFDM	orthogonal frequency-division multiplexing
OFDMA	orthogonal frequency-division multiple access
OOK	on-off-keying modulation
OOP	object-oriented programming
O/E	optical-to-electrical
OWC	optical wireless communications
PAM	pulse amplitude modulation
PAPR	peak-to-average power ratio
PD	photodiode
PDF	probability density function
PEP	pairwise-error probability
PER	packet error ratio
PHY	physical

PIN	positive-intrinsic-negative photodiode
PM	position modulating
PPM	pulse position modulating
PPDU	physical layer convergence procedure protocol data unit
P/S	parallel-to-serial
PS	power spectrum
PSD	power spectral density
QAM	quadrature amplitude modulation
RBIR	received bit mutual information rate
RCO	repetition and clipping optical
RF	radio frequency
RP	random process
RU	resource unit
RTSP	real-time streaming protocol
RV	random variable
RWP	random waypoint
SCFDE	single-carrier with frequency domain equalization
SDN	software-defined networking
SIC	successive interference cancellation
SIFS	short inter frame space
SISO	single-input and single-output
SINR	signal-to-interference-plus-noise ratio
SM	spatial modulation
SNR	signal-to-noise ratio
STA	station
S/P	serial-to-parallel
TCP	transmission control protocol
TGax	IEEE 802.11 High Efficiency - Task Group “ax”
TGbb	IEEE 802.11 Light Communications Amendment - Task Group “bb”
THP	Tomlinson-Harashima precoder
TIA	transimpedance amplifier
TIM	time index modulation
VCSEL	vertical-cavity surface-emitting laser

VGA	variable gain amplifier
VL	visible light
VLC	visible light communications
VLP	visible light positioning
VPN	virtual private network
USB	universal serial bus
WDM	wavelength division multiplexing
WMF	whitened matched filter
WOC	wireless optical channel
WOCIR	wireless optical channel impulse response
WSS	wide-sense stationary
WSSUS	wide-sense stationary uncorrelated scattering

List of Principal Symbols

$\ \cdot\ _2$	L2-norm
$\mathbb{1}(\cdot)$	indicator function
$\delta[n]$	dirac delta function
γ	collinearity
ε	elemental object
ε^s	elemental source
ε^r	elemental receiver
λ	wavelength
μ_θ	mean of $m_\theta(t)$
μ_ω	mean of $m_\omega(t)$
ϕ	random phase
$\Phi_{1/2}$	the half-power semiangle of emitters
Ψ_c	field-of-view
ρ	reflectivity
\mathcal{R}	receiver element
\mathcal{S}	source element
ω	azimuth angle
σ_{shot}	standard deviation of a shot noise
θ	polar angle
A	detection ares
\mathbf{b}	binary vector
\mathbf{B}	feedback matrix
d_{ij}	distance of the i^{th} point and the j^{th} point
\mathbf{d}	input information vector
\mathbf{e}	error vector
$\mathbb{E}[\cdot]$	the expectation operation
E_b	energy per bit
E_s	energy per symbol
\mathbf{F}	feed-forward filter

f_c	center frequency
f_s	one-to-one mapping
f_{samp}	sampling frequency
f_{sym}	symbol rate
f_{rx}	mapping function at a transmitter
f_{tx}	mapping function at a transmitter
$h(t)$	optical wireless channel impulse response
$h_c(\tau, t)$	channel impulse response at time t to an impulse input transmitted at $t - \tau$
$h_d[l, n]$	discrete-time channel impulse response
H_{tx}	frequency response of an analog front-end at a transmitter
H_{rx}	frequency response of an analog front-end at a receiver
H	channel matrix
I_a	lower limit of a linear region
I_b	higher limit of a linear region
L	local scattering function estimator
L_{cp}	the cyclic-prefix length
m	the generalized Lambertian pattern mode
$m_\theta(t)$	noisy measurement with respect to the polar angle
$m_\omega(t)$	noisy measurement with respect to the azimuth angle
$\text{mod}(\cdot)$	modulo operation
$n(t)$	thermal noise
p	position vector
n	normal vector
$n_\theta(t)$	noise of measurement with respect to the polar angle
$n_\omega(t)$	noise of measurement with respect to the azimuth angle
N_0	single-sided power spectral density of a white noise
$p_t(t)$	pulse shaping at a transmitter
$p_r(t)$	pulse shaping at a transmitter
P_b	bit-error-ratio
\mathcal{P}_M	mapping set with a constellation size of M
P_L	pathloss
$q(t)$	received signal in the electrical domain
$r(t)$	noisy received signal in the electrical domain

\mathbf{r}	received symbol vector
R	responsivity
\mathbf{R}_e	mean square error matrix
R_s	symbol rate
$s(t)$	transmitted waveform
\mathbf{s}	transmitted symbol vector
\mathcal{S}	codebook
SNR	signal-to-noise ratio
SINR	signal-to-interference-and-noise ratio
$\text{tr}(\cdot)$	trace operation
T_{stat}	the stationary time
$v(t)$	zero-mean white noise
$w_\theta(t)$	window function with respect to the polar angle
\mathbf{w}	thermal noise vector
\mathbf{W}	DFT matrix
$x(t)$	instantaneous optical power
$x_c(t)$	continuous-time signal
$x_d(t)$	discrete-time signal
$y(t)$	received optical power
$y_d(t)$	discrete-time received signal

Chapter 1

Introduction

1.1 Motivations

Optical wireless communications (OWC) are wireless access technologies that occupy the light spectrum, e.g., the infrared (IR), visible light (VL), or ultraviolet [Chowdhury *et al.*, 2018]. Examples of OWC are IR wireless technology [Gfeller & Bapst, 1979], visible light communications (VLC) [Komine *et al.*, 2001], optical camera communications (OOC) [Leibowitz *et al.*, 2001], and LiFi [Haas *et al.*, 2016]. To date, the main motivation behind the popularity of OWC does not stray too far from the keywords: spectrum crunch, free spectrum, and security, see [Chowdhury *et al.*, 2018] and also references therein. The term spectrum crunch was first introduced by the federal communications commission (FCC) in [FCC, 2010]. It refers to a situation where the total licensed radio frequency (RF) spectrum is less than the required spectrum to accommodate the expected total mobile data traffic. It is mentioned in [FCC, 2010] that there would be a 275-MHz spectrum deficit in 2014. Taking into account the whole RF spectrum, Cogalan and Haas further predict that the entire RF spectrum will be fully utilized by 2035 [Cogalan & Haas, 2017]. Owing to the fact that the light spectrum is unlicensed, OWC is a suitable candidate to complement RF communications [Chowdhury *et al.*, 2020]. Another advantage of OWC is its security. As light does not penetrate opaque objects, OWC can prevent eavesdropping from outside a room. This benefit can also be used to improve the security of RF communications in 5G networks by using both OWC and RF communications simultaneously [Anamalamudi *et al.*, 2018].

This thesis tries to discuss the complementing advantage of OWC, especially in hybrid WiFi and LiFi networks. There are several motivations for focusing on hybrid WiFi and LiFi networks, which are detailed as follows.

- (Why WiFi?)

By 2022, 59% of global mobile data traffic (111.4 exabytes/month) will be offloaded to WiFi [Cisco, 2020]. This number is higher than that in the previous prediction, which

is 54% (13.4 exabytes/month) in 2017. In addition, there might be an internet protocol (IP) traffic explosion by 2022 due to machine-to-machine and internet-of-things traffic, where the total global IP traffic will be 4.8 zettabytes per year (more than three times higher than that in 2017). 51% of the total global IP traffic is carried by WiFi [Cisco, 2020]. Additionally, WiFi plays a central role in providing indoor connectivity to date, and an estimated 80% of the mobile traffic originates and terminates from/to indoors [CommScope, 2018]. Therefore, as the global mobile data traffic will be primarily transferred over WiFi, this thesis focuses on WiFi as the RF communication system.

- (Why LiFi?)

As WiFi supports bidirectional and multiuser communications (point-to-multipoint and multipoint-to-point communications), among OWC, LiFi is the strongest candidate as it supports the same features [Haas *et al.*, 2016]. Recently, a new task group called Institute of Electrical and Electronics Engineers (IEEE) 802.11 Light Communications Amendment - Task Group “bb” (TGbb)¹ was established to standardize LiFi technology, which will adopt the physical (PHY) layer of WiFi-6 (IEEE 802.11ax) [Serafimovski, Han, Weszely, *et al.*, 2019]. It is also planned that the medium access control (MAC) layer of IEEE 802.11bb adopts that of IEEE 802.11ax, which supports bidirectional and multiuser communications. Meanwhile, other OWC technologies based on the corresponding standards only support point-to-point communications, see [IEEE 802.15 TG 7m, 2019; IEEE 802.15 TG 13, 2019; ITU-T G.9991, 2019].

Specifically, this thesis seeks to calculate a metric called an offloading efficiency, which can measure the contribution of LiFi in hybrid WiFi and LiFi networks. Intuitively, out of the 59% of global mobile data traffic, the offloading efficiency can be used to approximate how much traffic LiFi can carry. This investigation is presented in the last technical chapter of this thesis, which is Chapter 5. Before directly discussing the offload efficiency, many other details must be addressed, such as the random orientation model of a mobile device and human models that will illustrate how user bodies may block the LiFi channel. The reason for this is that there have been many studies on calculating offload capabilities of LiFi in hybrid WiFi and LiFi networks that do not incorporate realistic assumptions and therefore having these models is highly important. These studies can be found in the latest survey in hybrid WiFi and LiFi networks [Wu *et al.*, 2020] and references therein. For example, a theoretical study in [Stefan *et al.*, 2013] concludes

¹https://www.ieee802.org/11/Reports/tgbb_update.html.

that an area spectral efficiency gain of 920 can be obtained. However, this number was obtained without the assumptions as mentioned earlier, and it is also not straightforward to interpret it in terms of offloading efficiency. The same reasoning also applies to other theoretical studies in [Khallaf *et al.*, 2017; Li *et al.*, 2015; Y. Wang & Haas, 2015; Ma & Zhang, 2018; Obeed *et al.*, 2018]. There are also many practical implementations of hybrid WiFi and LiFi networks, such as [Shao *et al.*, 2014; Alshaer & Haas, 2016; Liu *et al.*, 2018; Haas *et al.*, 2020]. However, they mostly focus on a proof-of-concept of hybrid WiFi and LiFi networks. In the last chapter, hybrid assumptions of both practical and theoretical studies are used to estimate the offloading efficiency of LiFi. By using this method, this thesis helps to answer the benefit of combining LiFi with WiFi in future networks, such as in 6G [Zhang *et al.*, 2019, Figure 2].

1.2 Contributions and Thesis Layout

As previously mentioned, the main goal of this thesis is to calculate an offloading efficiency, which will be postponed until the intermediate studies are presented. In the subsequent chapters, a random orientation model, single-carrier and multi-carrier modulation techniques are presented. The following are logical structures and contributions of this thesis.

Chapter 2: LiFi Channel and System Models

This chapter mostly discusses channel and system models that will be used in the following chapters. The models include the frequency responses and the linear dynamic ranges of the light emitters. These models are mostly taken from TGbb as they have been agreed by many parties within the task group. However, one of the contributions of this thesis is an open-source, lightweight library, called `owcsimpy`. The main contribution of `owcsimpy` is its 3D object modeling, which enables users to generate arbitrary 3D objects including their directions or orientations. The existence of 3D objects is important, mainly because an opaque object can block LiFi signals. Moreover, the locations of 3D objects, such as furniture, can limit the mobility of users. Then, these 3D objects can be used to generate CIRs of LiFi channels by using existing methods, for example, a deterministic approach proposed in [Barry *et al.*, 1993]. The main advantages of `owcsimpy` are that it is open source and lightweight, where it can be quickly installed in many computing instances. It is useful in cases when many CIRs need to be generated.

Chapter 3: Random Orientation Model

The next contribution of this thesis is a random orientation model. Prior to this contribution being published, there have been very few studies that assume randomly-oriented LiFi-enabled devices. Due to the nature of short-range communications in LiFi, an outage can occur when the mobile device faces away from an access point (AP). In addition, assuming randomly-oriented devices can break the symmetry of downstream (from an AP to a station (STA)) and upstream of LiFi channels where the STA is assumed to face upwards with the AP facing downwards. The random orientation model is proposed based on real data measurements. In the chapter, the knowledge of the random orientation model is also used to calculate the coherence time in LiFi channels, which is also one of the contributions in this thesis. Knowing this value helps system designers to plan and place LiFi APs in the future software-defined networking (SDN)-enabled WiFi and LiFi networks.

Chapter 4: Modulation: Single-Carrier and Multi-Carrier

Having near-realistic assumptions of LiFi channels in terms of both random orientation and random blockage models, the next contribution focuses on modulation techniques for LiFi. Both single-carrier and multi-carrier modulation schemes are investigated. The primary reason for this is that, based on the comparisons in [Nuwanpriya *et al.*, 2015; Khalighi *et al.*, 2017], either single or multi-carrier schemes do not generally outperform each other. That is, single-carrier modulation techniques are superior compared to others in the low spectral efficiency region. Meanwhile, at a higher spectral efficiency region, OFDM-based techniques are better. Depending on LiFi use cases, therefore, it is useful to study both modulation techniques. The single-carrier techniques are based on PAM-SCFDE [Nuwanpriya *et al.*, 2015]. PAM-SCFDE can be seen as a block transmission system with a CP and a linear feed-forward equalizer filter at the receiver, which is optimized based on the minimum mean square error (MMSE) criterion. Therefore, the next natural improvement is to add a non-linear equalizer, e.g., DFE and THP. This thesis also discusses another way to improve PAM-SCFDE by improving the constellation symbols using IM, which is referred to as PAM-GTIM. As for multi-carrier systems, the OFDM-based system that has been agreed as the common mode in TGbb is introduced. Limitations of the OFDM-based system are also given in this chapter as well as a proposed solution, which is referred to as IQ-WDM. Lastly, performance comparisons of both single-carrier and multi-carrier systems are given at the end of this chapter.

Chapter 5: Hybrid WiFi-LiFi: Determining the LiFi Offloading Capability

In this last technical chapter, results from previous chapters are used, i.e., the assumptions and the blockage model from Chapter 2, the random orientation model from Chapter 3, and the OFDM system from Chapter 4. The offloading efficiency is calculated by emulating the hybrid WiFi and LiFi networks using Linux namespaces. Using the Linux namespaces, the real transmission control protocol (TCP)/IP stack can be used. This enables us to use multipath transmission control protocol (MPTCP) [Ford *et al.*, 2011] to provide simultaneous WiFi and LiFi connections so that, for example, seamless handover from LiFi to WiFi can be emulated in the event of a blockage. The wireless channel and the PHY layer processing blocks are abstracted by means of link-to-system mapping [Brueninghaus *et al.*, 2005]. The data traffic is emulated by directly accessing some popular websites based on the Alexa list [Alexa, 2020]. Finally, the offloading efficiency is shown by combining these emulation and simulation methods.

Chapter 6 concludes and discusses briefly how to extend the results from this thesis into future research.

1.3 Publication Lists

In order to sum up the contributions of this thesis, the following are publication lists made throughout my study as well as those that are under preparation.

Open Source Libraries:

- [1] **Purwita, A. A.** (2020). `owcsimpy`: a Python simulator for optical wireless communications. <https://github.com/ardimasp/owcsimpy>.
- [2] **Purwita, A. A.** (2020). `wlanlifi`: Codebase for LiFi simulation which is based on the IEEE 802.11 Light Communications Amendment - Task Group “bb”. <https://github.com/ardimasp/wlanlifi>.

Deliverable:

- [1] Garcia, A., Cogalan, T., **Purwita, A. A.**, Mur, D. C., Khalili, H., Sark, V., Gutiérrez, J., Hemadeh, I., Kainulainen, J., Turyagyenda, C., Frank, H., Bian, R., & Ghoraishi, M. (2020), State-of-the-Art Review and Initial Design of the Integrated 5GNR/Wi-Fi/LiFi Network Frameworks on Coexistence, Multi-Connectivity, Resource Management and

Positioning. 5G-CLARITY Deliverable D3.1. https://www.5gclarity.com/wp-content/uploads/2020/09/5G-CLARITY_D3.1.pdf.

Journal Papers:

- [1] Soltani, M. D., **Purwita, A. A.**, Zeng, Z., Haas, H., & Safari, M. (2019). Modeling the Random Orientation of Mobile Devices: Measurement, Analysis and LiFi Use Case. *IEEE Transactions on Communications*, 67(3), 2157-2172.
- [2] **Purwita, A. A.**, Soltani, M. D., Safari, M., & Haas, H. (2019). Terminal Orientation in OFDM- Based LiFi Systems. *IEEE Transactions on Wireless Communications*, 18(8), 4003- 4016.
- [3] Dehghani Soltani, M., **Purwita, A. A.**, Tavakkolnia, I., Haas, H., & Safari, M. (2019). Impact of Device Orientation on Error Performance of LiFi Systems. *IEEE Access*, 7, 4169041701.
- [4] Xie, E., He, X., Islim, M. S., **Purwita, A. A.**, McKendry, J. J. D., Gu, E., ... Dawson, M. D. (2019). High-Speed Visible Light Communication Based on a III-Nitride Series-Biased Micro-LED Array. *Journal of Lightwave Technology*, 37(4), 1180-1186.
- [5] **Purwita, A. A.**, Yesilkaya, A., Safari, M., & Haas, H. (2020). Generalized Time Slot Index Modulation for Optical Wireless Communications. *IEEE Transactions on Communications*, 68(6), 3706-3719.
- [6] Chen, C., Basnayaka, D., **Purwita, A. A.**, Wu, X., & Haas, H. (2020). Wireless Infrared-based LiFi Uplink Transmission with Link Blockage and Random Device Orientation. *IEEE Transactions on Communications* (accepted).

Conference Papers:

- [1] **Purwita, A. A.**, Chen, C., Basnayaka, D. A., & Haas, H. (2017). Aggregate Signal Interference of Downlink LiFi Networks. In 2017 IEEE Global Communications Conference (GLOBECOM), (p. 1-6). Singapore, Singapore.
- [2] **Purwita, A. A.**, Dehghani Soltani, M., Safari, M., & Haas, H. (2018). Impact of terminal orientation on performance in LiFi systems. In 2018 IEEE Wireless Communications and Networking Conference (WCNC) (p. 1-6). Barcelona, Spain.
- [3] **Purwita, A. A.**, Soltani, M. D., Safari, M., & Haas, H. (2018). Handover Probability of Hybrid LiFi/RF-Based Networks with Randomly-Oriented Devices. In 2018 IEEE 87th Vehicular Technology Conference (VTC Spring) (p. 1-5). Porto, Portugal.

- [4] Chen, C., Soltani, M. D., Safari, M., **Purwita, A. A.**, Wu, X., & Haas, H. (2019). An Omnidirectional User Equipment Configuration to Support Mobility in LiFi Networks. In 2019 IEEE International Conference on Communications Workshops (ICC Workshops) (p. 1-6). Shanghai, China.
- [5] **Purwita, A. A.**, Chen, C., Safari, M., & Haas, H. (2019). Cyclic-Prefixed System with PAM using DFE and THP for Uplink Transmission in LiFi. In ICC 2019 - 2019 IEEE International Conference on Communications (ICC) (p. 1-6). Shanghai, China.
- [6] **Purwita, A. A.**, Yesilkaya, A., Tavakkolnia, I., Safari, M., & Haas, H. (2019). Effects of Irregular Photodiode Configurations for Indoor MIMO VLC with Mobile Users. In 2019 IEEE 30th Annual International Symposium on Personal, Indoor and Mobile Radio Communications (PIMRC) (p. 1-7). Istanbul, Turkey.
- [7] **Purwita, A. A.**, Yesilkaya, A., Cogalan, T., Safari, M., & Haas, H. (2019). Generalized Time Slot Index Modulation for LiFi. In 2019 IEEE 30th Annual International Symposium on Personal, Indoor and Mobile Radio Communications (PIMRC) (p. 1-7). Istanbul, Turkey.
- [8] **Purwita, A. A.**, & Haas, H. (2020a). IQ-WDM for IEEE 802.11bb-based LiFi. In 2020 IEEE Wireless Communications and Networking Conference (WCNC) (p. 1-6). Seoul, Korea (South).
- [9] **Purwita, A. A.**, & Haas, H. (2020b). Studies of Flatness of LiFi Channel for IEEE 802.11bb. In 2020 IEEE Wireless Communications and Networking Conference (WCNC) (p. 1-6). Seoul, Korea (South).
- [10] Dehghani Soltani, M., **Purwita, A. A.**, Zeng, Z., Chen, C., Haas, H., & Safari, M. (2020). An Orientation-Based Random Waypoint Model for User Mobility in Wireless Networks. In 2020 IEEE International Conference on Communications Workshops (ICC Workshops) (p. 1-6). Dublin, Ireland.

Standardization:

- [1] **Purwita, A.**, Rossius, A., Haas, H., Serafimovski, N., Afgani, M., Berner, S., ... Uysal, M. (2020). Proposals and related work on Center Frequency for the Common Mode Mandatory PHY. <https://mentor.ieee.org/802.11/dcn/20/11-20-1449-03-00bb-proposals-and-related-work-on-center-frequency-for-the-common-mode-mandatory-phy.pptx>.
- [2] **Purwita, A.**, Haas, H., Serafimovski, N., Afgani, M., Berner, S., Walker, D., ... Miramirkhani, F. (2020). Proposed Center Frequency for the Common Mode Manda-

- tory PHY. <https://mentor.ieee.org/802.11/dcn/20/11-20-0572-00-00bb-proposed-center-frequency-mandatory-phy.pptx>.
- [3] **Purwita, A.**, Haas, H., Serafimovski, N., & Berner, S. (2020). Proposed Center Frequency for the Common Mode Mandatory PHY. <https://mentor.ieee.org/802.11/dcn/20/11-20-0815-00-00bb-proposed-center-frequency-for-common-mode-mandatory-phy.pptx>.
- [4] **Purwita, A.**, Videv, S., Haas, H., & Serafimofski, N. (2019, September). Spectral Flatness Test of the TGbb's Reference Channel Models with HE Waveform. Retrieved from <https://mentor.ieee.org/802.11/dcn/19/11-19-1639-01-00bb-spectral-flatness-test-of-the-tgbb-refrence-channel-models-with-he-waveform.pptx>
- [5] Rossius, A., Berner, S., Weszely, T., **Purwita, A.**, Haas, H., Serafimovski, N., ... Han, C. (2020). Experimental results for TGbb centre frequency discussion. <https://mentor.ieee.org/802.11/dcn/20/11-20-1037-00-00bb-experimental-results-for-tgbb-centre-freq-discussion.pptx>.
- [6] Serafimovski, N., Han, C., Weszely, T., Videv, S., **Purwita, A.**, Dehghani, M., ... Haas, H. (2019). Proposal for common-mode mandatory PHY. <https://mentor.ieee.org/802.11/dcn/19/11-19-1625-04-00bb-proposed-common-mode-mandatory-phy.pptx>.

Under Preparation:

- [1] Purwita, A. A., Cogalan, T., & Haas, H. (2020). Coherence Time of Indoor LiFi Channels. to be submitted.
- [2] Purwita, A. A., Cogalan, T., Soltani, M. D., Safari, M., & Haas, H. (2020). owcsimpy: A 3D Simulator for Indoor Optical Wireless Channels. to be submitted.
- [3] Purwita, A. A., Cogalan, & Haas, H. (2020). Hybrid WiFi-LiFi: How Much Will LiFi Contribute?. to be submitted.

1.4 Summary

This chapter discusses the main motivation of this thesis, which is trying to calculate the offloading efficiency of LiFi in hybrid WiFi and LiFi networks. The primary reason for this is

that WiFi is predicted to carry more than 50% of global mobile traffic. Therefore, knowing the offloading efficiency, we can estimate, out of the 50% of global mobile traffic, what portion can be carried by LiFi. In order to calculate it, other studies need to be conducted. For example, parts of the contributions of this thesis are:

- the open source library `owcsimpy`, where random blockage can be modeled,
- a random orientation model,
- PAM-SCFDE with DFE, THP, and GTIM, and
- IQ-WDM.

Lastly, a list of publications made throughout my Ph.D. study is given.

Chapter 2

LiFi Channel and System Models

2.1 Introduction

This chapter mainly discusses LiFi channel and system models. The main purpose of this chapter is to define assumptions that will be used in the following chapters. It means that if an assumption is not specifically mentioned in a following chapter or section, then the assumption follows the description defined in this chapter. The general abstraction of a LiFi channel model consists of a transceiver and channel models, which include the direct current (DC) wander effect, the generalized Lambertian propagation pattern, multipath propagation model, *etc.* A reference model of a LiFi system that has been agreed in the TGbb is also discussed. At the time of writing, TGbb has agreed on the operating wavelength spectrum for IEEE 802.11bb. Based on [Serafimovski, Han, Weszely, *et al.*, 2019], the related motion states the following.

“Move to adopt the 800nm - 1,000nm wavelength spectrum as the mandatory, common mode wavelength for all TGbb STAs.”

In other words, the common mode of IEEE 802.11bb suggests the use of the IR spectrum for both downlink and uplink transmissions. There are two main reasons behind this motion. The first reason is that the responsivity of silicon-based PDs is higher at those ranges compared to that in the VL spectrum as shown in Figure 2.1, which shows four samples of responsivities of different Silicon-based PDs taken from [Edmund Optics®, 2020]. Note that the responsivity describes a conversion factor of the received signal from the optical domain to the electrical domain [Edmund Optics®, 2020]. The second reason is to avoid issues with VLC, where a communication link is disrupted if the light source is dimmed. Therefore, throughout this thesis, we will assume the 800nm - 1,000nm optical spectrum.

The remainder of the chapter is organized as follows. Section 2.2 discusses the LiFi channel model that includes the transceiver and optical wireless channel models. Section 2.3 discusses the examples of the channel model. The examples include the transceiver frontend models that have been agreed in TGbb. Finally, Section 2.4 summarizes this chapter.

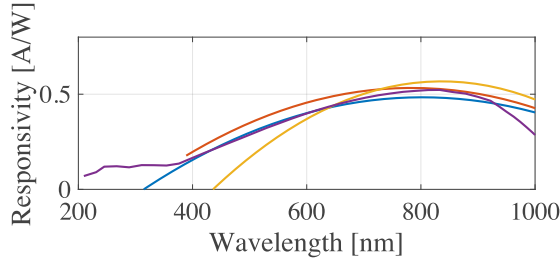


Figure 2.1. Responsivities of four different Silicon-based PDs taken from [Edmund Optics®, 2020]. (Please refer to [Edmund Optics®, 2020] for more detailed information on the corresponding curves. Note that details are removed for clarity purposes.)

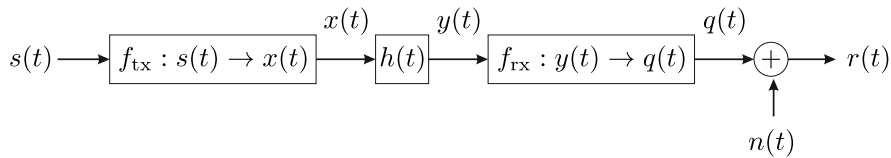


Figure 2.2. A transceiver model of IM/DD systems.

2.2 LiFi Channel Model

Throughout this thesis, intensity modulation and direct detection (IM/DD) systems are assumed. With intensity modulation, an input current waveform is modulated onto an instantaneous optical power (in Watt) at the transmitter. A direct detection receiver converts the instantaneous optical power back into a current. Figure 2.2 denotes a transmission model of IM/DD systems. The transmitted waveform $s(t)$ is mapped to the instantaneous power $x(t)$ by a mapping function f_{tx} . The mapping function f_{tx} can represent, for example, a combination of an optical-power-vs.-electrical-current ($P - I$) curve and a low-pass filter model of a light emitting diode (LED). Then, the instantaneous power $x(t)$ is transmitted over an optical wireless channel $h(t)$. Based on [Kahn, Krause, & Carruthers, 1995; Kahn & Barry, 1997], the received optical power can be expressed as:

$$y(t) = h(t) \circledast x(t), \quad (2.1)$$

where \circledast denotes the convolution operation. At the receiver, a mapping function f_{rx} is used as a representation of, for example, the responsivity of a PD (in A/W), i.e., $q(t) = Ry(t)$, where R is the responsivity. Then, an additive noise $n(t)$ is used to represent the thermal noise that is usually modeled as additive white Gaussian noise (AWGN).

The rest of this section will discuss the transmitter model (represented by f_{tx}), an optical wireless channel model (represented by $h(t)$), and a receiver model (represented by f_{rx}).

2.2.1 Transmitter Model

A transmitter model is shown in Figure 2.3. The model includes a driver, a frequency response H_{tx} , a DC bias, a $P - I$ curve, and a diffuser. The aggregate effect of the driver, H_{tx} , and the DC bias should generate a driving current of an emitter, e.g., an LED or an LD, that fits within its linear region in the $P - I$ curve, which is shown in the red shaded area. The linear region is also determined based on an eye safety requirement, e.g., [BSI British Standards Std., 2008; International Electrotechnical Commission, 1993]. In this thesis, H_{tx} , which is modeled as a finite impulse response (FIR) filter, represents the aggregate frequency response of a driver and emitters. H_{tx} is assumed to have a bandpass filter characteristics, where the highpass filter is used to represent the DC wander effect (also known as the baseline wander) that has a cutoff frequency of around 100 kHz [Grobe *et al.*, 2016]. The DC wander refers to a phenomenon where a signal is not DC balanced or the mean of a signal changes over time [Grobe *et al.*, 2016]. A primary cause of the DC wander is due to the use of a high-pass filter (HPF) to mitigate DC photocurrent generated by ambient light [Street *et al.*, 1997].

A diffuser is typically used in order to spread the optical radiation, especially for LDs. Throughout this thesis, a diffuser is assumed so that the radiation of $x(t)$ follows the generalized Lambertian pattern [Kahn & Barry, 1997]. Moreover, a diffuser is assumed to be an attenuator, and the range of the attenuation is around 70% to 90% [Kahn & Barry, 1997]. In addition, the generalized Lambertian pattern is characterized by a mode number, denoted by m [Gfeller & Bapst, 1979], which is defined as:

$$m = \frac{-\ln 2}{\ln \cos \Phi_{1/2}}, \quad (2.2)$$

where $\Phi_{1/2}$ is the half-power semiangle of emitters. In many datasheets, the value of $\Phi_{1/2}$ can be found based on the value of full width at half maximum (FWHM).

2.2.2 Optical Wireless Channel Model

In this thesis, the channel model $h(t)$ is mainly based on deterministic approaches [Barry *et al.*, 1993; Carruthers & Kannan, 2002b; Schulze, 2016]. Let ε be an elemental object, which can

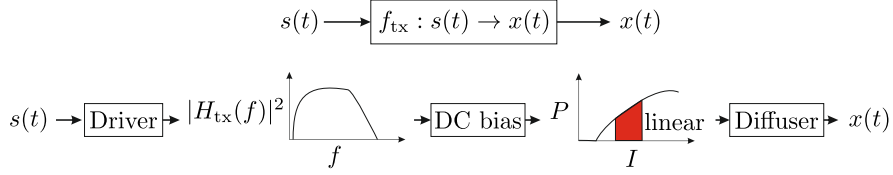


Figure 2.3. A transmitter model.

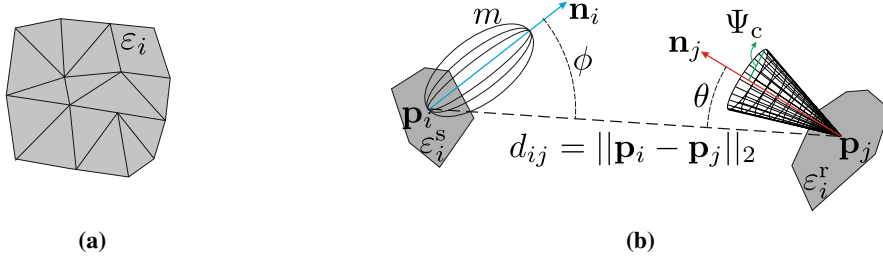


Figure 2.4. (a) The partitioning of an arbitrary 2D plane into smaller planes, and (b) the geometry model.

physically represent either a reflecting surface (which is assumed to be a purely diffusive) or a light emitter or receiver [Barry *et al.*, 1993]. As a reflecting surface, the elemental object can also be a partition of a big reflecting surface as depicted in Figure 2.4(a). An elemental object is defined as a set of attributes, i.e.,:

$$\varepsilon = \{\mathbf{p}, \mathbf{n}, m, A, \Psi_c, \rho\}, \quad (2.3)$$

where \mathbf{p} is a position vector, \mathbf{n} is a normal vector, m is the mode number of the Lambertian radiation (2.2), A is a detection area, Ψ_c is a field-of-view (FoV), and ρ is a reflectivity. Note that an elemental object acting as a source, referred to as an elemental source, is denoted by adding the superscript ‘s’, i.e., ε^s . Similarly, an elemental receiver is denoted by ε^r . A reflecting surface ε^s has $m = 1$ (ideal Lambertian), and a reflecting surface ε^r has the FoV of 90° [Barry *et al.*, 1993]. An illustration of an elemental source and receiver is shown in Figure 2.4(b), where d_{ij} denotes the distance of \mathbf{p}_i and \mathbf{p}_j , and $\|\cdot\|_2$ is the L2-norm.

A source \mathcal{S} (e.g., a LED) and a receiver \mathcal{R} (i.e., a PD) are defined as a subset of ε as follows:

$$\mathcal{S} = \{\mathbf{p}, \mathbf{n}, m\}, \text{ and } \mathcal{R} = \{\mathbf{p}, \mathbf{n}, A, \Psi_c\}. \quad (2.4)$$

The CIR $h(t; \mathcal{S}, \mathcal{R})$ of a source \mathcal{S} and a receiver \mathcal{R} is defined as an infinite sum, i.e.,:

$$h(t; \mathcal{S}, \mathcal{R}) = \sum_{k=0}^{\infty} h^{(k)}(t; \mathcal{S}, \mathcal{R}), \quad (2.5)$$

where $h^{(k)}(t; \mathcal{S}, \mathcal{R})$ is the CIR in which only k reflections are considered. Based on [Barry *et al.*, 1993], $h^{(k)}(t; \mathcal{S}, \mathcal{R})$ can be approximated as:

$$h^{(k)}(t; \mathcal{S}, \mathcal{R}) \approx \sum_{i=0}^{N-1} h^{(0)}(t; \mathcal{S}, \varepsilon_i^r) \circledast h^{(k-1)}(t; \varepsilon_i^s, \mathcal{R}), \quad (2.6)$$

where N is the total number of elemental objects ε . Notice that $h^{(k)}(t; \mathcal{S}, \mathcal{R})$ is calculated recursively in (2.6). The base case of the above recursive form with the elemental source ε_i^s and the elemental receiver ε_j^r can be calculated by using its DC channel gain, which is defined as:

$$h^{(0)}(t; \varepsilon_i^s, \varepsilon_j^r) = \frac{(m_i + 1)A_j}{2\pi d_{ij}^2} \cos^{m_i}(\phi) \cos(\theta) \mathbb{1}(\theta) V_{ij}, \quad (2.7)$$

where $\mathbb{1}(\theta)$ is an indicator function for $0 \leq \theta \leq \Psi_{cj}$, and V_{ij} is the visibility function that evaluates if the path between ε_i^s and ε_j^r is not obstructed. It is worth noting here that other variants of (2.5) and (2.6) are available, such as an iterative approach in [Carruthers & Kannan, 2002b] and a frequency-domain approach [Schulze, 2016].

2.2.3 Receiver Model

A receiver model is depicted in Figure 2.5. An optical-to-electrical (O/E) converter is used to convert the received instantaneous optical power $y(t)$ to the corresponding signal in the electrical domain. The O/E converter model includes a responsivity of a PD R (in A/W) and a gain coming from an optical filter and a concentrator. If an avalanche photodiode (APD) is used, then a shot noise is added. Otherwise, if a positive-intrinsic-negative photodiode (PIN) is used, then the shot noise can be ignored [Kahn & Barry, 1997]. A shot noise model captures the ambient light noises coming from sunlight, incandescent, and fluorescent lamps [Gfeller & Bapst, 1979; Kahn & Barry, 1997]. Suppose if an amplifier is used, then the excess noise factor of an APD should also be considered. The excess noise factor measures the effect of multiplying the shot noise by an amplifier, e.g., TIA. In addition, the effect of excess noise

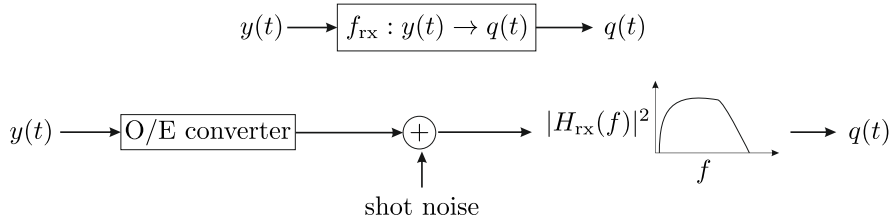


Figure 2.5. A receiver model.

factor is captured by the variance of the shot noise as given by [Tsonev *et al.*, 2017]:

$$\sigma_{\text{shot}}^2 = (2q(I_D + R\Theta)F)G_{\text{APD}}G_{\text{TIA}}, \quad (2.8)$$

where q is the elementary charge of an electron, I_D is a photodiode dark current (which is in the order of 1 nA), Θ is the optical power collected by the APD, F is the excess noise factor (which is typically around 0.3), G_{APD} is the gain of the APD, and G_{TIA} is the gain of TIA. Similar to the transmitter model, a bandpass filter having a magnitude response of $|H_{\text{rx}}(f)|^2$ is also used in the receiver model.

2.3 LiFi System Model

Given the abstraction of a LiFi channel model, as discussed in Section 2.2, this section introduces a realization of such a model. Specifically, the frontend models are based on a measurement-based model from the TGbb [Hinrichs, Hilt, Hellwig, Jungnickel, & Bober, 2019]. In addition, the channel model is based on a near-realistic model that considers blocking and wavelength-dependent reflecting objects.

2.3.1 Frontend Model

If a system model is not specifically mentioned in one of the chapters, then the system model follows an agreed model from TGbb [Hinrichs *et al.*, 2019]. The reason for using the TGbb model is that it is publicly available, and it has been agreed by all organizations in the TGbb. In [Hinrichs *et al.*, 2019], wideband transceiver frontend systems are proposed based on real measurements. The Tx frontend mainly comprises a driver and an emitter. A simplified measurement setup is shown in Figure 2.6(a). The driver matches the impedance from the Tx digital

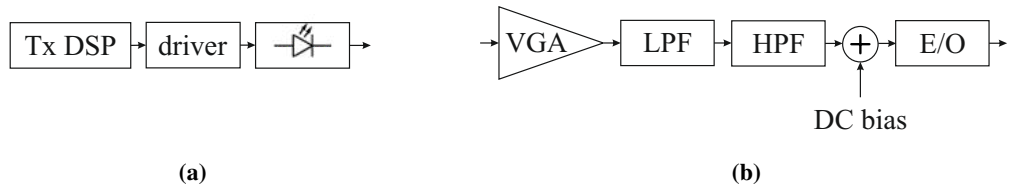


Figure 2.6. (a) Measurement setup for the Tx frontend, and (b) the Tx frontend model. Note that DSP stands for digital signal processor and VGA stands for variable gain amplifier.

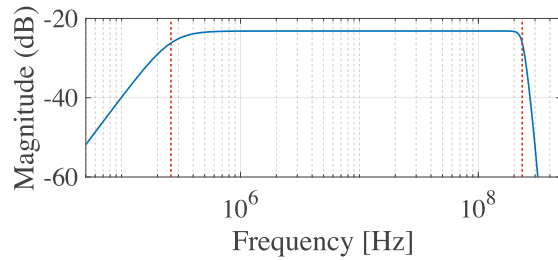


Figure 2.7. A bandpass magnitude response of the Tx frontend model based on a 30mW LC850-0030AR VCSEL (850 nm), where the red dashed lines show the cutoff frequencies, i.e., 2.6×10^5 Hz and 2.34×10^8 Hz.

signal processor (DSP), which is typically around 50Ω , and the impedance from the emitter, which is typically only a few ohms. A bias current is also considered to be a part of the driver. Figure 2.6(b) depicts the equivalent model of Figure 2.6(a). A variable gain amplifier (VGA) is assumed to model an input current in Ampere. The bandpass filter is modeled by a concatenation of a low-pass filter (LPF) and a HPF. Then, a DC bias is added to the output of HPF before being fed into an electrical-to-optical (E/O) device. The magnitude response of the Tx frontend model is shown in Figure 2.7, which also shows the cutoff frequencies of 2.6×10^5 Hz and 2.34×10^8 Hz (which equivalently gives a bandwidth of around 230 MHz).

Based on [Hinrichs *et al.*, 2019], the Rx model is measured by using a bootstrap TIA in order to match the impedance of the receiver and that of Rx DSP, which is shown in Figure 2.8(a). Its block diagram model is shown in Figure 2.8(b). The existence of a shot noise is due to the use of an APD. As in the Tx model, an HPF is also used to remove the DC signal. A thermal noise component is added after the HPF. An automatic gain controller (AGC) is used in order to normalize the amplitude of the signal. Finally, the output of the AGC is fed through an LPF. The magnitude response of the Rx frontend model is shown in Figure 2.9, which also shows the cutoff frequencies of 4.8×10^5 Hz and 2.6×10^8 Hz (which equivalently results in a bandwidth of around 260 MHz). Based on the datasheet of the LC850-0030AR vertical-cavity surface-

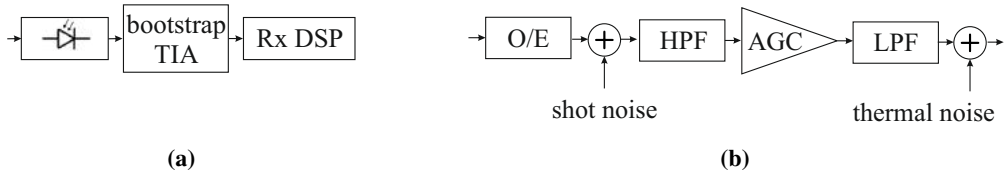


Figure 2.8. (a) Measurement setup for the Rx frontend, and (b) the Rx frontend model. Note that AGC stands for automatic gain controller.

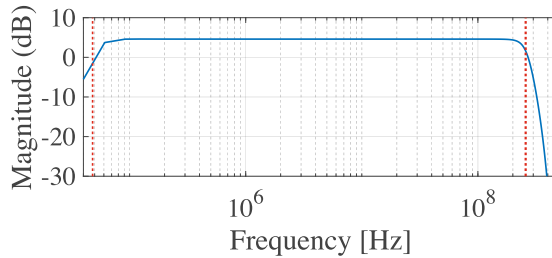


Figure 2.9. A bandpass magnitude response of the Rx frontend model based on SAR1500H4 Si APD, where the red dashed lines show the cutoff frequencies, i.e., 4.8×10^4 Hz and 2.6×10^8 Hz.

emitting laser (VCSEL), its $P - I$ curve is shown in Figure 2.10, where the linear region is from 30 mA to 39 mA based on its first derivative, i.e., dP/dI . It is assumed that the $\Phi_{1/2}$ is 24° , and a diffuser is used with the attenuation of 0.9. The detection area and the FoV is 10 mm^2 and 45° , respectively. A concentrator optical gain is 1.7. Note that two different wavelengths will be used throughout this thesis, i.e., 850 nm and 940 nm. The frequency responses of the frontends and the linear region are assumed to be almost the same. The main difference comes from the different attenuations at different wavelengths from reflecting materials and the responsivity of the PD, which will be discussed in the next subsection.

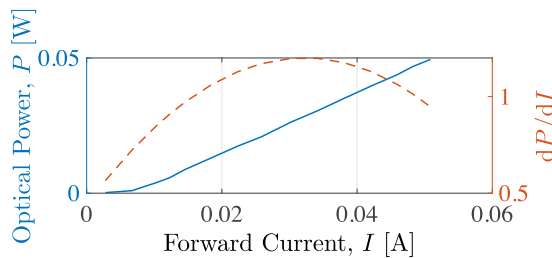


Figure 2.10. The $P - I$ curve of the 30mW LC850-0030AR VCSEL.

2.3.2 Channel Model

`owcsimpy` [Purwita, 2020] is used to generate wireless optical CIRs, $h(t)$. To the best of the author's knowledge, the existing implementations of CIR calculations are all licensed-based. For example, implementations of [Carruthers & Kannan, 2002b] are available in [Carruthers & Kannan, 2002a; Rahaim, 2018], which depend on MATLAB® that needs a license to run. A popular commercial software to generate CIRs is Zemax® [Zemax, 2020], which can only be installed in the Windows operating system. The main motivation in developing `owcsimpy` is to support a mechanism where it is straightforward to calculate thousands of CIRs. It is time-consuming to use existing softwares for such a purpose. Enabling this mechanism is possible if we can widely deploy (horizontal scaling) the CIR implementation. In this space, the novelty of `owcsimpy` is that it is free, open, and lightweight. By having a free, open, and lightweight implementation, `owcsimpy` can be easily deployed to, for example, tens of cloud compute instances from several cloud providers, such as Amazon AWS, Microsoft Azure, or Google Cloud Platform. `owcsimpy` consists of a high-performance backend, which can calculate the CIRs based on the deterministic and analytical approaches [Carruthers & Kannan, 2002b; Schulze, 2016; Jungnickel *et al.*, 2002], and a modular frontend, which mainly handles geometry models. The backend of `owcsimpy` is implemented in a low-level programming language due to its computationally intensive requirement. `owcsimpy` uses C with additional libraries such as OpenMP (for multi-threading), BLAS, and LAPACK (for linear algebra operations).

The frontend module handles geometric models, and it is written in Python. Note that the primary contribution of `owcsimpy` to this thesis is its method to model arbitrary 3D objects and calculate CIRs correspondingly. A common method to approach this is, for example, by considering a fixed 3D model, such as a cylinder to model a human model. Based on this model, then a cumulative distribution function (CDF) of the channel gain is derived, which is demonstrated in [Chen *et al.*, 2019]. However, it is not straightforward to generalize it such that arbitrary 3D objects, e.g., a human model sitting on a chair inside a room, can be easily modeled. It is also difficult to combine it with other random behavior models, such as random mobility. Another limitation is that the CDF in [Chen *et al.*, 2019] is only applicable for a single-tap CIR. In this thesis, we need a CIR generator mechanism that can easily produce thousands of multipath CIRs for various scenarios to calculate realistic offloading efficiencies of LiFi in hybrid LiFi and WiFi networks. While the ability of `owcsimpy` to generate thousands of multipath CIRs has been discussed in the previous paragraph, the next paragraph will discuss

the ability of `owcsimpy` to model arbitrary 3D objects.

`owcsimpy` treats all 3D objects as a collection of 2D faces. For example, Figure 2.11(a) shows a result of the Delaunay triangulation that yields many triangular faces. The initial implementation of `owcsimpy` uses a square face as shown in a human model depicted in Figure 2.11(b). These faces are the manifestation of the elemental object ε as explained in (2.3). For the sake of the illustrations, different opacities of faces in Figure 2.11(b) show different reflectivities, i.e., the head portions of the models have different reflectivities compared to the body portions of the model. Note that the reflectivity ρ corresponds to one of the attributes of an elemental object in (2.3). By using this approach, `owcsimpy` can support wavelength-dependent CIRs based on [Lee *et al.*, 2011]. In addition, `owcsimpy` models orientations of light emitters and receivers as vectors, and detection areas of light receivers as circles.

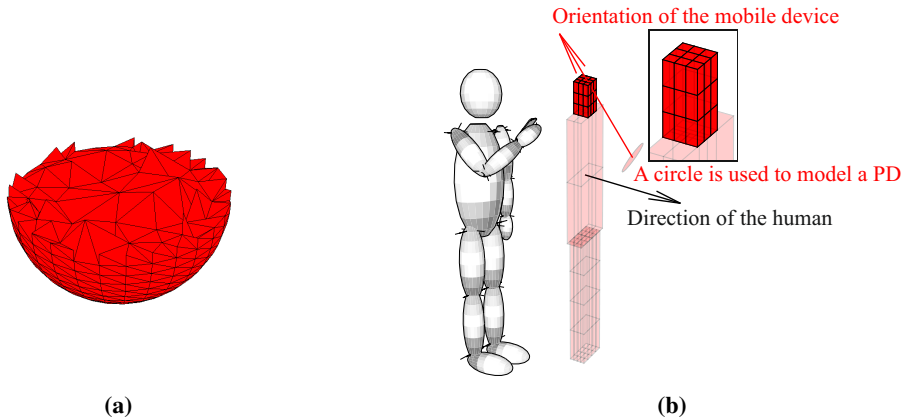


Figure 2.11. (a) An example of a 3D object as a collection of 2D faces, and (b) a human model as a collection of square faces.

It is intuitive to define a blockage event by treating a 3D object as a collection of faces. Figure 2.12 illustrates a blockage event in `owcsimpy`. Suppose we want to validate if a link between two red planes is blocked by a black plane, then an intersecting point on the black plane must be calculated first. A blockage event occurs in Figure 2.12(a) as the intersecting point, which is shown by the blue dot, is detected between the red planes. Meanwhile, Figure 2.12(b) shows that the black plane does not block the red planes.

The primary advantage of using `owcsimpy` is how straightforward it is to model arbitrary 3D objects. Different scenarios will be shown throughout this thesis, e.g., simple office environments (discussed in the next subsection), open office environments (discussed in Chapter 3), residential rooms (discussed in Chapter 5), and indoor aircraft cabins (shown in Appendix A). As `owcsimpy` allows the modeling of 3D objects with ease, various 3D objects located in

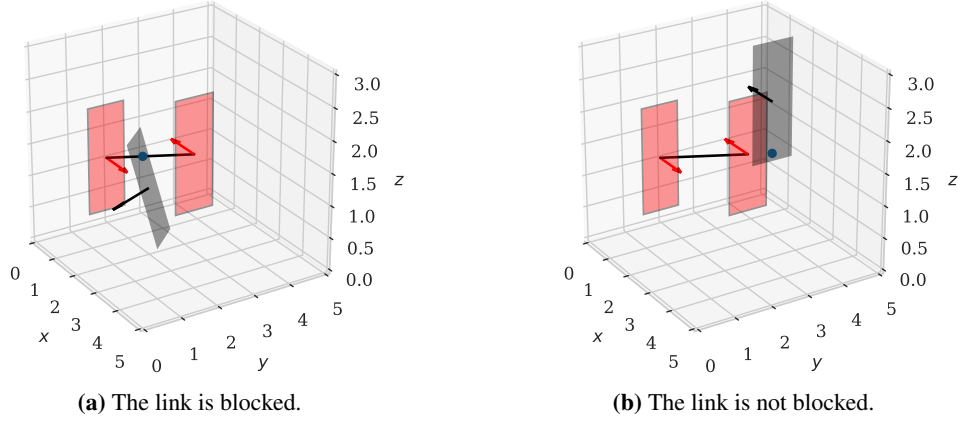


Figure 2.12. Illustration of blockage event in `owcsimpy` for a link between two red planes and a blocking object, i.e., the black plane.

random locations can be deployed. Hence, it is claimed in this thesis that `owcsimpy` can be used to easily realize the random blockage assumption and generate CIRs. Other features of `owcsimpy` are provided in Appendix A.

2.3.3 A Simple Office Environment

In this subsection, a few samples of CIRs in a simple office environment are given. An illustration of the small office environment is depicted in Figure 2.13(a). The office has the dimensions $4 \times 3 \times 3 \text{ m}^3$. The small office environment consists of an AP, a desk, a chair, and a human model holding a LiFi-enabled mobile device. The AP is located in the center of the ceiling.

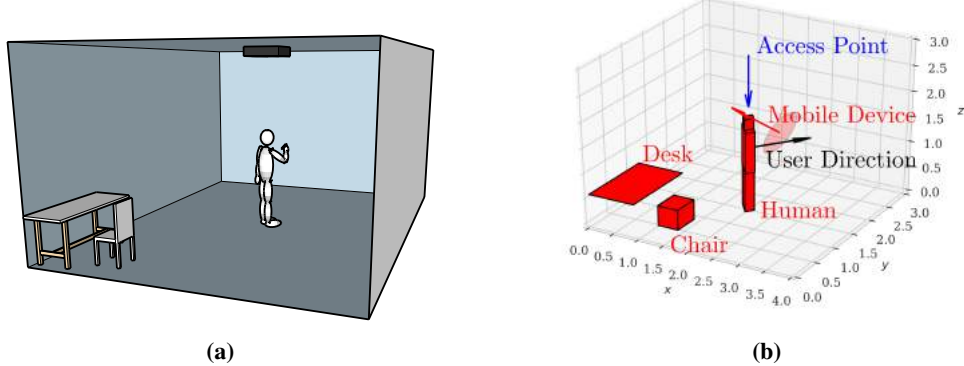


Figure 2.13. (a) A 3D model of a small office environment, and (b) its corresponding model used in `owcsimpy`.

The corresponding `owcsimpy` models of those depicted by Figure 2.13(a) is shown in Figure 2.13(b). In this case, the desk is modeled by a plane, and the chair is modeled by a cuboid.

Materials:	paint	cotton	skin	plaster	pinewood
Reflectivities (@ 940 nm):	0.04	0.65	0.70	0.85	0.92
Reflectivities (@ 850 nm):	0.04	0.64	0.66	0.83	0.92

Table 2.1. Reflectivities of materials over visible light (VL) and infrared (IR) spectrum.

The human model is modeled by a few cuboids, i.e.,:

- the head part's dimensions are 15 cm × 15 cm × 20 cm,
- the body part's dimensions are 40 cm × 15 cm × 80 cm, and
- the leg part's dimensions are 30 cm × 15 cm × 80 cm.

The AP and the mobile device are modeled by point sources; hence, vectors are used to represent them.

The surfaces of the desk and the chair are assumed to be covered in black, glossy paint as discussed in [Miramirkhani *et al.*, 2015, Figure 2]. The ceilings and walls are assumed to be made from plaster. Meanwhile, pinewood is used to model the material of the floor. Cotton is used as the material for the body and legs of the human model. The material for the head portion is assumed to be the same as that of the human skin. Spectral reflectances of these materials are taken from [Miramirkhani *et al.*, 2015; Kokaly *et al.*, 2017; Cooksey & Allen, 2013]. Summaries of the reflectivities of the materials can be found in Table 2.1.

Three different locations in the simple office environment are defined as depicted in Figure 2.14. That is, the first case illustrates a scenario where a dominant line of sight (LoS) exists. The second case represents the case where a weaker LoS exists. That is, the ratio of the received signal coming from the LoS link to the total power is less than that of the first case. The third case depicts a scenario where there is not a LoS link. In this subsection, an uplink scenario is assumed. The reason for this is that, a general study of LiFi outside this thesis mostly assumes that the downlink transmission is carried out over the VL spectrum and uplink transmission is carried out over IR spectrum [Haas *et al.*, 2016]. The CIRs are shown in Figure 2.15. Even though the CIRs coming from reflections have higher amplitudes, the difference can be neglected as the maximum mean square error (MSE) among the CIRs of the three scenarios is 2.243×10^{-16} . More results of CIRs with a user mobility and a randomly-oriented mobile device will be shown in Section 3.6.4.1.

2.4 Summary

The main purpose of this chapter is to describe both channel and system models that will be used in the following chapters. The LiFi channels are assumed to be multipath and consider realistic assumptions, such as wavelength-dependent reflectivities and random blocking objects throughout this thesis. The system model is mainly taken from the agreed baseline model from the task group that works for the LiFi standardization IEEE 802.11bb, i.e., TGbb. The system model includes the bandpass filter characteristic that also models the DC wander effect. In addition, the instantaneous shot noise is also considered for APDs. Note that throughout this thesis, it is assumed that the wavelength of 800 nm to 1,000 nm is used.

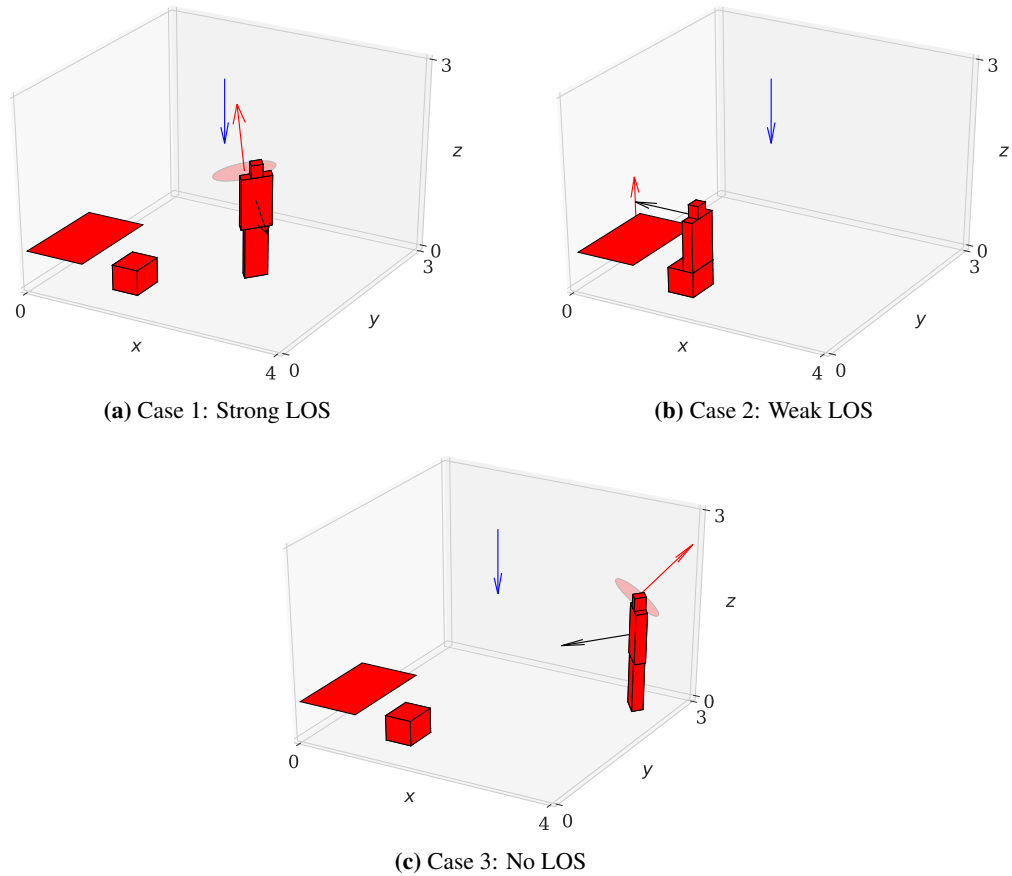


Figure 2.14. Three different realizations of a small office environment.

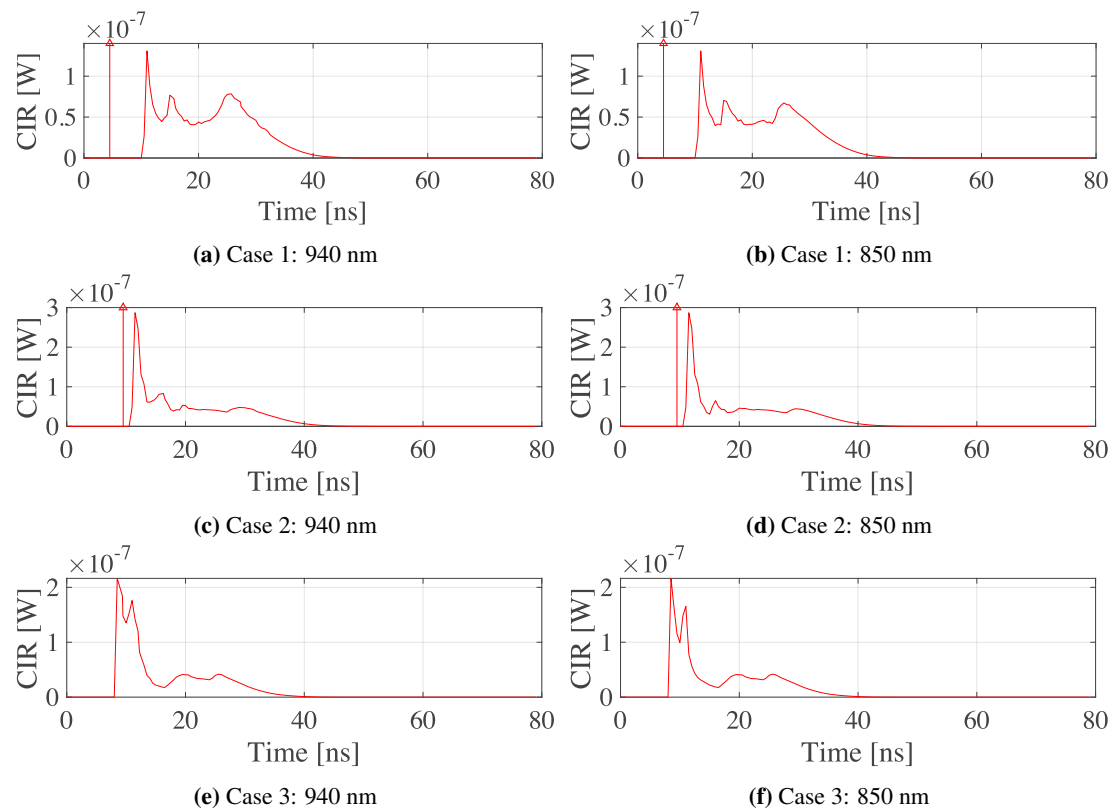


Figure 2.15. CIRs of configurations shown in Figure 2.14.

Chapter 3

Random Orientation Model

3.1 Introduction

This thesis considers on mobile users in indoor scenarios. In such scenarios, it is not realistic to assume that mobile devices will consistently face upwards towards the ceiling. The assumption where devices face upwards is suitable for the deployment of LiFi in universal serial bus (USB) dongles connected to, for example, laptops. Most of the time, mobile devices are tilted while in use, for example, when a user accesses the Internet and reads an article, or the user calls someone as depicted in Figure 3.1. Therefore, we should assume that users tilt their devices in the scenarios we use.

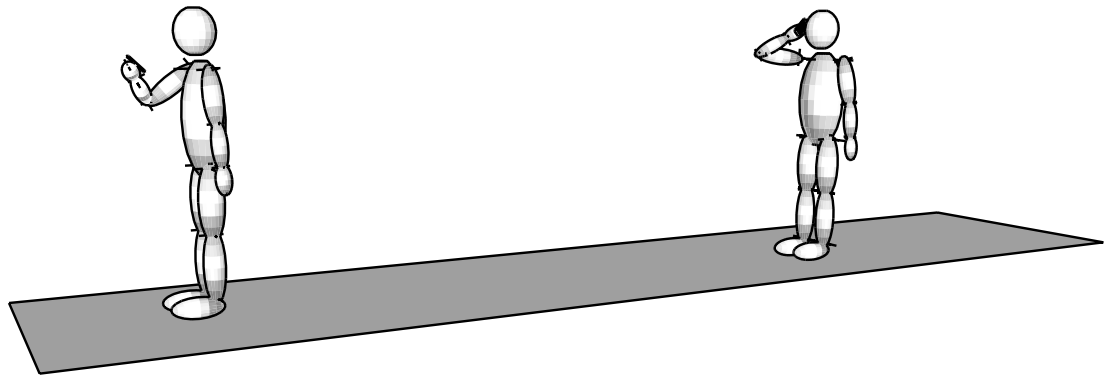


Figure 3.1. An illustration of human models using their mobile devices in a position that is not directly facing upwards.

Not only should it be assumed that devices are tilted, but randomly-oriented mobile devices should also be assumed. The reason for this is that involuntary oscillations of hands, which are also known as tremor, can be found in both healthy and sick individuals [Dick, 2017].

The contributions and related works of this chapter are presented in the next sections. Then, a random orientation model, which is mainly based on [Purwita, Soltani, *et al.*, 2019; Soltani, Purwita, *et al.*, 2019], is presented. The random orientation model in [Purwita, Soltani, *et al.*, 2019; Soltani, Purwita, *et al.*, 2019] is proposed based on measurement data collected from

40 participants who were asked to conduct a series of experiments. This measurement will be discussed in Section 3.4. The random orientation model is discussed in Section 3.5. Then, the application of the random orientation model to calculate the coherence time of indoor LiFi channels is also discussed in Section 3.6. Finally, Section 3.6 summarizes this chapter.

3.2 Contributions of This Chapter

The main contribution of this chapter is the random orientation model, which is based on real measurements. Parts of the discussions in this chapter have been published in [Purwita, Soltani, *et al.*, 2019]. In addition, a use case of the proposed random model is used to calculate the coherence time of LiFi indoor channels. The main motivation behind the coherence time study in this chapter is aligned with the final goal of this thesis, i.e., to calculate the offloading efficiency of LiFi in hybrid LiFi and WiFi networks. In the context of hybrid networks or heterogeneous networks (HetNets), it is envisioned that the implementation of HetNets will utilize the SDN paradigm [Cox *et al.*, 2017]. Based on [He *et al.*, 2015], the delay requirement of commercial SDN-enabled switches is 40 ms. That is, 40 ms is the mean time delay from the time when an SDN rule is generated until it is successfully applied in an SDN-enabled switch. Hypothetically, if LiFi CIRs keep changing before a new SDN rule is applied, then the SDN rule becomes invalid. Therefore, knowing the coherence time, which is defined as the time where a LiFi channel does not change significantly, is important to answer if LiFi could be a part of HetNets. The novelty of the coherence time investigation in this chapter is that realistic assumptions, e.g., the random mobility of users, the random orientation of mobile devices, and random blockages, are considered. Other works that are related to these contributions are discussed in the next section.

3.3 Related Works

In 2018 and 2019, the measurement-based random orientation model was published [Purwita, Dehghani Soltani, *et al.*, 2018; Purwita, Soltani, *et al.*, 2019; Soltani, Purwita, *et al.*, 2019; Zeng *et al.*, 2018]. Before that, most assumptions in the current literature on LiFi consider mobile devices while they are facing upwards, such as in [Haas *et al.*, 2016; Chen *et al.*, 2016; J. Wang *et al.*, 2018] and references therein. However, there are a few studies in the literature that incorporate randomly-oriented devices, e.g., [Y. Wang *et al.*, 2017; Chen & Haas, 2017; Eroğlu *et al.*, 2019] and references therein. All the authors assume that the random orientation

follows a certain distribution function without any support from measurement data. The lack of justification from the measurement data is the main motivation behind random orientation studies in [Purwita, Dehghani Soltani, *et al.*, 2018; Purwita, Soltani, *et al.*, 2019; Soltani, Purwita, *et al.*, 2019; Zeng *et al.*, 2018].

From outside the LiFi community, a similar random orientation model of a mobile device comes from the terahertz community [Peng & Kürner, 2017]. However, the authors only focus on the rate of change of orientation.

Other related works come from studies of tremor, such as in [Dick, 2017; Gresty & Buckwell, 1990] and references therein. As we will elaborate on further, the measurement data that are collected will fit a harmonic random process (RP), which is also typically used for characterizing tremor [Gresty & Buckwell, 1990]. The proposed random orientation model has been applied to various studies, such as:

- visible light positioning (VLP) [Kim *et al.*, 2019],
- studies of channel gain or signal-to-noise ratio (SNR) of LiFi [Soltani, Zeng, *et al.*, 2019; Arfaoui *et al.*, 2019],
- error performance of LiFi [Dehghani Soltani *et al.*, 2019],
- design of LiFi devices [C. Chen *et al.*, 2019; Tavakkolnia *et al.*, 2019],
- LiFi modulation schemes [Soltani, Arfaoui, *et al.*, 2019; Purwita, Chen, *et al.*, 2019], and
- studies of handover [Purwita, Soltani, *et al.*, 2018].

In this section, the study of the coherence time of indoor LiFi channels directly uses the random orientation model proposed in [Purwita, Soltani, *et al.*, 2019], where the random orientation model is modeled as an RP. This is in contrast to [Purwita, Dehghani Soltani, *et al.*, 2018; Soltani, Purwita, *et al.*, 2019; Zeng *et al.*, 2018] that models the random orientation as a random variable (RV). As an RP, the random orientation model can be directly combined with the random mobility of users and random blockage to investigate the coherence time of indoor LiFi channels. There are not many works focusing on the study of coherence time in LiFi. The most related studies, to the best of the authors' knowledge, is the work in [Bykhovsky, 2018; J. Chen *et al.*, 2020]. The main difference with the works in [Bykhovsky, 2018; J. Chen *et al.*, 2020] is that the former assumes a simple scenario. That is, the random orientation, random

blockage, or random mobility models are not considered. This simplification leads to the wide-sense stationary (WSS) assumption. It will be shown later that if more realistic assumptions are considered, non-WSS assumption should be used instead.

3.4 Data Collection and Assumptions

Our studies on random orientation models are based on real measurements. Forty participants were asked to sit and walk while browsing articles and watching streaming videos from the Internet. These activities will be referred to as either the *sitting* or *walking* activities. For the walking activity, the participants were asked to walk around a $40 \times 15 \text{ m}^2$ straight corridor in the Alexander Graham Building at the University of Edinburgh. The orientation of a mobile device is denoted by \mathbf{n}_u , which is a normal vector of the device's screen. The normal vector \mathbf{n}_u is represented by its spherical coordinates, namely a polar angle, denoted by θ , and an azimuth angle, denoted by ω . These descriptions are depicted in Figure 3.2.

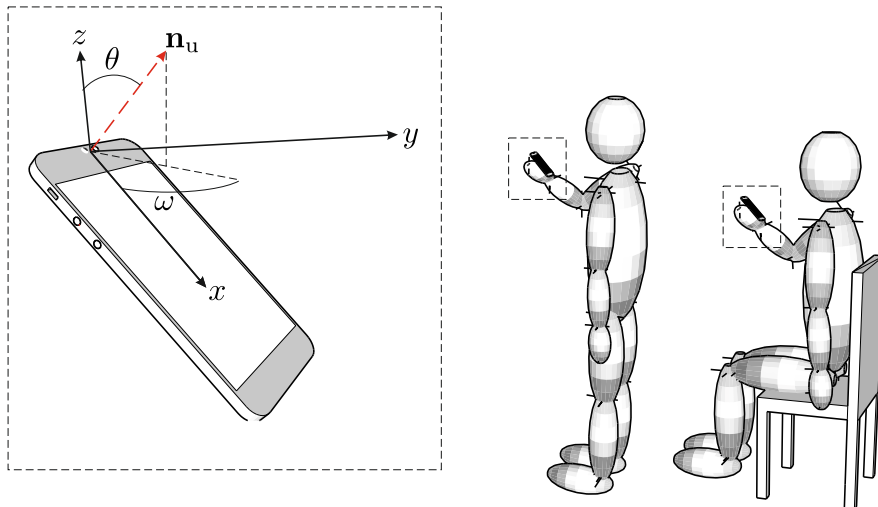


Figure 3.2. Definitions of orientation of a mobile device using spherical coordinates, and activities that are carried out by the participants.

While participants conducted the series of experiments, samples of the measurements were collected by using an application called the Physics Toolbox Sensor Suite [Vieyra Software, 2020], which was installed on a Samsung Galaxy S5. There were a total of 222 measurements that were collected. This data comprises 148 measurements for the sitting activity and 74 measurements for the walking activity. From each experiment, two noisy measurements are observed,

namely $m_\theta(t)$ and $m_\omega(t)$, which correspond to the spherical coordinates θ and ω , respectively. It is worth noting that a WSS RP is assumed for each noisy measurement. Therefore, these noisy measurements can be defined by:

$$m_\theta(t) = \mu_\theta + \theta_0(t) + n_\theta(t), \text{ and} \quad (3.1)$$

$$m_\omega(t) = \mu_\omega + \omega_0(t) + n_\omega(t). \quad (3.2)$$

$\theta_0(t)$ and $\omega_0(t)$ are zero-mean RPs, which denote the fluctuation of θ and ω around a constant value μ_θ and μ_ω , respectively. $n_\theta(t)$ and $n_\omega(t)$ denote the noise of the measurements. Figure 3.3 show a visualization of $m_\theta(t)$ when it is decomposed into its individual terms, i.e., μ_θ , $\theta_0(t)$, and $n_\theta(t)$. The term μ_θ shows the mean of the polar angle over time. The term $\theta_0(t)$ denotes a zero-mean change with respect to the polar angle. The term $n_\theta(t)$ denotes an additive zero-mean noise to the polar angle. Therefore, the term μ_θ denotes the orientation of a mobile device if a user's hand is steady, and there is no noise. The term $\theta_0(t)$ denotes a fluctuation with respect to the polar angle if the mobile device is not tilted, and there is no noise. Samples of the noisy measurements from the sitting and walking activities are shown in Figure 3.4. By briefly observing the samples, results for the sitting activity have less fluctuations and are less noisy.

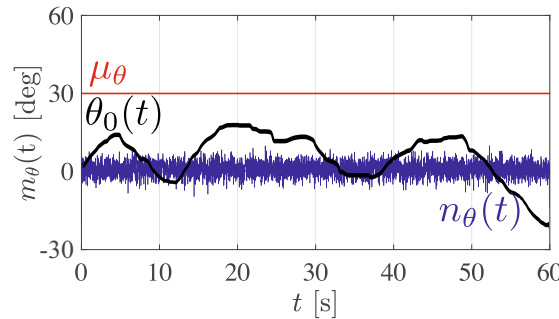


Figure 3.3. An illustration of the componenets of the noisy measurement $m_\theta(t)$, i.e., μ_θ , $\theta_0(t)$, and $n_\theta(t)$.

There are 5 terms that need to be estimated from the random orientation model as expressed in (3.1) and (3.2), i.e., μ_θ , θ_0 , n_θ , ω_0 , and n_ω . Note that μ_ω depends on the direction of a user as illustrated in Figure 3.2. That is, μ_ω is the opposite direction of a user. Therefore, suppose a random waypoint (RWP) are used to model the random mobility of a user [Johnson & Maltz, 1996], then μ_ω will be determined by the direction of the user in each realization. Therefore, μ_ω does not need to be estimated, and it will be defined based on to which direction a user faces. Estimations of μ_θ , θ_0 , n_θ , ω_0 , and n_ω are discussed in the next section.

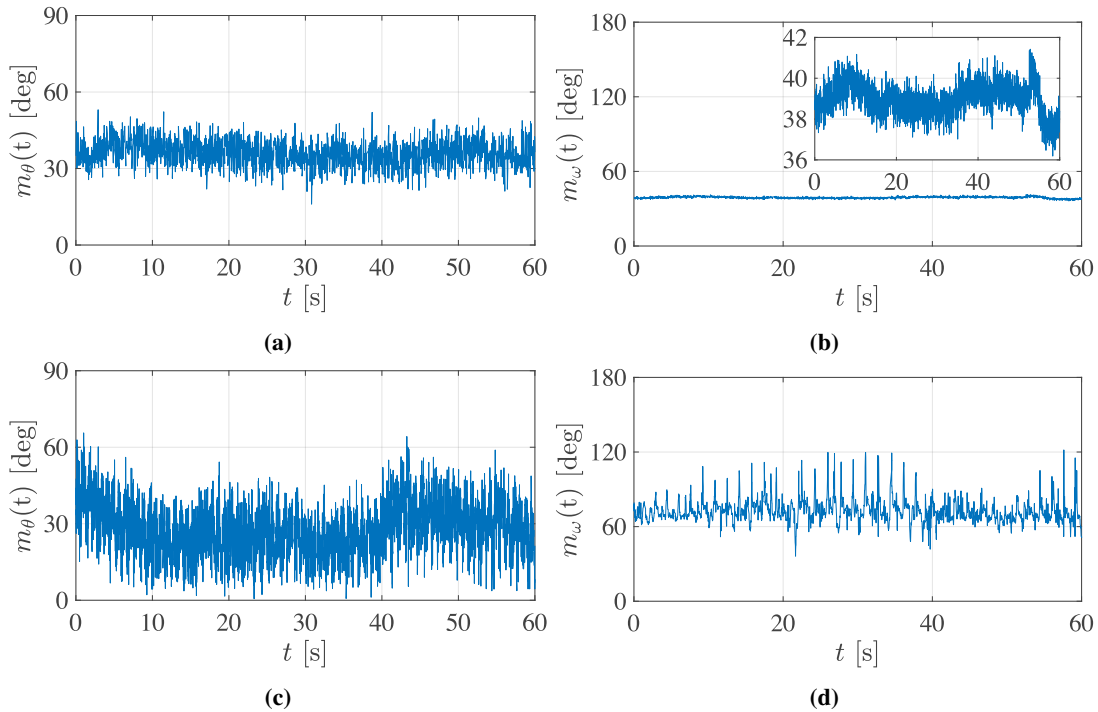


Figure 3.4. Samples of noisy measurement: (a) $m_\theta(t)$ and (b) $m_{\omega|\tilde{\omega}}(t)$ for the sitting activity, (c) $m_\theta(t)$ and (d) $m_{\omega|\tilde{\omega}}(t)$ for the walking activity.

3.5 Random Orientation Model

3.5.1 Noise Estimation: n_θ and n_ω

In order to estimate n_θ and n_ω , a separate measurement was carried out. By using the same device application, 15 data measurements were collected without performing any activity. Samples of $n_\theta(t)$ and $n_\omega(t)$ can be found in Figure 3.5. It is obvious from the figure that the noise variance of ω is greater than that of θ . A more important observation here is that the samples are not equally spaced as shown in the inset of Figure 3.5(a). Consequently, the conventional Fourier analysis, which assumes equally-spaced samples, cannot be used. Instead, an analytical tool that supports unevenly-spaced sampled data, e.g., the Lomb-Scargle periodograms [Scargle, 1982; VanderPlas, 2018], should be used.

The power spectral densities (PSD) of samples given in Figure 3.5 are shown in Figure 3.6. Note that the PSDs of the samples are estimated by using the Lomb-Scargle periodograms. (A brief overview of the Lomb-Scargle periodogram can be found in Appendix B.) The PSDs resemble that of white noises. Therefore, many realizations of zero-mean white noises are generated, and their PSDs are estimated in order to show the similarity. The PSDs of artificial white noise are

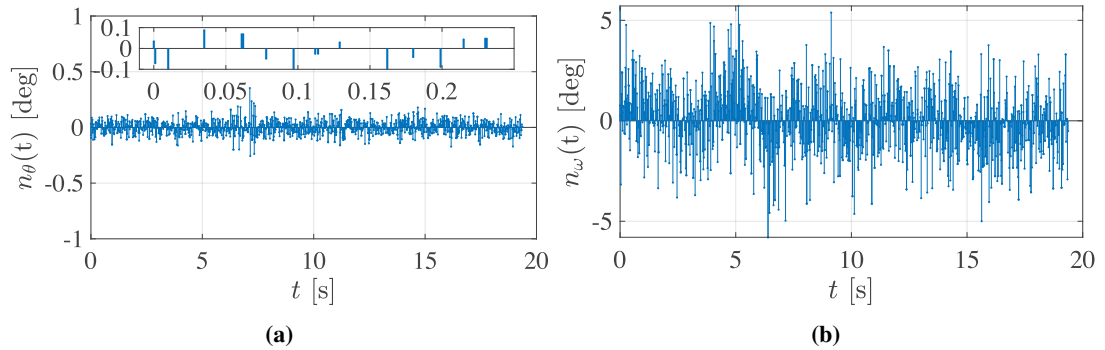


Figure 3.5. A sample of noise measurements for (a) $n_\theta(t)$ and for (b) $n_\omega(t)$.

shown in red curves, where white noises with the variance of 0.0011 is used in Figure 3.6(a), and the variance of 1.0257 is used in Figure 3.6(b). These values are obtained by considering all 15 noise measurements. Therefore, $n_\theta(t)$ and $n_\omega(t)$ are assumed to be zero-mean white noise processes with the variances of 0.0011 and 1.0257, respectively.

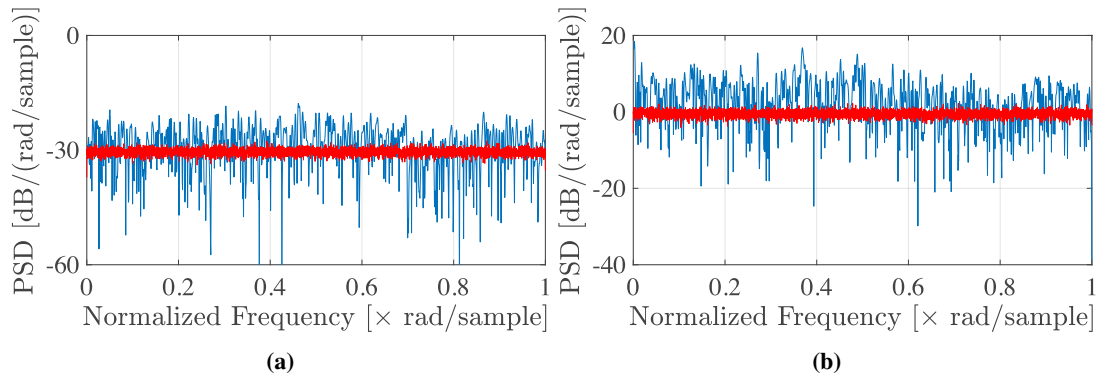


Figure 3.6. (a) PSD of the sample shown in Figure 3.5(a), and (b) PSD of the sample shown in Figure 3.5(b). The red curves are generated by taking the averages of periodograms of many zero-mean white noises with the variances of 0.0011 and 1.0257, respectively.

3.5.2 Tilted Angle Estimation: μ_θ

The term μ_θ from (3.1) is estimated by calculating sample average from each measurement. The probability density functions (PDFs) of μ_θ can be seen in Figure 3.7. The best distribution fitting based on their Kolmogorov-Smirnov distances (KSDs) is shown for each activity. It is shown that the distribution of μ_θ from the sitting activity measurement can be closely approximated with a Laplace distribution. Meanwhile, a Gaussian distribution is more fitted for that of the walking activity. In terms of the mean values μ , the tilted angle for the sitting activity shows that the mobile devices face more towards the ceiling than that of the walking activity. In

terms of the standard deviations σ , the tilted angle for the sitting activity shows less fluctuation compared to that of the walking activity.

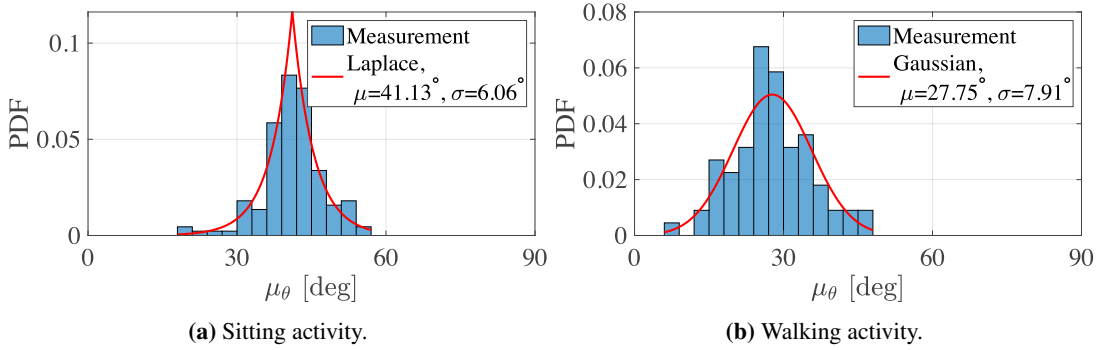


Figure 3.7. PDFs of μ_θ for each activity, where μ and σ denote the mean and the standard deviation, respectively.

3.5.3 Small-Signal Estimation: θ_0 and ω_0

In this subsection, the terms θ_0 and ω_0 in (3.1) and (3.2) are estimated. First, the effect of random sampling will be discussed. Let $w_\theta(t)$ be a window function for $m_\theta(t)$, which is defined as:

$$w_\theta(t) = \begin{cases} 1, & t = t_k \\ 0, & t \neq t_k \end{cases}, \quad (3.3)$$

where $\{t_k\}_{k=0}^{N-1}$ is an arbitrary time sampling. If $\{t_k\}_{k=0}^{N-1}$ is evenly-spaced, and $t_k - t_{k-1} = T$, then $w_\theta(t)$ is a Dirac comb with the interval of T s. The corresponding spectrum of the evenly spaced Dirac comb is another Dirac comb with the interval of $1/T$ Hz. Therefore, sampling a signal with the evenly-spaced time sampling results in a periodic spectrum every $1/T$ Hz. In the frequency domain, this is equivalent to taking a convolution with the Dirac comb that has the interval of $1/T$ Hz. Analogously, the same thing also occurs with unevenly-spaced time sampling. Figure 3.8(a) shows the power spectrum of the window function from one of the $m_\theta(t)$ measurements from the sitting activity. The regular spikes shown in Figure 3.8(a) are known as *partial-aliasing* [VanderPlas, 2018]. The partial-aliasing can be mistaken as harmonics, as shown in Figure 3.8(b). Notice that the harmonics seen in Figure 3.8(b) are aligned with the spikes shown in Figure 3.8(a). Figure 3.8(b) also shows the Nyquist frequency of 500 Hz due to the minimum sampling time of the Physics Toolbox Sensor Suite application [Vieyra Software, 2020] is 1 ms.

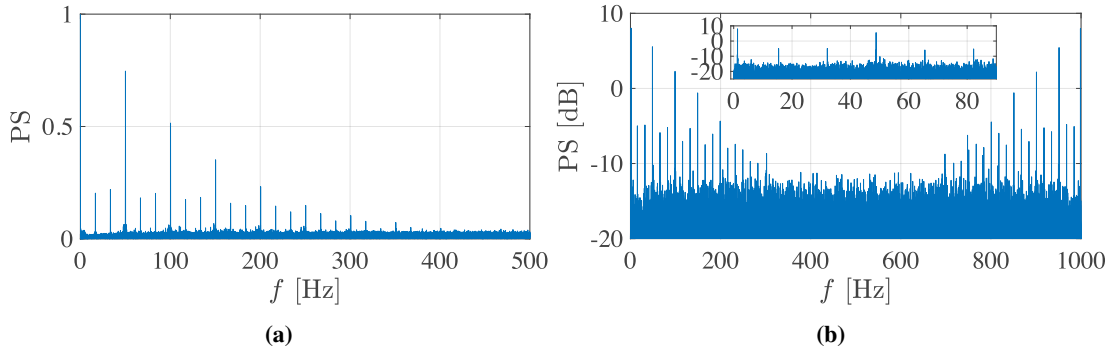


Figure 3.8. (a) The power spectrum of a window function taken from one of the $m_\theta(t)$ measurements from the sitting activity. (b) The power spectrum of the corresponding data.

In order to estimate θ_0 and ω_0 , the effects of μ_θ and μ_ω should be eliminated first by subtracting the measurement samples with the estimated μ_θ and μ_ω , respectively. Then, the effects of the noises $n_\theta(t)$ and $n_\omega(t)$ should be removed too. This is carried out by using a first-order Wiener filter and the results from the noise estimation in Section 3.5.1. Lastly, the partial aliasing should be removed. A typical approach to remove the spurious peaks from the power spectrum is by using the iterative CLEAN¹ algorithm [Baisch & Bokelmann, 1999; Roberts *et al.*, 1987]. Figure 3.9(a) shows the filtering result of the measurement whose power spectrum (PS) is shown in Figure 3.8(b).

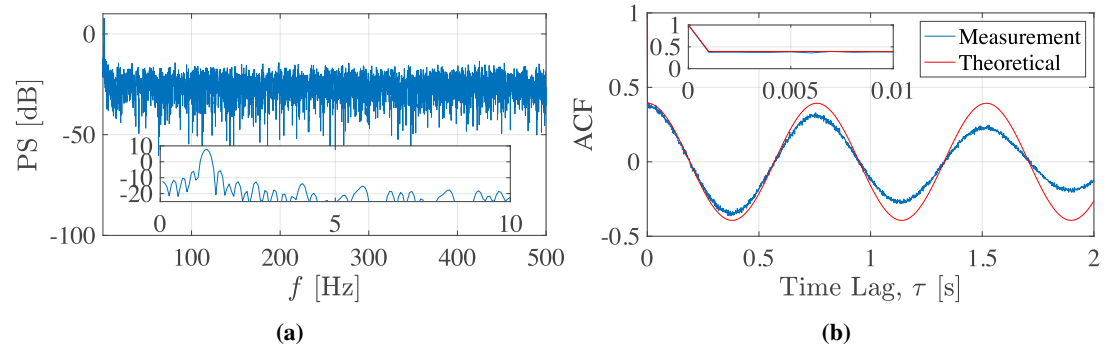


Figure 3.9. (a) A PS of the measurement whose PS is shown in Figure 3.8(b) after being filtered. (b) Its corresponding autocorrelation function.

The PS shown in Figure 3.9(a) resembles that of a harmonic RP, a sinusoid with random phases in white noise. This fact is in line with the finding in [Gresty & Buckwell, 1990]. That is, $\theta_0(t)$

¹To the best of author's knowledge, it is not an abbreviation and first introduced as CLEAN algorithm.

Parameters	Sitting Activity		Walking Activity	
	$\theta_0(t)$	$\omega_0(t)$	$\theta_0(t)$	$\omega_0(t)$
A ($^{\circ}$)	1.88	1.31	3.22	3.15
f (Hz)	0.67	1.46	1.86	1.71
σ_v ($^{\circ}$)	5.91	3.22	7.59	9.48

Table 3.1. Average values of the estimated parameters $\{A, f, \sigma_v\}$ in (3.4) and (3.5).

and $\omega_0(t)$ can be modeled by harmonic RPs and defined as:

$$\theta_0(t) = A_\theta \sin(2\pi f_\theta t + \phi) + v_\theta(t) \text{ and} \quad (3.4)$$

$$\omega_0(t) = A_\omega \sin(2\pi f_\omega t + \phi) + v_\omega(t) \quad (3.5)$$

where:

- ϕ is a random phase following a uniform distribution with the support of $[0, 2\pi]$,
- $v(t)$ is a zero-mean white noise with the variance of σ_v^2 , and
- the set $\{A, f, \sigma_v\}$ is the set of parameters that need to be estimated.

The parameters A and f can be estimated from the PS. For example, $A_\theta = 3.56^{\circ}$ and $f_\theta = 1.32$ Hz based on the PS shown in Figure 3.9(a). The amplitude is obtained from the fact that the value of the peak is $A^2/2$, and the frequency is determined by the location of the peak. The parameter σ_v can be estimated by calculating the autocorrelation function (ACF) from the PS. By taking the inverse discrete Fourier transform (IDFT) of the PS, the corresponding ACF is shown in Figure 3.9(b). The normalized ACF of $\theta_0(t)$ is:

$$R_\theta(\tau) = \mathbb{E}[\theta_0(t)\theta_0(t+\tau)] = \frac{\frac{A_\theta^2}{2} \cos(2\pi f_\theta \tau) + \sigma_{v_\theta}^2 \delta(\tau)}{\frac{A_\theta^2}{2} + \sigma_{v_\theta}^2}. \quad (3.6)$$

The comparison of the ACFs based on the measurement and the theoretical one is shown in Figure 3.9(b). Then, σ_{v_θ} can be approximated by solving (3.6) at $\tau = \delta$, where δ is a very small number. Based on Figure 3.9(b), $R_\theta(\delta) \approx 0.4$. Hence, $\sigma_{v_\theta} \approx 3.08^{\circ}$. By repeating this procedure to all measurement data and taking the average, the final estimated values are shown in Table 3.1.

3.6 Coherence Time of Indoor LiFi Channels

In this section, the proposed random orientation model is used to investigate the coherence time of indoor LiFi channels by means of computer simulations. Computer simulations are chosen due to the fact that we want to obtain a conclusion over many channel realizations in which we consider randomly-oriented devices, random mobile users, and random blockage models. A system model will be discussed first, and then followed by the descriptions of the simulation environments. Then, a result from a realization of a small office environment is discussed before presenting the final result of the coherence time over many realizations.

3.6.1 System Model

A discrete-time CIR model is defined in this subsection. Assume that an IM/DD system is used, and $x_d[k]$ denotes a non-negative discrete-time input signal, i.e., $x_d[k] \geq 0$. The upsampling factor is denoted by T , and the corresponding continuous-time signal is defined as:

$$x_c(t) = \sum_k x_d[k] p_t(t - kT), \quad (3.7)$$

where $p_t(t)$ is a pulse shaping function at a transmitter. Given a linear time-varying channel $h_c(\tau, t)$, the received signal can be expressed as:

$$y_c(t) = \int_{-\infty}^{\infty} h_c(\tau, t) x_c(t - \tau) d\tau, \quad (3.8)$$

where τ denotes a time delay. That is, $h_c(\tau, t)$ denotes a response of the channel at time t to an impulse input transmitted at $t - \tau$. A matched filter $p_r(t)$ is used at the receiver, and the received signal is denoted by $y_c(t)$. A discrete-time received signal $y_d[n]$ is obtained by downsampling the convolution of $y_c(t)$ and $p_r(t)$, i.e.,:

$$y_d[n] = (y_c * p_r)(t)|_{t=nT}. \quad (3.9)$$

Putting together the terms above, the relationship between $y_d[n]$ and $x_d[k]$ can be expressed as:

$$y_d[n] = \sum_l h_d[l, n] x_d[n - l], \quad (3.10)$$

where $l = n - k$. In a time-invariant case, $h_c(\tau, t)$ and $h_d[l, n]$ are simplified to $h_c(\tau)$ and $h_d[l]$. The CIR $h_c(\tau, t)$ will be obtained using simulations. Then, the discrete-time CIR $h_d[l, n]$ is obtained by transmitting an impulse, i.e., $x_d[k] = \delta[k]$.

The discrete-time CIR $h_d[l, n]$ is used to measure the coherence time. Unlike in [Tse & Viswanath, 2005], where a coherence time is calculated based on the Doppler spread, a coherence time is defined as an interval over which $h_d[l, n]$ changes ‘significantly’ with respect to n . The degree of significance will be measured by means of a local scattering function (LSF) [Matz, 2005]. Studies of coherence time in [Matz, 2005] are more relevant to this thesis because:

- the coherence time is evaluated based on the changes of amplitudes in $h_d[l, n]$ with respect to n , which can be applied to IM/DD systems, and
- the study in [Matz, 2005] focuses on non-wide-sense stationary uncorrelated scattering (WSSUS) cases, where it will be shown later that $h_d[l, n]$ is non-WSSUS with the assumption of mobile users.

More details about this topic will be discussed in Chapter 3.6.4.1.

3.6.2 Simulation Environments

3.6.2.1 Small Office Environment

The small office environment in this chapter follows the illustrations described in Chapter 2.3.3. In this scenario, the human model moves arbitrarily inside the room while using the mobile device, for example, as they read Internet articles on their device, as shown in Figure 2.13(a). Three different random mobilities are used in this chapter, i.e., random waypoint [Johnson & Maltz, 1996], random direction [Royer *et al.*, 2001], and the truncated Levy-walk model [Hong *et al.*, 2008]. The entire room is included in the region of mobility, excluding the corner where the desk and the chair are located.

Different activities are assumed here, i.e., the reading and calling activities. In addition, two different locations of the light emitter and receiver are assumed, i.e., on the front screen as shown in Figure 3.10(a) and on top of the mobile device as shown in Figure 3.10(b). The vector \mathbf{n}_u denotes the orientation of the active pair of light emitter and receiver. For the reading activity,

the active pairs of the light emitter and receiver are the ones on the front screen. Meanwhile, the pairs of the light emitter and receiver on top of the mobile device are active for the calling activity.

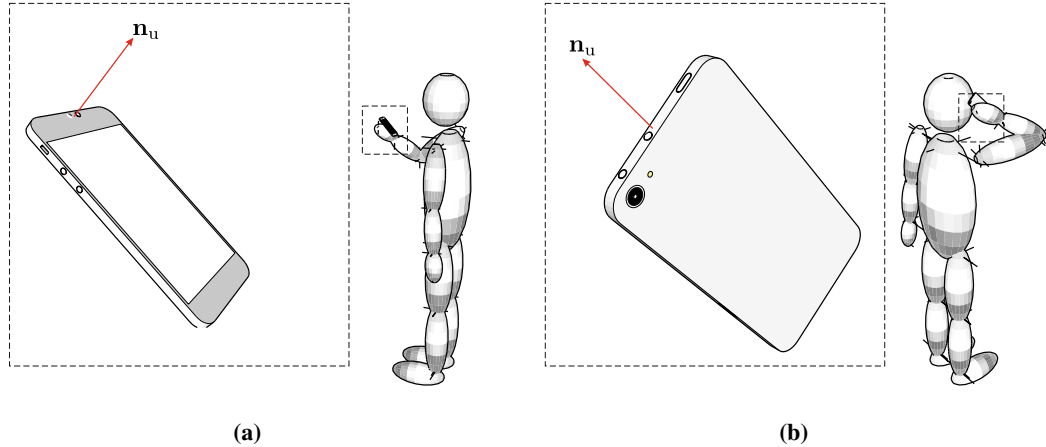


Figure 3.10. (a) The reading activity and (b) the calling activity.

3.6.2.2 Open Office Environment

In addition to the small office environment, an open office environment is also considered in this chapter. The open office environment is an extension of the small office environment, where the room's dimensions are $25 \times 10 \times 3 \text{ m}^3$. The open layout is filled with 8 groups of 4 desks, as shown in Figure 3.11. The number of people working at the desks (which are shown in gray) follows a binomial distribution. There are two people walking around the office, and the mobility area is shown in the pink shaded region in Figure 3.11(b). The user of interest with a calling activity is shown in red.

In terms of materials, we keep the same assumptions as those of the small office environment for simplicity. The distances between APs are 5 m in the x -axis and 4 m in the y -axis.

3.6.3 Specific Case: A Realization of A User's Random Mobility

In this subsection, discussions on a realization of the channel in the small office environment with the user carrying out the reading activity are provided. An uplink transmission is assumed in this case. The main goal of this subsection is to show that, in general, LiFi indoor channels are non-WSSUS.

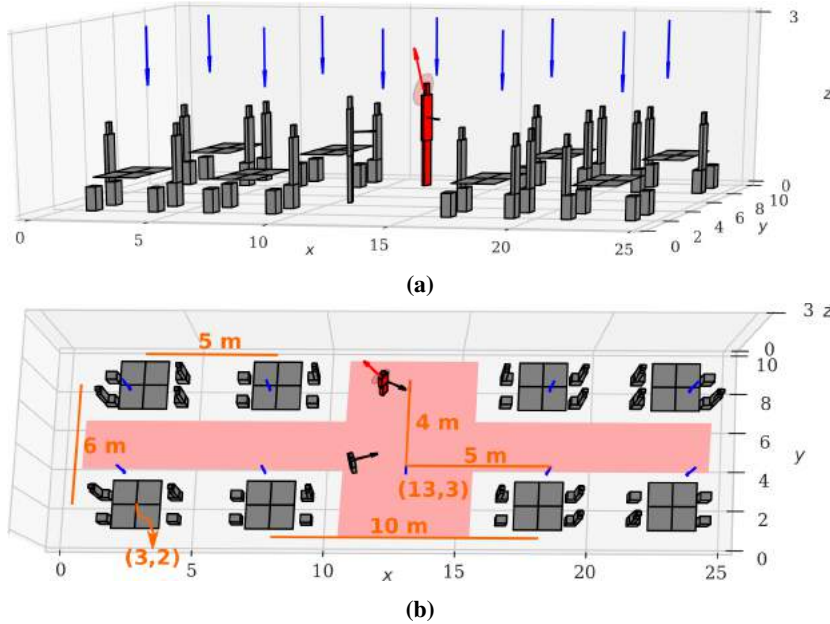


Figure 3.11. (a) A geometry model for the open office environment. The red human model represents the user of interest doing a calling activity. (b) The top view of the open office environment, where the pink area illustrates the mobility area of people.

A realization of the random mobility is shown in Figure 3.12(a). Its corresponding speeds are shown in Figure 3.12(b). In this section, for the simplicity of our discussion, we will slightly abuse the definition of v so that it also refers to its corresponding path. For example, when the user moves from $(1.97, 1.87)$, which is the start point, to $(1.42, 1.79)$ with a speed of $v_0 = 0.52$ m/s, we will refer to such mobility with the path v_0 .

Figure 3.12(c) depicts the LoS portion of the CIR, i.e., the DC channel gain as defined in (2.7). In the end of path v_1 , there is a blocking event, which makes the received signal from the LoS link zero. During the path v_2 , the gain of the LoS link increases as the user approaches the AP, and it decreases as the user moves away from the AP. As a comparison Figure 3.13 shows another set of realizations. The mean of the DC channel gain in Figure 3.13(c) is 1.9×10^{-4} , while the mean DC channel gain in Figure 3.12(c) is 0.8×10^{-4} . It is obvious that $h_c(\tau, t)$ does not follow the WSS assumption, as the mean is not constant over different realizations. This fact is also commonly found in RF cases when the shadowing assumption is incorporated [Matz, 2005]. In the LiFi case with realistic assumptions, the non-WSS phenomenon can be justified by the fact that there is a non-zero probability that the LoS link is blocked for mobile users. In addition, a justification can be made based on the fact that the attenuation of the channel decreases as the mobile device approaches the AP. Therefore, in general, the CIRs will

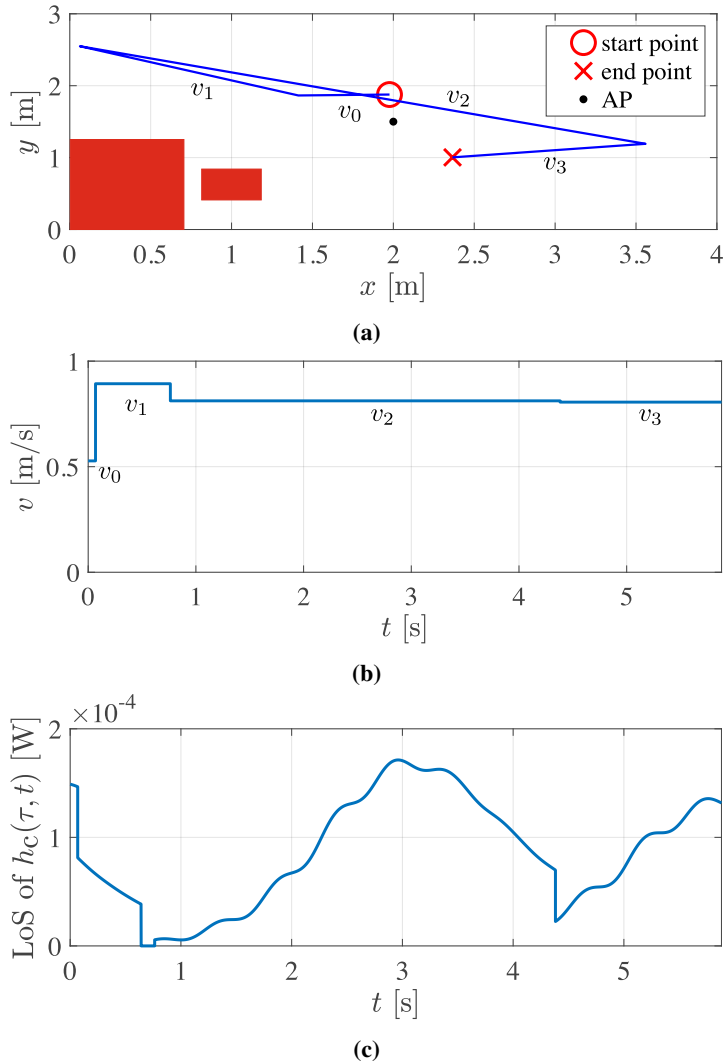


Figure 3.12. (a) A realization of random mobility in the small office environment. (b) The corresponding speed vs. time graph. (c) LoS of the CIR.

be assumed to be non-WSS.

The corresponding discrete-time CIRs of the realization shown in Figure 3.12(a) can be seen in Figure 3.14 with different bandwidth B . It is obvious that the greater the bandwidth, the greater the number of channel taps l is. The main reason for this is that the typical delay spread of a LiFi channel is in the order of 1 ns to 20 ns [Kahn & Barry, 1997, Fig. 13], while the symbol period of a signal with $B = 80$ MHz is 6.25 ns. A more important observation is shown in the insets of Figure 3.14(a) and Figure 3.14(b). That is, the amplitudes of the discrete-time CIRs in the first tap ($l = 1$) highly correlate to those in the zeroth tap. This fact shows that indoor LiFi channels do not follow the uncorrelated scatterers assumption, which is widely used in

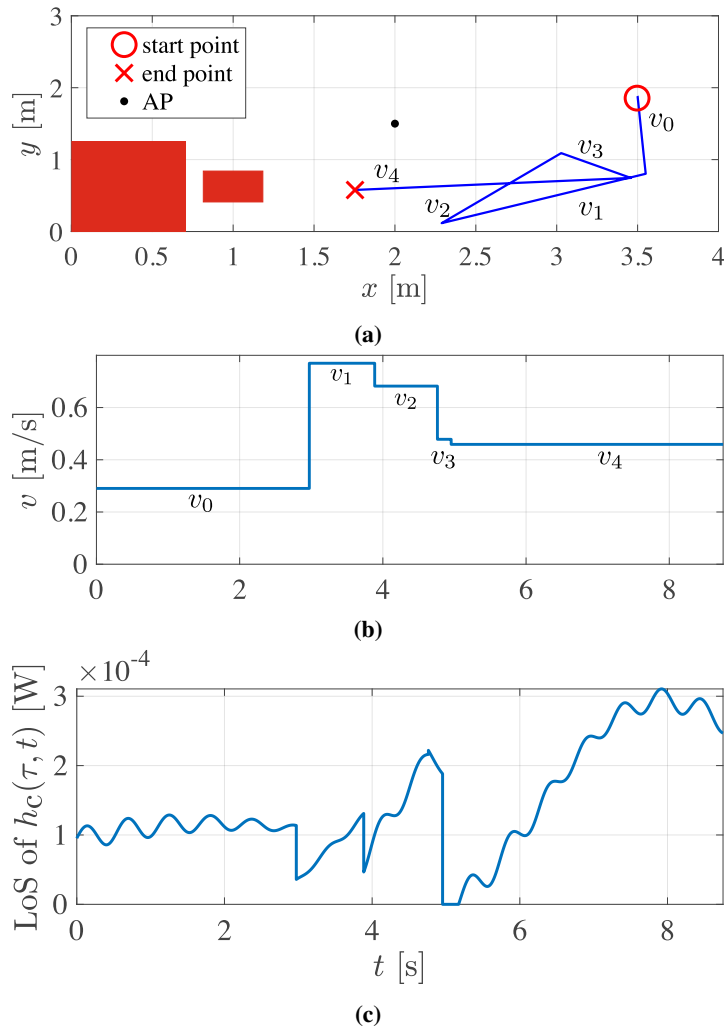


Figure 3.13. (a) Another realization for a comparison with Figure 3.12(a). (b) The corresponding speed vs. time graph. (c) LoS of the CIR.

RF studies [Bello, 1963]. Based on [Matz, 2005], if the scenario is made more realistic, the uncorrelated scatterers assumption is violated, especially for cases where received signals can come from the same reflecting objects. This justification is also relevant in the indoor LiFi channels. Therefore, the non-WSSUS assumption will be used in the study of the coherence time of the indoor LiFi channels.

Bandwidth can also affect the coherence time, which will be discussed in Chapter 3.6.5. The effect of bandwidth on the coherence time can be discussed by looking at the fluctuation of the magnitude response of the wireless optical channels. It will be shown in Section 3.6.4.1 that the magnitude response is the fundamental component to calculate the coherence time based on the framework proposed in [Matz, 2005; Herdin *et al.*, 2005; Paier *et al.*, 2008; Bernadó

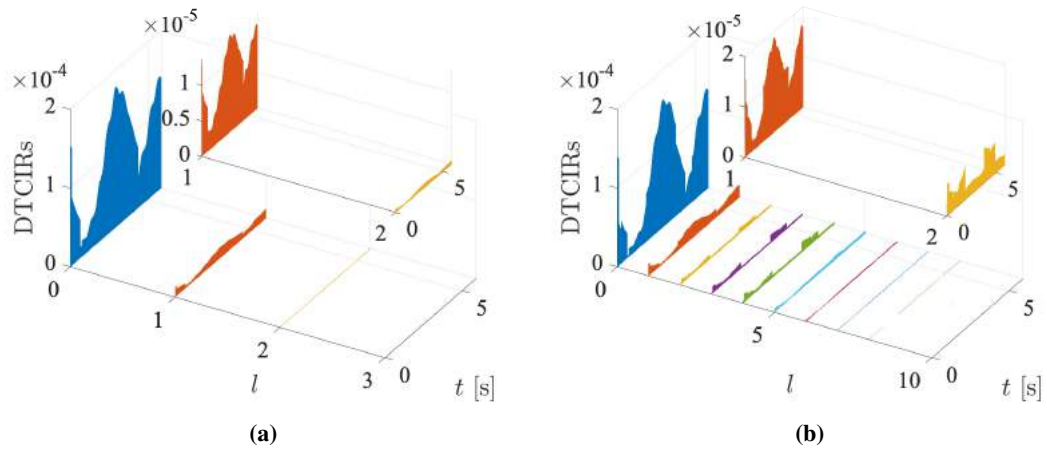


Figure 3.14. The discrete-time CIRs (DTCIRs) w.r.t. the mobility sample shown in Figure 3.12(a) with (a) $B = 20$ MHz and (b) $B = 80$ MHz.

et al., 2012]. Figure 3.15 depicts the normalized magnitude response of samples shown in Figure 3.14(a). Suppose $H(f, t)$ is a frequency response of the channel, and the power spectral density of transmitted signal is $S_X(f, t)$, then the average received power of the signal at time t is $\int |H(f, t)|^2 S_X(f, t) df$. It can be seen from Figure 3.15(b) that the magnitude response has more fluctuations with a wider bandwidth. Therefore, we can expect that as we increase the bandwidth B , the average received power will fluctuate more as it is proportional to $|H(f, t)|^2$. Consequently, we will see later that the coherence time will be smaller.

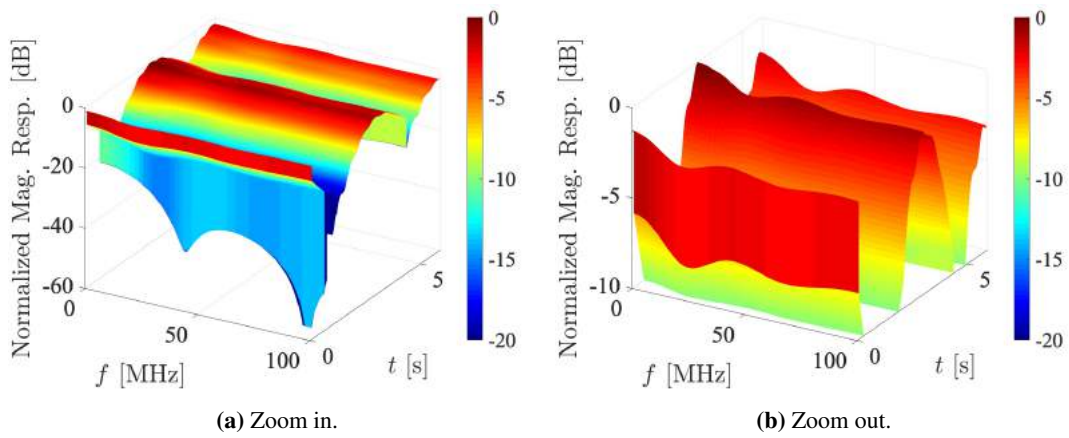


Figure 3.15. Normalized magnitude response of wireless optical channel corresponded to the mobility sample shown in Figure 3.12(a).

3.6.4 Coherence Time of The Specific Case

In the previous subsection, the justification for the non-WSSUS is discussed. In order to calculate the coherence time for non-WSSUS, an analytical tool from [Matz, 2005], which is based on LSF, is used. Therefore, before presenting the result, a brief overview of LSF will be provided.

3.6.4.1 Local Scattering Function and Collinearity

Based on [Matz, 2005; Herdin *et al.*, 2005; Paier *et al.*, 2008; Bernadó *et al.*, 2012], the coherence time is calculated based on the notion of local stationary regions. A stationarity region is first found by defining a *minimum stationarity region* such that the WSSUS assumption holds. Then, this region is gradually increased, and the neighboring LSFs are measured. This process continues while the neighboring LSFs are similar, which is measured by its collinearity [Herdin *et al.*, 2005; Paier *et al.*, 2008; Bernadó *et al.*, 2012]. Finally, the coherence time is defined as a time range where the corresponding collinearity exceeds a threshold [Paier *et al.*, 2008].

A basic ingredient in estimating LSFs is the discrete version of the frequency response of $h_d[l, n]$, i.e., $H[q, n]$, where $q \in \{0, 1, \dots, Q - 1\}$, and Q is the number of frequency bins. The frequency bins are chosen such that the frequency f is evenly partitioned. Similarly, let S be the total number of samples in the time domain. The Q and S samples are partitioned into multiple of U and P samples, respectively. The $U \times P$ under-tested stationary region is indexed by (k_f, k_t) , where:

$$k_t \in \{1, \dots, \lfloor S/P - 1 \rfloor\}$$

and

$$k_f \in \{1, \dots, \lfloor Q/U - 1 \rfloor\}.$$

The collinearity, which is denoted by $\gamma[k_t, k_t + \Delta k_t]$, is bounded from 0 to 1, where the value of 1 indicates similarity. Based on [Paier *et al.*, 2008], the collinearity is defined as:

$$\gamma_t[k_t, k_t + \Delta k_t] = \frac{\sum_{u=0}^{U-1} \sum_{p=-P/2}^{P/2-1} \sum_{k_f=1}^{\lfloor Q/U - 1 \rfloor} L[k_f, k_t; u, p] L[k_f, k_t + \Delta k_t; u, p]}{\|L[k_f, k_t; u, p]\|_2 \|L[k_f, k_t + \Delta k_t; u, p]\|_2}, \quad (3.11)$$

where L is the LSF estimator, and it is defined as:

$$L[k_f, k_t; u, p] = \frac{1}{IJ} \sum_{w=0}^{IJ-1} |\mathcal{H}_w[k_f, k_t; u, p]|^2, \text{ where} \quad (3.12)$$

$$\mathcal{H}_w[k_f, k_t; u, p] = \sum_{p'=-P/2}^{P/2-1} \sum_{q'=-U/2}^{U/2-1} H[q, n] W_w[p', q'] e^{-j2\pi(pp' - uq')}, \quad (3.13)$$

where $q = k_f U + q'$, $n = k_t P + p'$, and $I = J = 3$ [Bernadó *et al.*, 2012]. The term W is a taper that typically employs a discrete prolate spheroidal sequences (DPSS) window [Paier *et al.*, 2008; Bernadó *et al.*, 2012]. Let $\alpha[k_t, k_t + \Delta k_t]$ be an indicator function, which is defined as:

$$\alpha[k_t, k_t + \Delta k_t] = \begin{cases} 1, & \gamma[k_t, k_t + \Delta k_t] > \alpha_{\text{th}} \\ 0, & \text{otherwise} \end{cases}, \quad (3.14)$$

where α_{th} is a threshold, and as a rule-of-thumb, it is typically equal to 0.9 [Paier *et al.*, 2008]. Then, the stationary time T_{stat} is defined as:

$$T_{\text{stat}}[k_t] = T \sum_{k'_t \in \mathcal{K}} \alpha[k_t, k'_t], \quad (3.15)$$

where:

$$\mathcal{K} = \left\{ k + \Delta k_t \mid \Delta k_t \in \left\{ 0, 1, \dots, \left\lfloor \frac{S-P}{P} \right\rfloor - k_t \right\} \text{ and} \right. \quad (3.16)$$

$$\left. \alpha[k_t, k_t + \Delta k_t] \text{ consecutively has value of 1} \right\}. \quad (3.17)$$

For example, if $k_t = 0$ and:

$$\alpha[k_t, k_t + \Delta k_t] = [\underbrace{1, 1, 1, 1}_{\mathcal{K}}, 0, 0, 1, 1, 0], \quad (3.18)$$

then $\mathcal{K} = \{0, 1, 2, 3\}$. The reason for this exclusion is that in this thesis we focus on a worst-case scenario, where the channel must be strictly similar within a coherence time.

Conversion: The index k_t is discrete, and it is not straightforward to translate it into a time instance t , which has a more meaningful physical interpretation. Recall that there are S discrete-time CIRs, i.e., $n \in \{0, 1, \dots, S-1\}$, which is obtained by sampling every T sec-

ond. S samples are then divided into multiple of P samples, and it is indexed by k_t such that $k_t \in \{1, \dots, [S/P - 1]\}$. The relationship of k_t and n is $n = k_t P + p'$, where $p' \in \{-P/2, \dots, P/2 - 1\}$. Then, a corresponding time instance can be obtained by using $t(nT) \triangleq t[n]$. The same conversion also applies for Δk_t and Δt .

3.6.4.2 Specific Case: Results and Discussions

Figure 3.16 shows the collinearity of the discrete-time CIRs shown in Figure 3.14(a) with $B = 20$ MHz. Note that k_t and Δk_t are converted to time instance t so that we can easily compare it with that in Figure 3.12. In addition, only results with $\Delta t > 0$ are shown, which shows the similarities shared with future samples. The collinearity at particular time instances gives a better insight. The collinearities at $t = 0.25$ s and at $t = 1.27$ s are shown in Figure 3.17. The coherence time at $t = 0.25$ s is 0.359 s, which means that the samples in Figure 3.14(a) at $t = 0.25$ are similar for the next 0.359 s. Longer coherence time is shown at $t = 1.27$ s, which is $T_{\text{stat}} = 0.608$ s. These results are intuitive as based on samples in Figure 3.14(a), the amplitudes have more fluctuations at $t < 1$ s.

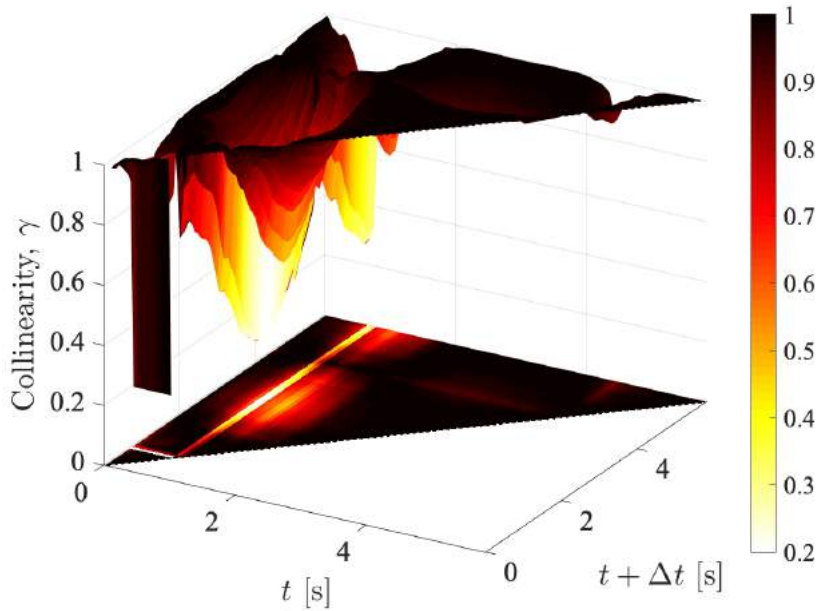


Figure 3.16. Collinearity of the discrete-time CIRs shown in Figure 3.14(a), i.e., $B = 20$ MHz.

All stationary times and their CDF are shown in Figure 3.18. The minimum value of T_{stat} is 164

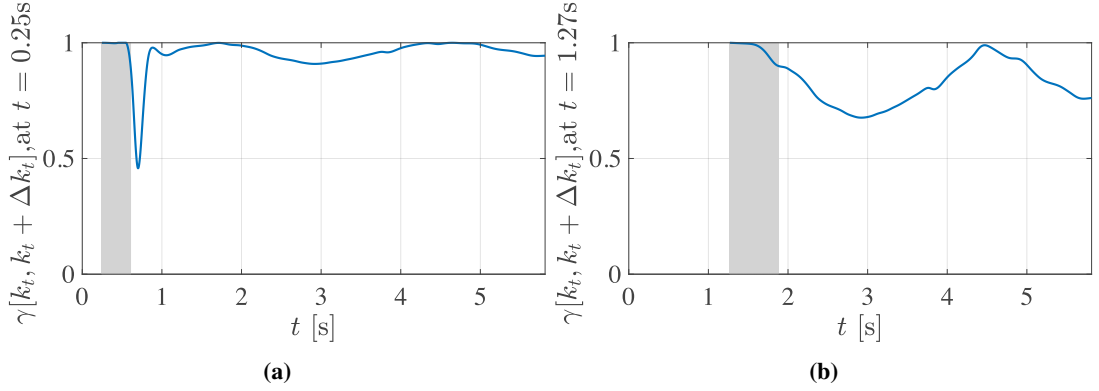


Figure 3.17. Collinearities at different time instances, i.e., (a) $t = 0.25$ s and (b) $t = 1.27$ s. The shaded areas denote T_{stat} , where $T_{\text{stat}} = 0.359$ s for (a) and $T_{\text{stat}} = 0.608$ s.

ms. The mean and the standard deviation of T_{stat} are 1.65 s and 1.17 s, respectively. The 5% lower and upper confidence intervals are 0.232 s and 3.71 s, respectively. With these results and this particular case, LiFi is suitable for applications with a delay requirement of less than 100 ms. For example, LiFi can be integrated into SDN-based HetNets, which are based on [He *et al.*, 2015], the delay requirement is around 40 ms. In the next subsection, comprehensive results of general cases with various average speeds, random mobility models, signal bandwidths, and scenarios are discussed.

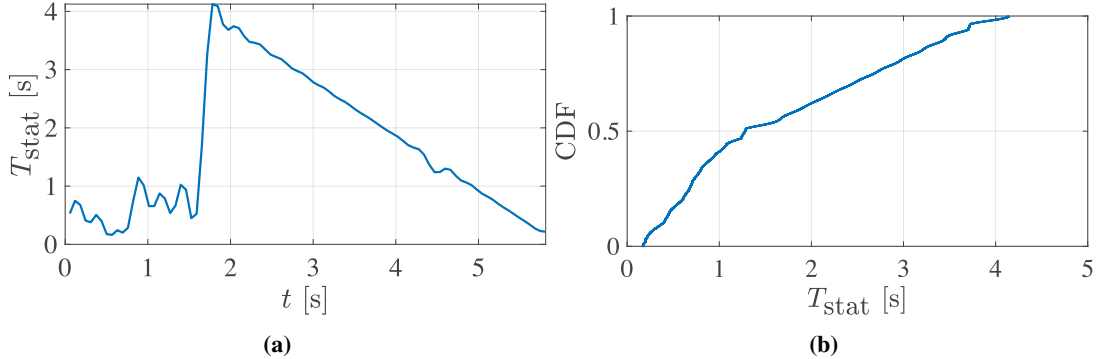


Figure 3.18. (a) The stationary time, and (b) its CDF.

3.6.5 Results and Discussions

3.6.5.1 Small Office Environment

For the small office environment, 30,000 realizations for a target average speed of the user, i.e., 0.5 m/s and 1 m/s, are generated. Different realizations are generated for downlink and uplink transmissions. In this section, the downlink transmission is carried out over the 940 nm

Scenario		UL T_{stat}	DL T_{stat}
Avg. speed ≈ 0.5 m/s, $B = 20$ MHz	min	95 ms	92 ms
	5% CB	145 ms	139 ms
	mean	964 ms	950 ms
Avg. speed ≈ 1 m/s, $B = 20$ MHz	min	58 ms	53 ms
	5% CB	67 ms	61 ms
	mean	495 ms	489 ms
Avg. speed ≈ 0.5 m/s, $B = 80$ MHz	min	69 ms	63 ms
	5% CB	82 ms	78 ms
	mean	878 ms	871 ms
Avg. speed ≈ 1 m/s, $B = 80$ MHz	min	42 ms	41 ms
	5% CB	49 ms	46 ms
	mean	448 ms	439 ms

CB: confidence bound, DL: downlink, UL: uplink

Table 3.2. Coherence time of the small office environment.

wavelength spectrum, and the 850 nm wavelength spectrum is used for the uplink transmission. These realizations are obtained from samples of three different random mobility models, i.e., random waypoint [Johnson & Maltz, 1996], random direction [Royer *et al.*, 2001], the truncated Levy-walk model [Hong *et al.*, 2008] with a maximum waiting time of 1 s. Each realization of these mobilities consists of one or more activities, i.e., the reading and calling activity, which emulate different activities while walking.

All results for the small office environment are summarized in Table 3.2. Three different statistics, which are the minimum value, the 5% lower confidence bound, and the mean value, are presented. A general observation of the results is that all statistics are above 40 ms even with the average speed of 1 m/s and signal bandwidth of 80 MHz. The coherence time for the uplink channel is better than that of the downlink channel. The main reason for this is that the reflectivities at 940 nm are higher than those at 850 nm. Therefore, higher power signals are received from different propagation paths [Al-Kinani, Wang, Zhou, & Zhang, 2018]. Consequently, the CIRs have more fluctuations. Increasing the signal bandwidth also lowers the coherence time. The intuition of this fact has been discussed previously, please see discussions about Figure 3.15.

3.6.5.2 Open Office Environment

For the open office environment, instead of 30,000, 3,000 realizations for each scenario are generated. Note that the number of APs is $A = 10$. Suppose $a \in \mathcal{A} = \{0, 1, \dots, A - 1\}$

Scenario		UL T_{stat}	DL T_{stat}
Avg. speed ≈ 0.5 m/s, $B = 20$ MHz	min	91 ms	82 ms
	5% CB	119 ms	111 ms
	mean	928 ms	919 ms
Avg. speed ≈ 1 m/s, $B = 20$ MHz	min	46 ms	41 ms
	5% CB	58 ms	55 ms
	mean	467 ms	463 ms
Avg. speed ≈ 0.5 m/s, $B = 80$ MHz	min	66 ms	60 ms
	5% CB	72 ms	71 ms
	mean	688 ms	675 ms
Avg. speed ≈ 1 m/s, $B = 80$ MHz	min	34 ms	32 ms
	5% CB	42 ms	40 ms
	mean	401 ms	394 ms

CB: confidence bound, DL: downlink, UL: uplink, $\Phi_{1/2}$: half-power semiangle

Table 3.3. Coherence time of the open office environment.

is the index of the AP, P_a is the average received power from or at the a^{th} AP (depending on the downlink or uplink transmissions), $h_d^{(a)}[l, n]$ is the discrete-time CIR of the user that is associated with the a^{th} AP, then:

$$h_d[l, n] = \left\{ h_d^{(x)}[l, n] \middle| x = \arg \max_{a \in \mathcal{A}} P_a \right\}, \forall n, \quad (3.19)$$

which at discrete-time instance n , the discrete-time CIR is chosen from the CIRs which have the highest average received power.

Table 3.3 summarizes the results for the open office environment. Generally, the coherence time is lower than that in the small office environment. It is worth noting here that with the average speed of 1 m/s and the bandwidth of 80 MHz, in the worst case, the coherence time is slightly below 40 ms. However, the 40 ms delay is also the worst case in the delay measurement reported in [He *et al.*, 2015]. The median value reported in [He *et al.*, 2015] is in the range of 20 ms to 30 ms, which depends on what SDN rule is measured. In addition, based on the 5% lower confidence bound, 95% of the measured coherence time has a coherence time greater than 43 ms. In this case, applying LiFi in very high bandwidth and with a moderate user's speed is still feasible.

3.7 Summary

In this chapter, a random orientation model was discussed. The random orientation model was proposed based on measurement data. The emphasis was put on the fact that the sampled data was not evenly-spaced, which violated the uniform sampling assumption of the conventional Fourier analysis. The Lomb-Scargle method which could accommodate non-uniform sampling was used instead. The proposed random orientation model was a harmonic RP, which is a sinusoid with a random phase in white noise. Then, the random orientation model was combined with the random mobility of a user and random blockage to study the coherence time of indoor LiFi channels. It was shown that the non-WSSUS assumption should be used. The key usage of the coherence time study is that LiFi could be a part of future HetNets which are envisioned to utilize the SDN paradigm. The reason for this is that a delay requirement for the SDN rules in existing SDN-enabled switches is 40 ms, and it has been shown in this chapter that the coherence time of indoor LiFi channels is greater than 40 ms.

Chapter 4

Modulation: Single-Carrier and Multi-Carrier

4.1 Introduction

In the previous chapters, the channel model and its characteristics have been presented. In this chapter, both single and multi-carrier modulation techniques will be discussed. There are different motivations why this thesis considers both modulation techniques. A single-carrier modulation is mainly considered due to its power efficiency [Proakis, 2007]. Meanwhile, multi-carrier one is superior in terms of its spectral efficiency [Proakis, 2007]. An important conclusion of the comparison between the two modulation techniques for OWC can be drawn from [Nuwanpriya *et al.*, 2015] as shown in Figure 4.1. The general conclusion is that PAM-SCFDE, which is a single-carrier modulation, is better than enhanced unipolar (eU)-OFDM [Tsonev & Haas, 2014], which is a multi-carrier modulation, at a lower range of spectral efficiency. Meanwhile, multi-carrier modulations are better than single-carrier ones at a high range of spectral efficiency. It means that both schemes do not always dominate each other. Therefore, in a particular case where a system designer wants to take advantage of the power efficiency and spectral efficiency traits of single-carrier and multi-carrier modulation methods, the system designer can employ both approaches. For example, based on the IEEE 802.11ad technical specification (WiGig), a single-carrier modulation technique is used to have a power-efficient system, and an OFDM-based modulation technique is used to have a spectral-efficient system [IEEE P802.11 TGad, 2012]. The same motivation is also applied in this thesis. This thesis discusses different modulation techniques that excel either at lower or higher spectral efficiencies. Therefore, depending on the spectral efficiency region, systems designers can choose from various modulation techniques that have a better performance at the spectral efficiency region of interest.

For completion purposes, it is worth discussing how comprehensive the comparisons are conducted in [Nuwanpriya *et al.*, 2015]. There are only four different techniques that are compared, as shown in Figure 4.1, i.e., PAM-SCFDE [Nuwanpriya *et al.*, 2015], decomposed quadrature

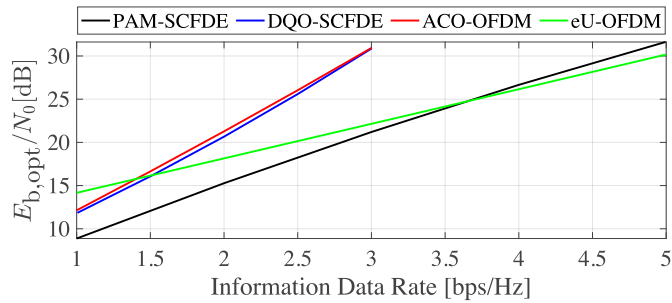


Figure 4.1. The comparisons of different modulation techniques at different spectral efficiencies taken from [Nuwanpriya *et al.*, 2015].

optical (DQO)-SCFDE [Acolatse *et al.*, 2011], asymmetrically clipped optical (ACO)-OFDM [Armstrong & Lowery, 2006], and eU-OFDM [Tsonev & Haas, 2014]. The DQO-SCFDE [Acolatse *et al.*, 2011] is considered because it outperforms ACO [Armstrong & Lowery, 2006] and repetition and clipping optical (RCO)-SCFDE [Acolatse *et al.*, 2011]. Therefore, the latter modulation techniques are not discussed in [Nuwanpriya *et al.*, 2015]. The same reason also applies to PAM-SCFDE. That is, PAM-SCFDE is a generalization of on-off-keying modulation (OOK)-SCFDE, and it is superior compared to pulse position modulating (PPM)-SCFDE [Hsieh & Shiu, 2006]. Moreover, ACO-OFDM has a similar performance compared to unipolar (U)-OFDM, Flip-OFDM, and position modulating (PM)-OFDM. In addition, eU-OFDM is shown to be better than DC-OFDM. Hence, U-OFDM [Tsonev *et al.*, 2012], Flip-OFDM [Fernando *et al.*, 2011], PM-OFDM [Nuwanpriya *et al.*, 2012], and DC-OFDM [Carruthers & Kahn, 1994] are not considered in [Nuwanpriya *et al.*, 2015]. Therefore, it is sufficient to compare PAM-SCFDE, DQO-SCFDE, ACO-OFDM, and eU-OFDM in [Nuwanpriya *et al.*, 2015].

4.2 Contributions of This Chapter

The primary contribution of this chapter is the improvements made for existing modulations techniques. That is, PAM-SCFDE is used as a foundation for the study of single-carrier modulations. First, non-linear equalizers, e.g., DFE and THP, are used to improve PAM-SCFDE. Then, PAM-SCFDE is enhanced by adopting IM, namely SC-GTIM. Regarding the multi carrier modulation, the common mode PHY is improved by using a proposed system that is referred to as IQ-WDM. Lastly, both single carrier and multi carrier modulations are compared in Section 4.7.

4.3 Related Works

There are two foci in this chapter. Firstly, enhanced versions of PAM-SCFDE will be discussed. Secondly, an agreed OFDM system in the TGbb is elaborated. The reason for explaining the enhanced versions of PAM-SCFDE is because of the lack of further studies on PAM-SCFDE, which is in contrast to the number of studies of the IM/DD-based OFDM systems. For example, the use of bit-and-power allocation algorithms for the OFDM systems has been discussed in [Vučić *et al.*, 2010; Zhengguo *et al.*, 2012; Khalid *et al.*, 2012; Bykhovsky & Arnon, 2014; Lu *et al.*, 2014; Wei *et al.*, 2016]. Using the same reason, there are also not many studies that investigate the TGbb-agreed OFDM systems that reuse an RF-based OFDM chipset for LiFi. Specifically, TGbb agreed to use the OFDM waveform from IEEE 802.11ax for the common mode of the IEEE 802.11bb [Serafimovski, Han, Weszely, *et al.*, 2019]. (Note that a brief overview of the IEEE 802.11ax standard is provided in the Appendix C.) There is also a discussion on the use of a single-carrier modulation technique for the IEEE 802.11bb, but it might be left for one of the optional modes [Kim *et al.*, 2019].

A direct approach to improve PAM-SCFDE is to first look at it from a general perspective based on [Scaglione *et al.*, 1999]. That is, PAM-SCFDE is a block transmission system with a CP and a linear feed-forward equalizer filter at the receiver, which is optimized based on the MMSE criterion. The LE can be further improved by combining it with a non-linear equalizer, such as a DFE [Xu *et al.*, 2006], or a precoder, such as a THP [Tomlinson, 1971; Harashima & Miyakawa, 1972]. The study of PAM-SCFDE with an LE, a DFE, and a THP under a redundant filter-bank framework [Scaglione *et al.*, 1999] is discussed in [Purwita, Chen, *et al.*, 2019]. Other than [Purwita, Chen, *et al.*, 2019], there are not many studies on DFE and THP. Even if there is such a study, it only considers them separately, i.e., they are not discussed under a framework as in [Purwita, Chen, *et al.*, 2019]. An example of such a study can be found in [Komine *et al.*, 2009], where a DFE is compared with an LE in different scenarios. Therefore, in order to get a comprehensive view of PAM-SCFDE, the results from [Purwita, Chen, *et al.*, 2019] will be discussed first. Then, using the redundant filter-bank framework, the IM [Abu-alhiga & Haas, 2009] can be adopted to improve the PAM-SCFDE as proposed in [Purwita, Yesilkaya, *et al.*, 2019; Purwita *et al.*, 2020]. The combination of IM and PAM-SCFDE will be referred to as SC-GTIM. An important issue that is not discussed in [Nuwanpriya *et al.*, 2015] is the effect of DC wander. However, based on [Grobe *et al.*, 2016], the effect of DC wander is negligible if the ratio of bitrate and the HPF's cut-off frequency is greater than 50% for OOK and 150% for

8-PAM. It is obvious from Figure 2.7 that the ratio with a 20 MHz bandwidth is 77% for OOK and 230% for 8-PAM. Therefore, the effect of the DC wander can be ignored in this thesis.

As previously mentioned, in addition to the single-carrier modulation, TGbb-agreed OFDM systems [Serafimovski, Han, Weszely, *et al.*, 2019] are discussed in this thesis. Discussions of OFDM systems dominate the majority of sessions during TGbb meetings. Specifically, the discussions are mostly about the use of PHY of IEEE 802.11ax [IEEE P802.11 TGax, 2018] or International Telecommunication Union - Telecommunication Standardization Sector (ITU-T) G.9991 (also known as G.vlc) [ITU-T G.9991, 2019] for IEEE 802.11bb. The latter approach supports DC-OFDM and ACO-OFDM with the bit-and-power allocation. However, it has been agreed that these techniques will be used for the optional mode [Serafimovski, Han, Weszely, *et al.*, 2019]. The main reason for this is that the bit-and-power allocation introduces an additional complexity, it is not always required in most LiFi scenarios, as discussed in the study of the flatness of LiFi channels [Purwita & Haas, 2020b; Purwita *et al.*, 2019]. Note that the bit-and-power allocation of OFDM-based OWC has been discussed in many studies, e.g., [Vučić *et al.*, 2010; Zhengguo *et al.*, 2012; Khalid *et al.*, 2012; Bykhovsky & Arnon, 2014; Lu *et al.*, 2014; Wei *et al.*, 2016]. Therefore, this thesis only discusses the use of IEEE 802.11ax's PHY to IEEE 802.11bb. Specifically, the comparison between the common mode and the proposed method in [Purwita & Haas, 2020a] is presented in this chapter. The proposed technique, which is referred to as IQ-WDM, takes advantage of the fact that the diffuse link of LiFi channels has a low pass filter characteristic [Jungnickel *et al.*, 2002]. Hence, instead of working in the pass-band region, the output waveform is converted into baseband, and the IQ signals are transmitted over different wavelengths. A similar technique has been discussed in [Chen *et al.*, 2017]. The main difference with the discussion in [Purwita & Haas, 2020a] is that it is not tailored to the PHY of IEEE 802.11ax.

4.4 Improving PAM-SCFDE with Non-Linear Equalizers

One of the contributions of this thesis in studies of single-carrier modulations is the incorporation of the light emitter's linear region. First, a subsection will be dedicated to discussing the linear region. Then, PAM-SCFDE will be rewritten under the framework of the redundant filter-bank framework [Scaglione *et al.*, 1999] and the linear region. Next, DFE and THP are individually added into PAM-SCFDE.

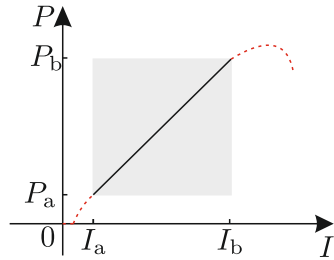


Figure 4.2. An abstraction of linear region, where the black line with a shaded region denotes the linear region, and the red lines denotes the non-linear curves.

4.4.1 Linear Region of Light Emitters

Throughout this thesis, the transmitted signal is assumed to be DC-biased such that it fits a linear region of a light emitter. The primary justification for this is based on the common practice for conducting experiments. Before carrying out an experiment, an optimal peak-to-peak current or voltage and an optimal DC bias are predetermined. One of the methods is described in [Chun *et al.*, 2018, Fig. 2]. A sinusoidal signal is transmitted, and an optimal peak-to-peak and an optimal DC bias are tuned such that the received signal has the maximum peak-to-peak value, and the signal is not distorted. Using the same approach, an experiment in [Bian *et al.*, 2019], which uses off-the-shelf LEDs, reports that the DC bias is in the order of 3 V, and the maximum peak-to-peak voltage is 300 mV. In another sample from custom-designed series-biased micro-LEDs consisting of 9 micro-LEDs, the DC bias is around 26 V, and the maximum peak-to-peak voltage is in the order of 7 V [Xie *et al.*, 2019]. The linear region can also be found based on a datasheet. An example of linear regions obtained from a datasheet has been shown in Figure 2.10 in Ch. 2. Therefore based on the above arguments, an abstraction of the linear region of a $P - I$ curve, as shown in Figure 4.2, will be used throughout this section. That is, the range $[I_a, I_b]$ is referred to as a linear region of a light emitter. It is worth noting that the linear region is temperature dependent [Turan & Ucar, 2017]. Throughout this thesis, a cooling system, e.g., a heat sink, is assumed such that the linear region is fixed [Ghassemlooy *et al.*, 2018].

4.4.2 PAM-SCFDE with LE

A high-level description of PAM-SCFDE with LE will be first discussed before going into details in the next paragraph. Figure 4.3 depicts a PAM-SCFDE with a feed-forward LE, denoted

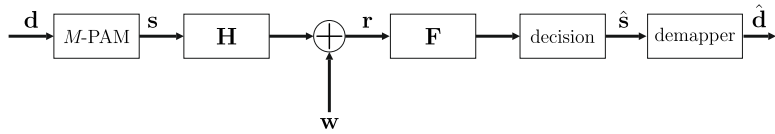


Figure 4.3. PAM-SCFDE with LE.

by a matrix \mathbf{F} . The input information vector coming from the finite alphabet is denoted by \mathbf{d} . Then, the input information vector \mathbf{d} is mapped into a symbol vector \mathbf{s} based on a mapping set \mathcal{P}_M . Elements of \mathcal{P}_M are PAM symbols representing a driving current of a light emitter. A channel matrix \mathbf{H} represents an equivalent channel model comprising analog front-ends of an optical transceiver system and a LiFi CIR. A thermal and shot noise at the receiver are modeled by a vector \mathbf{w} [Kahn & Barry, 1997]. Hence, the received symbol is denoted by $\mathbf{r} = \mathbf{H}\mathbf{s} + \mathbf{w}$. Then, a linear equalization is carried out by multiplying \mathbf{r} with a linear matrix \mathbf{F} . A decision process is performed to estimate the symbol vector \mathbf{s} , namely $\hat{\mathbf{s}}$. Lastly, a demapper is used to estimate the information vector \mathbf{d} , namely $\hat{\mathbf{d}}$.

A block transmission with an input sequence \mathbf{d} is assumed, where $\mathbf{d} = [d_0, d_1, \dots, d_{N-1}]^T \in \mathcal{D}^{N \times 1}$, $\mathcal{D} = \{0, 1, \dots, M - 1\}$, N is the block length, and M is the constellation size. This information data is then mapped into a symbol vector $\mathbf{s} \in \mathcal{P}_M^{N \times 1}$. Then, the mapping set \mathcal{P}_M is defined based on a light emitter's linear region $[I_a, I_b]$ as follows:

$$\mathcal{P}_M = \left\{ I_a + \frac{I_b - I_a}{M-1} i \middle| i \in \{0, 1 \cdots, M-1\}, [I_a, I_b] \subset \mathbb{R}^+ \right\}, \quad (4.1)$$

where $[I_a, I_b]$ is assumed to be strictly positive as discussed previously. For a unit energy transmit pulse, the energy per symbol is denoted as:

$$E_s = \frac{1}{|\mathcal{P}_M|} \sum_{s \in \mathcal{P}_M} |s|^2 = \frac{1}{6} \left(2(I_a^2 + I_a I_b + I_b^2) + \frac{(I_b - I_a)^2}{M-1} \right). \quad (4.2)$$

Energy per bit is denoted by $E_b = E_s / \log_2 M$. The mean of s is defined as:

$$\mu_s \triangleq \mathbb{E}[s] = \frac{I_a + I_b}{2}. \quad (4.3)$$

Figure 4.4 shows an equivalent channel matrix \mathbf{H} , which models:

- a CP addition block.

- a P/S conversion,
- a transmitter's frontend ($h_{\text{txfe}}(t)$) as described in Chapter 2,
- an LD ($h_{\text{ld}}(t)$),
- a LiFi CIR ($h_{\text{woc}}(t)$),
- a PD ($h_{\text{pd}}(t)$),
- a TIA ($h_{\text{tia}}(t)$),
- a receiver's frontend ($h_{\text{rffe}}(t)$) as described in Chapter 2,
- an S/P conversion, and
- a CP removal block.

The input of the channel matrix is denoted by the symbol vector \mathbf{s} . First, a CP is added to the symbol vector \mathbf{s} with the CP length L_{cp} , which is assumed to be $L_{\text{cp}} < N$. The CP addition operation is denoted by $\mathbf{T}\mathbf{s}$, where \mathbf{T} is defined as:

$$\mathbf{T}_{(N+L_{\text{cp}}) \times N} = \begin{bmatrix} \mathbf{0}_{L_{\text{cp}} \times (N-L_{\text{cp}})} & \mathbf{I}_{L_{\text{cp}}} \\ \mathbf{I}_{N-L_{\text{cp}}} & \mathbf{0}_{(N-L_{\text{cp}}) \times L_{\text{cp}}} \\ \mathbf{0}_{L_{\text{cp}} \times (N-L_{\text{cp}})} & \mathbf{I}_{L_{\text{cp}}} \end{bmatrix}. \quad (4.4)$$

Accordingly, a CP removal matrix at the receiver \mathbf{R} is defined as:

$$\mathbf{R}_{N \times (N+L_{\text{cp}})} = \begin{bmatrix} \mathbf{0}_{N \times L_{\text{cp}}} & \mathbf{I}_N \end{bmatrix}. \quad (4.5)$$

Prior to the digital-to-analog converter (DAC), the output of the CP addition is transformed into a discrete-time symbol sequence $x(n)$ by the P/S conversion.

A concatenation of the CIRs of a transmitter's frontend, LD, wireless optical channel (WOC), PD, TIA and a receiver's frontend is denoted by $c_c(t)$, which is defined as:

$$c_c(t) = h_{\text{txfe}}(t) \circledast h_{\text{ld}}(t) \circledast h_{\text{woc}}(t) \circledast h_{\text{pd}}(t) \circledast h_{\text{tia}}(t) \circledast h_{\text{rffe}}(t). \quad (4.6)$$

The models of the transceiver's frontends, LD, WOC, PD, TIA follow the model that is discussed in Chapter 2. Additionally, a discrete-time model comprising an FIR filter $C(z)$ and an additive white noise $w(n)$ with a zero mean and a variance of $\sigma_w^2 = R_s N_0 / 2$ is used in this thesis, where $N_0/2$ is the double-sided power spectral density of the thermal noise. The FIR

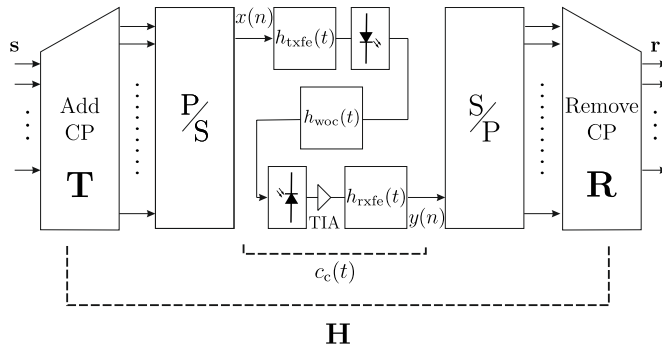


Figure 4.4. The block diagram of the channel matrix \mathbf{H} , which models: a CP addition block, a P/S conversion, a CIR of a transmitter's frontend $h_{txfe}(t)$, an LD ($h_{ld}(t)$), a LiFi CIR ($h_{woc}(t)$), a PD ($h_{pd}(t)$), a TIA ($h_{tia}(t)$), a CIR of a receivers's frontend ($h_{rxfe}(t)$), an S/P conversion, and a CP removal block.

filter $C(z)$ is defined as:

$$C(z) = \sum_{n=0}^{L_{cp}} c(n)z^{-n}, \quad (4.7)$$

where $c(n) \triangleq c_e(nT_s)$ and $T_s = 1/R_s$.

The concatenation of the matrix T , P/S, the channel $C(z)$, S/P and the matrix R can be represented by an $N \times N$ circulant matrix \mathbf{H} whose first column vector is:

$$[c(0), c(1), \dots, c(L_{cp}), \mathbf{0}_{1 \times (N-L_{cp}-1)}]^T,$$

where $N > L_{cp}$. A circulant matrix is diagonalizable by a normalized discrete Fourier transform (DFT) matrix denoted by \mathbf{W} , i.e.,:

$$\mathbf{H} = \mathbf{W}^H \boldsymbol{\Gamma} \mathbf{W}, \quad (4.8)$$

where $\boldsymbol{\Gamma}$ is a $N \times N$ diagonal matrix whose diagonal entry is the N -point DFT of the channel tap $c(n)$.

The received symbol vector \mathbf{r} can be written as:

$$\mathbf{r} = \mathbf{H}\mathbf{s} + \mathbf{w}. \quad (4.9)$$

Then, the received symbol vector \mathbf{r} is equalized by a feedforward filter \mathbf{F} under a linear opera-

tion \mathbf{Fr} . The estimated symbol vector of \mathbf{s} is defined as:

$$\hat{\mathbf{s}} = \arg \min_{\mathbf{s} \in \mathcal{P}_M^N} \|\mathbf{Fr} - \mathbf{s}\|.$$

The error vector is defined as $\mathbf{e} = \hat{\mathbf{s}} - \mathbf{s} = \mathbf{FHs} + \mathbf{Fw} - \mathbf{s} = (\mathbf{FH} - \mathbf{I})\mathbf{s} + \mathbf{Fw}$. Then, an MSE matrix is defined as:

$$\mathbf{R}_e \triangleq \mathbb{E} [\mathbf{ee}^H] = \mathbf{FHR}_s \mathbf{H}^H \mathbf{F}^H + \mathbf{R}_s - \mathbf{FHR}_s - \mathbf{R}_s \mathbf{H}^H \mathbf{F}^H + \sigma_w^2 \mathbf{FF}^H, \quad (4.10)$$

where $\mathbf{R}_s \triangleq \mathbb{E} [\mathbf{ss}^H] = E_s \mathbf{I} + \mu_s^2 \tilde{\mathbf{I}}$, and $\tilde{\mathbf{I}}$ is a matrix whose elements are all one except at all main diagonal entries, which are zero.

4.4.3 PAM-SCFDE with LE and DFE

Figure 4.5 shows the PAM-SCFDE with a DFE at the receiver. For a DFE system, a feedback loop is added after the linear equalization. The loop consists of a feedback matrix \mathbf{B} and a decision block to limit the output value of the feedback filter. The vector symbol \mathbf{Fr} is further processed by a feedback loop consisting of a feedback matrix \mathbf{B} . To impose a strict causality on the feedback filter, the matrix \mathbf{B} is assumed to be a strictly lower triangular matrix. That is, to estimate the n^{th} symbol, only the current input symbol and the *previously* estimated symbols are used. Note that the decision block is included in the feedback loop to limit the value and maintain the stability (bounded-input, bounded-output stability) of the filter.

Let $\bar{\mathbf{B}} = \mathbf{I} + \mathbf{B}$. The *ideal* error vector for the DFE system is $\mathbf{e} = (\mathbf{FH} - \bar{\mathbf{B}})\mathbf{s} + \mathbf{Fw}$, where it is assumed where no error propagation is assumed, i.e., $\mathbf{B}\hat{\mathbf{s}}$ at the receiver is replaced by \mathbf{Bs} . Then, the MSE matrix can be readily verified as:

$$\mathbf{R}_e = \mathbf{FHR}_s \mathbf{H}^H \mathbf{F}^H + \bar{\mathbf{B}} \mathbf{R}_s \bar{\mathbf{B}}^H - \mathbf{FHR}_s \bar{\mathbf{B}}^H - \bar{\mathbf{B}} \mathbf{R}_s \mathbf{H}^H \mathbf{F}^H + \sigma_w^2 \mathbf{FF}^H. \quad (4.11)$$

This MSE matrix will be used to find the optimal filter \mathbf{B} .

4.4.4 PAM-SCFDE with LE and THP

Figure 4.6 shows the PAM-SCFDE with a THP at the transmitter. In addition to a feedback matrix \mathbf{B} at the transmitter, a THP also has a modulo operation, which is used to limit the value

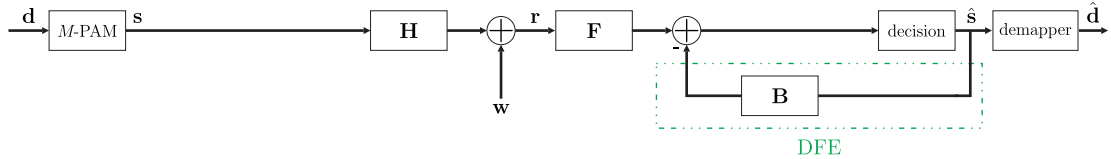


Figure 4.5. PAM-SCFDE with LE and DFE.

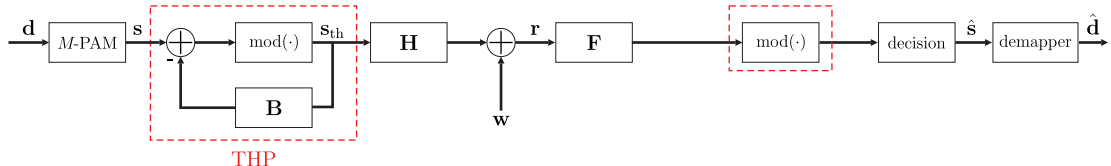


Figure 4.6. PAM-SCFDE with LE and THP.

of the output symbol of the THP. The output of THP is denoted by s_{th} . To fit the value of s_{th} into a linear dynamic range of a light emitter, the modulo operation is defined as:

$$\text{mod}(x) \triangleq x - (I_b - I_a) \left\lfloor \frac{x - I_a}{(I_b - I_a)} \right\rfloor. \quad (4.12)$$

The input-output relationship of the modulo operation is shown in Figure 4.7. The black and white circles in Figure 4.7 emphasize the half-open interval of the modulation operation, which can be written as:

$$\mathcal{I}_{th} \triangleq [I_a, I_b). \quad (4.13)$$

The exclusion of I_b in (4.13) implies that an ambiguity can occur if the mapping set \mathcal{P}_M in (4.1) is used. The reason for this is that the output of the symbol I_b is I_a , which cannot be correctly recovered at the receiver.

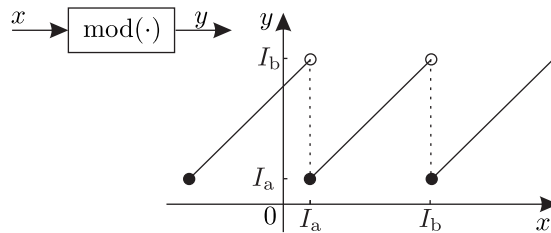


Figure 4.7. The modulo operation for the THP system.

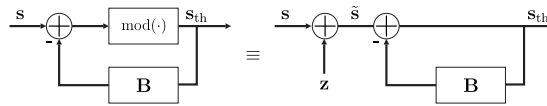


Figure 4.8. An equivalent model for THP.

In order to avoid the ambiguity caused by the half-open interval \mathcal{I}_{th} , let's define an interval for s as:

$$\mathcal{I}_s = [I_a + \epsilon, I_b - \epsilon], \quad 0 < \epsilon < \frac{I_b - I_a}{2}. \quad (4.14)$$

The variable ϵ denotes the width reduction of the linear region of an LED that the symbol s occupies. The mapping set for a THP is now defined as:

$$\mathcal{P}_M^{\text{THP}} = \left\{ I_a + \epsilon + \frac{I_b - I_a - 2\epsilon}{M-1} i \middle| i \in \{0, 1, \dots, M-1\} \right\}.$$

The energy per symbol can be written as:

$$E_s^{\text{THP}} = \frac{1}{|\mathcal{P}_M^{\text{THP}}|} \sum_{s \in \mathcal{P}_M^{\text{THP}}} |s|^2 = \frac{1}{6} \left(2(I_a^2 + I_a(I_b + \epsilon) + I_b^2 - I_b\epsilon + \epsilon^2) + \frac{(I_a - I_b + 2\epsilon)^2}{M-1} \right).$$

It is widely known that the output vector symbol, s_{th} , is identically independently distributed (IID). In addition, it follows a continuous uniform distribution [Fischer, 2002, p. 132]. Let E_{sth} be the energy per symbol after THP, which is given as:

$$E_{\text{sth}} = \frac{(I_b - I_a)^2}{12} + \frac{(I_b + I_a)^2}{4}. \quad (4.15)$$

Using (4.2) and (4.15), the precoding ratio is defined as [Fischer, 2002, p. 143]:

$$\gamma_{\text{th}} \triangleq \frac{E_{\text{sth}}}{E_s} = \frac{2(I_a^2 + I_a I_b + I_b^2)}{2(I_a^2 + I_a(I_b + \epsilon) + I_b^2 - I_b\epsilon + \epsilon^2) + \frac{(I_a - I_b + 2\epsilon)^2}{M-1}}. \quad (4.16)$$

It is easier to calculate the error vector using the equivalent model of THP as depicted in Figure 4.8, where the symbol vector \tilde{s} is referred to as the effective symbol vector [Fischer, 2002, p. 127]. A *unique precoding vector* $\mathbf{z} \in \mathbb{Z}^{N \times 1}$ is added to s such that $s_{\text{th}} \in \mathcal{I}_{\text{th}}^{N \times 1}$ based on operation in (4.12). Therefore, we have $s_{\text{th}} = \bar{\mathbf{B}}^{-1} \tilde{s}$.

It is generally considered difficult to directly work on the pair of vector symbols \mathbf{s} and $\hat{\mathbf{s}}$ to find the optimal filters. Instead, we can use the vector symbols $\tilde{\mathbf{s}}$ and its estimation, which is denoted by $\hat{\tilde{\mathbf{s}}}$. Hence, the error vector \mathbf{e} can be approximated by:

$$\mathbf{e} \approx \hat{\tilde{\mathbf{s}}} - \tilde{\mathbf{s}} = \mathbf{F}\mathbf{H}\hat{\mathbf{B}}^{-1}\tilde{\mathbf{s}} + \mathbf{F}\mathbf{w} - \tilde{\mathbf{s}} = (\mathbf{F}\mathbf{H} - \hat{\mathbf{B}})\mathbf{s}_{\text{th}} + \mathbf{F}\mathbf{w}. \quad (4.17)$$

This is equivalent to the case where the precoding vector \mathbf{z} is perfectly known at the receiver. Then, the MSE matrix is defined as:

$$\mathbf{R}_e = \mathbf{F}\mathbf{H}\mathbf{R}_{\mathbf{s}_{\text{th}}}\mathbf{H}^H\mathbf{F}^H + \mathbf{R}_{\mathbf{s}_{\text{th}}} - \mathbf{F}\mathbf{H}\mathbf{R}_{\mathbf{s}_{\text{th}}} - \mathbf{R}_{\mathbf{s}_{\text{th}}}\mathbf{H}^H\mathbf{F}^H + \sigma_w^2\mathbf{F}\mathbf{F}^H, \quad (4.18)$$

where $\mathbf{R}_{\mathbf{s}_{\text{th}}} \triangleq \mathbb{E}[\mathbf{s}_{\text{th}}\mathbf{s}_{\text{th}}^H]$. As in the DFE case, this MSE matrix will be used to determine the optimal filters.

4.4.5 MMSE-Based Equalizers

In this subsection, a joint optimal design for matrices \mathbf{F} and \mathbf{B} is discussed first, and it is followed by its optimality discussion.

4.4.5.1 Joint Design

Based on (4.10), (4.11), and (4.18), the MSE matrices \mathbf{R}_e for LE, DFE and THP systems have similar forms. Therefore, a general design problem based on MMSE can be formulated, i.e., minimize $\mathbb{E}[e_i e_i^H]$, $\forall i$. Equivalently, it is the same as minimizing $\text{tr}(\mathbf{R}_e)$. Therefore, a complete design problem can be stated as:

$$\begin{aligned} \arg \min_{\mathbf{F}, \mathbf{B}} & \quad \text{tr}(\mathbf{R}_e) \\ \text{subject to} & \quad \mathbf{B} \text{ is a strict lower triangular matrix. } \end{aligned} \quad (4.19)$$

Note that both the peak and average transmitter power are already constrained by the linear region of a light emitter, i.e., $[I_a, I_b]$; hence, it is not included in (4.19). The optimization problem in (4.19) is known to be a nonlinear problem [Xu *et al.*, 2006].

A typical approach to solve (4.19) is:

- (i) by treating \mathbf{B} as fixed and finding the optimal \mathbf{F} since there is no constraint imposed for \mathbf{F} , and
- (ii) the matrix \mathbf{B} is determined by using the expression for the optimal \mathbf{F} and the constraint on \mathbf{B} .

To derive an optimal \mathbf{F} , the orthogonality principle is used, i.e., $\mathbb{E} [\mathbf{e}\mathbf{r}^H] = 0$. For this purpose, it is easier to have the expression of \mathbf{e} as $\mathbf{e} = \mathbf{Fr} - \bar{\mathbf{B}}\mathbf{s}$. The optimal feedforward matrix \mathbf{F} is then:

$$\begin{aligned}\mathbf{F} &= \bar{\mathbf{B}}\mathbf{R}_{sr}\mathbf{R}_r^{-1} = \bar{\mathbf{B}}\mathbf{R}_s\mathbf{H}^H (\mathbf{H}\mathbf{R}_s\mathbf{H}^H + \mathbf{R}_w)^{-1} \\ &= \bar{\mathbf{B}}\mathbf{W}^H (\boldsymbol{\Gamma}^H \boldsymbol{\Gamma} + \sigma_w^2 \boldsymbol{\Gamma}_s^{-1})^{-1} \boldsymbol{\Gamma}^H \mathbf{W} = \bar{\mathbf{B}}\mathbf{W}^H \boldsymbol{\Lambda} \mathbf{W},\end{aligned}\quad (4.20)$$

where $\mathbf{R}_{sr} \triangleq \mathbb{E} [\mathbf{s}\mathbf{r}^H]$, $\mathbf{R}_r \triangleq \mathbb{E} [\mathbf{r}\mathbf{r}^H]$, $\mathbf{R}_w \triangleq \mathbb{E} [\mathbf{w}\mathbf{w}^H] = \sigma_w^2 \mathbf{I}$ and $\boldsymbol{\Gamma}_s = \mathbf{W}\mathbf{R}_s\mathbf{W}^H$ as \mathbf{R}_s is a circulant matrix. Using the properties of the DFT matrix \mathbf{W} , the $N \times N$ $\boldsymbol{\Gamma}_s$ matrix can also be defined as:

$$\boldsymbol{\Gamma}_s = \text{diag} (E_s + (N-1)\mu_s^2, E_s - \mu_s^2, \dots, E_s - \mu_s^2). \quad (4.21)$$

The matrix $\mathbf{W}^H \boldsymbol{\Lambda} \mathbf{W}$ in (4.20) is referred to as the frequency-domain equalization (FDE) since the received symbol vector \mathbf{r} is first transformed to the frequency domain by the DFT matrix \mathbf{W} and then multiplied by $\boldsymbol{\Lambda}$. Furthermore, since $\boldsymbol{\Lambda}$ is a diagonal matrix, it is commonly referred to as a single-tap FDE.

It is straightforward to see that if the channel tap is not zero, then $\boldsymbol{\Lambda}$ is not singular; hence, the feedforward matrix \mathbf{F} in (4.20) always exists. Using (4.20), the error vector can be written as:

$$\mathbf{e} = \bar{\mathbf{B}}\mathbf{R}_{sr}\mathbf{R}_r^{-1}\mathbf{r} - \bar{\mathbf{B}}\mathbf{s}.$$

The MSE matrix with the optimal \mathbf{F} is:

$$\begin{aligned}\mathbf{R}_e &= \bar{\mathbf{B}} (\mathbf{R}_s - \mathbf{R}_{sr}\mathbf{R}_r^{-1}\mathbf{R}_{rs}) \bar{\mathbf{B}}^H \\ &= \bar{\mathbf{B}} (\mathbf{R}_s - \mathbf{R}_s\mathbf{H}^H (\mathbf{H}\mathbf{R}_s\mathbf{H}^H + \mathbf{R}_w)^{-1} \mathbf{H}\mathbf{R}_s) \bar{\mathbf{B}}^H \\ &\stackrel{(a)}{=} \bar{\mathbf{B}} (\mathbf{R}_s^{-1} + \mathbf{H}^H \mathbf{R}_w^{-1} \mathbf{H})^{-1} \bar{\mathbf{B}}^H = \bar{\mathbf{B}} \mathbf{C} \bar{\mathbf{B}}^H,\end{aligned}\quad (4.22)$$

	F	B	R_e
LE	$\mathbf{W}^H \boldsymbol{\Lambda} \mathbf{W}$	$\mathbf{0}$	$\mathbf{W}^H (\boldsymbol{\Gamma}_s^{-1} + \sigma_w^{-2} \boldsymbol{\Gamma}^H \boldsymbol{\Gamma})^{-1} \mathbf{W}$
DFE & THP	$\bar{\mathbf{B}} \mathbf{W}^H \boldsymbol{\Lambda} \mathbf{W}$	$\mathbf{L}^{-1} - \mathbf{I}$	\mathbf{D}

Table 4.1. Optimal filters for PAM-SCFDE with LE, DFE, and THP.

where (a) uses the Woodbury matrix identity. Note that in order to have an optimal symbol detection within a block, it is necessary to obtain $\mathbf{R}_e = \boldsymbol{\Sigma}$, where $\boldsymbol{\Sigma}$ is a diagonal matrix with positive entries. In other words, the input of the decision block is white, i.e., the remaining error at each symbol is uncorrelated with the remaining error at the other symbols within the same block. That is, if $\mathbf{R}_e = \boldsymbol{\Sigma}$, then it is optimal in the sense of symbol-by-symbol detection [Palomar *et al.*, 2003].

Since \mathbf{C} is non-singular and positive definite, there exists a *unique* lower triangular matrix \mathbf{L} with a unit diagonal entry, and it is obtained by using the Cholesky decomposition, i.e.,:

$$\mathbf{C} = \mathbf{L} \mathbf{D} \mathbf{L}^H, \quad (4.23)$$

where \mathbf{D} is a diagonal matrix. Hence, from (4.22) and assigning $\mathbf{R}_e = \boldsymbol{\Sigma}$, we have the following relationship $\mathbf{L} \mathbf{D} \mathbf{L}^H = \bar{\mathbf{B}}^{-1} \boldsymbol{\Sigma} (\bar{\mathbf{B}}^H)^{-1}$. For $\mathbf{B} \neq \mathbf{0}$ (DFE and THP systems), the optimal feedback matrix and the minimum MSE can now be determined as:

$$\mathbf{B} = \mathbf{L}^{-1} - \mathbf{I}, \text{ and } \mathbf{R}_e = \mathbf{D}, \quad (4.24)$$

respectively. Table. 4.1 provides a summary of the optimal filters and the minimum MSE matrices.

4.4.5.2 Optimality Discussion

For an LE system, the MSE matrix is circulant; hence, the error variance at each symbol is identical, i.e., $\mathbb{E}[|e_i|^2] = [\mathbf{R}_e]_i = c, \forall i, c \in \mathbb{R}^+$. However, \mathbf{R}_e is not necessarily diagonal. The correlation implies that the error detection at any symbol correlates to the error detection at other symbols within a block. Therefore, the LE system is only optimal based on the MMSE criterion. We also observe that as $\text{tr}(\mathbf{R}_e^{\text{LE}}) = \text{tr}(\mathbf{C}) > \text{tr}(\mathbf{R}_e^{\text{DFE}}) = \text{tr}(\mathbf{D})$ which implies that the SINR of the LE system is upper bounded by that of the DFE system under the ideal assumptions. Consequently, the average bit error ratio (BER) of the LE system is always higher

than that of the ideal DFE system. For the THP system, the error performance of THP is not generally better than an LE system, and it highly depends on the value of ϵ , which has been shown in [Purwita, Chen, *et al.*, 2019]. In addition, we want to emphasize that even though $\mu_s \neq 0$, \mathbf{R}_s is still sometimes defined as $\mathbf{R}_s = E_s \mathbf{I}$, such as in [Nuwanpriya *et al.*, 2015]. It is straightforward to see that in this case $\text{tr}(\mathbf{R}_e)$ is higher; thus, it is suboptimal.

As the minimized MSE matrix is a diagonal matrix for the DFE and the THP systems, we know that the matrices in (4.20) and (4.24) are optimal in the sense of symbol-by-symbol detection within a block; equivalently, they maximize the SINR at each symbol. It can also be shown that (4.20) and (4.24) achieve an error bound based on Weyl's inequality [Weyl, 1949]. That is, if we can write the MSE matrix as $\text{tr}(\mathbf{R}_e) = \text{tr}(\bar{\mathbf{B}}\bar{\mathbf{L}}\bar{\mathbf{L}}^H\bar{\mathbf{B}}^H) = \|\bar{\mathbf{B}}\bar{\mathbf{L}}\|_F^2 = \sum_i \sigma_i^2$, where $\bar{\mathbf{L}} = \mathbf{LD}^{1/2}$, and σ_i is the singular value of $\bar{\mathbf{B}}\bar{\mathbf{L}}$, then we have:

$$\text{tr}(\mathbf{R}_e) = \sum_{i=1}^N \sigma_i^2 \geq \sum_{i=1}^N \mu_i^2 = \sum_{i=1}^N [\bar{\mathbf{B}}\bar{\mathbf{L}}]_i^2, \quad (4.25)$$

where μ_i is the eigenvalue of $\bar{\mathbf{B}}\bar{\mathbf{L}}$, and the last equality uses the fact that $\bar{\mathbf{B}}\bar{\mathbf{L}}$ is a lower triangular matrix, see [Weyl, 1949, (2)]. The equality in (4.25) is obtained when $\bar{\mathbf{B}}\bar{\mathbf{L}}$ is a normal matrix. $\bar{\mathbf{B}}\bar{\mathbf{L}}$ is normal, if and only if, it is a diagonal matrix. Using (4.24), we know that $\bar{\mathbf{B}}\bar{\mathbf{L}} = \mathbf{D}^{1/2}$, which is diagonal.

To show the limitation of the current optimal filters, it is also important to investigate the optimality in terms of minimizing the average BER. Based on [Palomar *et al.*, 2003], for a moderate to high SNR region, BER is minimized if eigenvalues of \mathbf{R}_e are identical, i.e., $\mathbf{R}_e = \alpha \mathbf{I}$ for a positive constant α as \mathbf{R}_e is a Hermitian matrix. However, the matrix \mathbf{D} does not necessarily have identical entries. Given that \mathbf{LDL}^H is unique, it is straightforward to see that the optimum average BER is not always achieved. Another way to see this is by using the trace-determinant inequality, which can be expressed as:

$$\text{tr}(\mathbf{R}_e) = \sum_{i=1}^N [\mathbf{D}]_i \geq N (\det(\bar{\mathbf{B}}\bar{\mathbf{C}}\bar{\mathbf{B}}^H))^{1/N} = N \left(\prod_{i=1}^N [\mathbf{D}]_i \right)^{1/N}. \quad (4.26)$$

The equation in (4.26) achieves the equality if \mathbf{D} has identical elements. The identical elements of \mathbf{D} can only be achieved if the CIR $c(n)$ is a constant. This occurs when all the front-end devices in Figure 4.4 are simply constant amplifiers with a flat gain, and the $h_{\text{woc}}(t)$ is a constant, i.e., there is no reflecting signal. This occurs when the bit rate is sufficiently low,

such that the inter-symbol interference (ISI) can be ignored, i.e., when $c(n)$ only has a single tap. One way to achieve the BER optimality is by adding a linear precoder, e.g., \mathbf{P} , before the matrix \mathbf{H} , i.e., \mathbf{H} is replaced by \mathbf{HP} .

To summarize this subsection, the optimal feed-forward matrix only achieves the minimum MSE, where the error detection in any symbol is correlated with other symbols. The DFE and THP systems are not only optimal in the sense of MSE, but also optimal in the sense of symbol-by-symbol detection as the error vectors at different symbols are uncorrelated. In other words, the DFE and THP systems also maximize individual SINR at each symbol.

4.5 SC-GTIM: PAM-SCFDE with IM

This section begins by outlining the motivations to apply the IM to PAM-SCFDE. Then, details of SC-GTIM are presented next in order to answer how PAM-SCFDE can benefit from IM. A set partitioning algorithm is discussed to construct a codebook for SC-GTIM in the end.

4.5.1 Motivations

IM is inspired by spatial modulation (SM) [R. Mesleh *et al.*, 2006; R. Y. Mesleh *et al.*, 2008], which simultaneously encodes both constellation symbols and transmit antenna index. The term IM is first introduced in [Abu-alhiga & Haas, 2009]. Instead of the transmit antenna index, subcarriers are used in [Abu-alhiga & Haas, 2009]. This method is referred to as subcarrier-IM OFDM. These transmit entities, namely transmit index (space domain) and subcarrier index (frequency domain), can be extended to other domains such as the time-domain [Nakao *et al.*, 2017; Choi, 2017] or combinations of these [Popoola *et al.*, 2013; Haas & Abu-Alhiga, 2016]. In fact, IM is not only limited to these domains, and could, for example, include orbital angular momentum (OAM) [Basar, 2018]. This section focuses on the adoption of TIM [Nakao *et al.*, 2017; Choi, 2017] to PAM-SCFDE. Recent survey papers in [Basar *et al.*, 2017; Sugiura *et al.*, 2017; Ishikawa *et al.*, 2018] summarize that IM appears to be a potential candidate for future wireless communication systems due to its spectral and energy efficiency as well as lower hardware complexity. These advantages can also be adopted in LiFi.

As IM can modulate an off-state transmit index, such as an antenna index in SM, it can be done with PAM-SCFDE having a strictly positive linear region. That is, the zero amplitude,

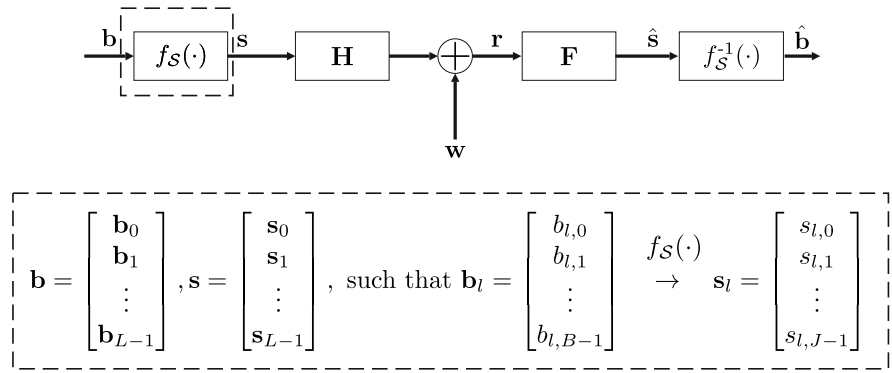


Figure 4.9. The system model of SC-GTIM.

for example, $I = 0$ in Figure 4.2, can be used as the off-state. Then, while the off-state is transmitted, PAM-SCFDE can benefit from a lower average transmit power. Also, having an additional choice of constellation symbols means that PAM-SCFDE might benefit from a larger Euclidean distance. These advantages will be demonstrated next.

4.5.2 Transmission Model

Figure 4.9 shows the block diagram of SC-GTIM, which is slightly modified from that of PAM-SCFDE, whose block diagram is shown in Figure 4.3. Instead of the input sequence d , B_t -bit binary vector b is used. A one-to-one mapping $f_{\mathcal{S}}$ converts the binary vector b to a symbol vector s according to a codebook \mathcal{S} . In this section, there are three codebooks that are considered, i.e.,:

- \mathcal{S}^{PAM} for the original PAM-SCFDE, which will be referred to as SC-PAM,
- \mathcal{S}^{TIM} for a direct adoption of TIM to PAM-SCFDE, which will be referred to as SC-TIM, and
- $\mathcal{S}^{\text{GTIM}}$ for a generalized version of \mathcal{S}^{TIM} , which will be referred to as SC-GTIM.

Therefore, \mathcal{S} is an element of $\{\mathcal{S}^{\text{PAM}}, \mathcal{S}^{\text{TIM}}, \mathcal{S}^{\text{GTIM}}\}$, i.e., $\mathcal{S} \in \{\mathcal{S}^{\text{PAM}}, \mathcal{S}^{\text{TIM}}, \mathcal{S}^{\text{GTIM}}\}$. At the receiver, an inverse mapping is used to estimate the binary vector b , i.e., \hat{b} .

The following is the mapping procedure of a binary vector b . Let J be a time-slot length. The B_t -bit binary vector b is partitioned into L sub-blocks, i.e., $b = [b_0^T, b_1^T, \dots, b_{L-1}^T]^T$, such that $J = N/L$. The length of each vector b_l becomes, $B = B_t/L$ bits. Then, each b_l is mapped onto a J -length symbol vector $s_l = [s_{l,0}, s_{l,1}, \dots, s_{l,J-1}]^T$ by a one-to-one mapping function

f_S . Therefore, the symbol vector can be defined as $\mathbf{s} = [\mathbf{s}_0^T, \mathbf{s}_1^T, \dots, \mathbf{s}_{L-1}^T]^T$, whose length is N symbols.

4.5.2.1 SC-PAM

For a block transmission with SC-PAM, the transmitted symbol vectors are chosen from the set \mathcal{S}^{PAM} which is defined as:

$$\mathcal{S}^{\text{PAM}} = \left\{ \mathbf{s}_l = [s_{l,0}, s_{l,1}, \dots, s_{l,J-1}]^T \mid s_{l,j} \in \mathcal{P}_M \right\},$$

where $|\mathcal{S}^{\text{PAM}}| = 2^B$ is the cardinality of the set \mathcal{S}^{PAM} . Typically, SC-PAM is defined with $J = 1$ and $s_l \in \mathcal{P}_M$ for $l = \{0, 1, 2, \dots, L-1 = N-1\}$. For example, with $M = 2$ and $B = 1$, if $b_{l,0} = 0$, then $s_{l,0}$ is mapped to $s_{l,0} = I_a$. Otherwise, $s_{l,0}$ is mapped to $s_{l,0} = I_b$. Equivalently with $J = 2$, the set \mathcal{S}^{PAM} can also be expressed as:

$$\mathcal{S}^{\text{PAM}} = \left\{ \begin{bmatrix} I_a \\ I_a \end{bmatrix}, \begin{bmatrix} I_b \\ I_a \end{bmatrix}, \begin{bmatrix} I_a \\ I_b \end{bmatrix}, \begin{bmatrix} I_b \\ I_b \end{bmatrix} \right\} \begin{array}{c} b_{l,0}=[0] & b_{l,0}=[1] & b_{l,0}=[0] & b_{l,0}=[1] \\ b_{l,1}=[0] & b_{l,1}=[0] & b_{l,1}=[1] & b_{l,1}=[1] \end{array}. \quad (4.27)$$

Notice that the mapping remains the same as in the case when $J = 1$. This representation will be used to relate SC-PAM to SC-TIM and SC-GTIM. For SC-PAM, the Gray code is always used to ensure the optimality in the sense of error probability [Agrell *et al.*, 2004].

4.5.2.2 SC-TIM

In SC-TIM, the B -bit vector \mathbf{b}_l contains a B_1 -bit and a B_2 -bit binary vectors, i.e., $B = B_1 + B_2$. A B_1 -bit binary vector is used to modulate the index of the active time slots. Note that B_1 is defined such that K out of J are chosen from the set \mathcal{P}_M , and the others are set to be 0. It is also worth noting that K out of J can be interpreted as choosing K out of J *time slots* to be active. A B_2 -bit binary vector is used to modulate the M -PAM symbols from \mathcal{P}_M . Therefore, B_1 and B_2 can be calculated as:

$$B_1 = \left\lfloor \log_2 \binom{J}{K} \right\rfloor, \text{ and } B_2 = K \log_2 M. \quad (4.28)$$

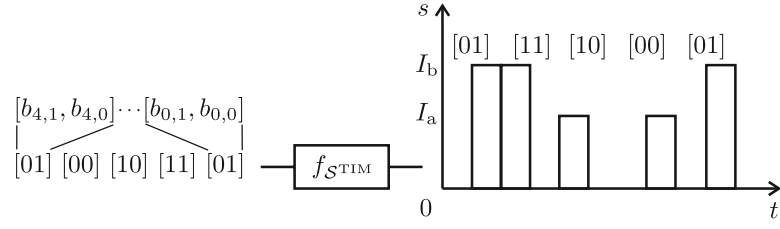


Figure 4.10. The working principle of $f_{S^{TIM}}$ with (4.29).

For example, with $K = 1$, $J = 2$ and $\mathcal{P}_2 = \{I_a, I_b\}$, we have the possible transmitted symbol $s_l \in \mathcal{S}^{TIM}$, such that the mapping set \mathcal{S}^{TIM} is:

$$\mathcal{S}^{TIM} = \left\{ \begin{bmatrix} 0 \\ I_a \end{bmatrix}, \begin{bmatrix} 0 \\ I_b \end{bmatrix}, \begin{bmatrix} I_a \\ 0 \end{bmatrix}, \begin{bmatrix} I_b \\ 0 \end{bmatrix} \right\} \text{ (4.29)}$$

$$\begin{array}{ll} b_{l,0}=[0] & b_{l,0}=[1] \\ b_{l,1}=[0] & b_{l,1}=[0] \end{array} \quad \begin{array}{ll} b_{l,0}=[1] & b_{l,0}=[0] \\ b_{l,1}=[1] & b_{l,1}=[1] \end{array}$$

In this case, $b_{l,1} = 0$ denotes the first time slot as inactive, while $b_{l,1} = 1$ denotes the second time slot as inactive. In addition, $b_{l,0} = 0$ denotes that the PAM constellation symbol I_a is chosen. Otherwise, the PAM constellation symbol I_b is chosen. A working principle of (4.29) is shown in Figure 4.10. Suppose the binary input vector is $\mathbf{b} = [1, 0, 1, 1, 0, 1, 0, 0, 1, 0]^T$ and $L = 5$, then we have $\mathbf{b}_0 = [b_{0,0}, b_{0,1}]^T = [1, 0]^T$, $\mathbf{b}_1 = [b_{1,0}, b_{1,1}]^T = [1, 1]^T$, etc. Based on (4.29), $[1, 0]^T$ maps to $[0, I_b]^T$, and $[1, 1]^T$ maps to $[I_b, 0]^T$ consecutively.

Compared to the energy per symbol of the SC-PAM in (4.2), it is generally harder to obtain a compact expression for \mathbf{R}_s . A naive way is (i) to list all possible combinations of alphabets $\mathbf{s}\mathbf{s}^H$; (ii) count the frequency of each element of the alphabet for given parameters M , K and J ; and (iii) calculate $\mathbf{R}_s = \mathbb{E} [\mathbf{s}\mathbf{s}^H]$ by taking the expectation value of all possible combinations. However, for $K = 1$, $\mathbf{R}_s^{TIM, K=1}$ can be found as shown in (4.30). The constants p and q can be calculated as:

$$p = \frac{1}{2^B} \sum_{s \in \mathcal{P}_M} |s|^2 = \frac{\left((I_a^2 + I_b^2)(2M - 1) + 2I_a I_b(M - 2) \right)}{3 \left(1 - \frac{1}{M} \right) 2^{(B+1)}},$$

$$q = \frac{1}{2^J 2^M} \sum_{x \in \mathcal{P}_M} \sum_{y \in \mathcal{P}_M} xy = M^2 (I_a + I_b)^2 2^{-(J+M+2)},$$

where the sum of the series formula is used to obtain these expressions. Note that $\mathbf{R}_s^{TIM, K=1}$ is not a circulant matrix. This is an example of a scenario when the simple single-tap equalization

cannot always be performed by a PAM-based SC-TIM. In this case, the PAM-based SC-TIM has a higher computational complexity. Note that p is also the average energy per symbol for the PAM-based SC-TIM which is lower than that without TIM, i.e., $E_{s,TIM} = p \leq E_{s,PAM}$.

$$\mathbf{R}_{\mathbf{s}}^{\text{TIM}, K=1} = \begin{bmatrix} \mathbf{P}_{J \times J} & \mathbf{Q}_{J \times J} & \cdots & \mathbf{Q}_{J \times J} \\ \mathbf{Q}_{J \times J} & \mathbf{P}_{J \times J} & \cdots & \mathbf{Q}_{J \times J} \\ \vdots & \vdots & \ddots & \vdots \\ \mathbf{Q}_{J \times J} & \mathbf{Q}_{J \times J} & \cdots & \mathbf{P}_{J \times J} \end{bmatrix}, \quad (4.30)$$

For an IM scheme, an average pairwise-error probability (PEP) over all possible pairs of symbols is typically used as an upper bound. The average BER is upper bounded by the average PEP (APEP), that is,:

$$P_b \leq \frac{1}{B2^B} \sum_{\mathbf{s}_i \in \mathcal{S}^{\text{TIM}}} \sum_{\substack{\mathbf{s}_j \in \mathcal{S}^{\text{TIM}} \\ \mathbf{s}_j \neq \mathbf{s}_i}} d_H(\mathbf{s}_i, \mathbf{s}_j) P(\mathbf{s}_i \rightarrow \mathbf{s}_j) = \text{APEP}. \quad (4.31)$$

A Hamming distance between the bits associated with both \mathbf{s}_i and \mathbf{s}_j is denoted by $d_H(\mathbf{s}_i, \mathbf{s}_j)$.

The PEP is defined as:

$$P(\mathbf{s}_i \rightarrow \mathbf{s}_j) = Q\left(\frac{d_E(\mathbf{s}_i, \mathbf{s}_j)}{2\sqrt{\sigma_e^2}}\right), \quad (4.32)$$

where $d_E(\mathbf{s}_i, \mathbf{s}_j) = \|\mathbf{s}_i - \mathbf{s}_j\|$ denotes the Euclidean distance between \mathbf{s}_i and \mathbf{s}_j . Let the average noise power of \mathbf{e} be σ_e^2 , which is defined as:

$$\sigma_e^2 \triangleq \text{tr}(\mathbf{R}_e)/N.$$

4.5.2.3 SC-GTIM

The main difference between SC-TIM and SC-GTIM is that K does not have to be fixed. To compare it with (4.29), we have, for example,:

$$\mathcal{S}^{\text{GTIM}} = \left\{ \begin{bmatrix} 0 \\ 0 \end{bmatrix}, \begin{bmatrix} I_b \\ 0 \end{bmatrix}, \begin{bmatrix} 0 \\ I_b \end{bmatrix}, \begin{bmatrix} I_b \\ I_b \end{bmatrix} \right\}, \quad (4.33)$$

$b_{l,0}=[0] \quad b_{l,0}=[1] \quad b_{l,0}=[0] \quad b_{l,0}=[1]$
 $b_{l,1}=[0] \quad b_{l,1}=[0] \quad b_{l,1}=[1] \quad b_{l,1}=[1]$

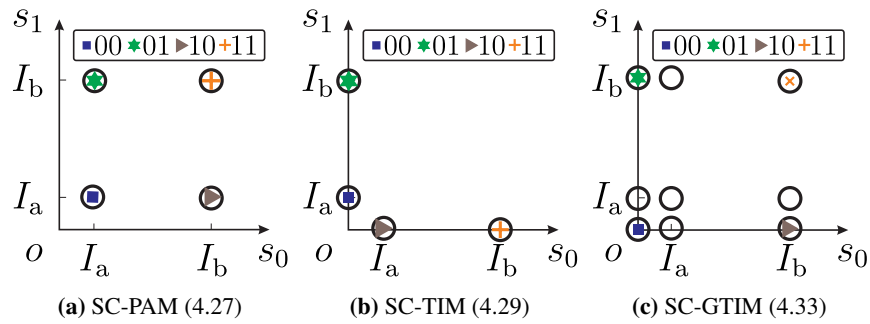


Figure 4.11. Vector representations: (a) SC-PAM with $M = 2$ and the Gray code and without IM ($\eta = 1$), (b) SC-TIM with $K = 1$ and $J = 2$ ($\eta = 1$) and (c) SC-GTIM with $J = 2$ ($\eta = 1$). The circle markers show the symbols that can be chosen and labeled with binary vectors. The other markers show the chosen symbols.

where the number of bits in SC-GTIM is defined as $B = \log_2 |\mathcal{S}^{\text{GTIM}}|$. Notice that K is not fixed for all elements of $\mathcal{S}^{\text{GTIM}}$ in the above example. In addition, SC-GTIM in (4.33) is reduced to OOK with return-to-zero pulse or PPM, which is known to achieve the Shannon capacity in low spectral efficiency regions [Verdu, 2002]. It is worth mentioning that SC-TIM cannot always be reduced to OOK as SC-TIM is constrained by (4.28), which is less flexible than SC-GTIM.

To illustrate the set $\mathcal{S}^{\text{GTIM}}$ based on (4.33) and compare it with other examples in (4.27) and (4.29), the vector representations of $[s_{l,0}, s_{l,1}, \dots, s_{l,J-1}]^T$ are illustrated in Figure 4.11. The index l is omitted as it is not relevant. Figure 4.11 uses circles to show all possible s_l that can be chosen and the colored markers to show the chosen s_l . In this way, we have a classic constellation diagram representation. Figure 4.11(c) clearly illustrates a more flexible constellation design of SC-GTIM compared to the others. If this can be cultivated fully, a significant performance gain can be achieved.

We now compare SC-GTIM with SC-TIM in (4.29). It is obvious to see that the BER of SC-TIM with \mathcal{S}^{TIM} expressed in (4.29) will be limited by the vectors $[0, I_a]^T$ and $[I_a, 0]^T$ if $|I_a - 0| < |I_b - I_a|$. Consequently, the BER of SC-TIM is worse than that of the conventional SC-PAM. In this case, a codebook with more possible constellation points is required. This is where SC-GTIM has the advantage by means of freeing the number of active time slots.

A collection of possible codewords \mathcal{S}^s is defined as:

$$\mathcal{S}^s = \left\{ \mathbf{s}_l = [s_{l,0}, s_{l,1}, \dots, s_{l,J-1}]^T \mid s_{l,j} \in \{\mathcal{P}_M, \{0\}\} \right\}. \quad (4.34)$$

The indexing and grouping of all possible $[s_{l,0}, s_{l,1}, \dots, s_{l,J-1}]^T \in \mathcal{S}^{\text{GTIM}} \subseteq \mathcal{S}^s$ will affect the

BER. There are:

$$G = \frac{(M+1)^J!}{((M+1)^J - 2^B)!} \quad (4.35)$$

ways of indexing and grouping in the construction of the set $\mathcal{S}^{\text{GTIM}}$. Based on (4.32) and the upper bound in (4.31), the design problem can be formulated as:

$$\begin{aligned} \arg \max_{\mathcal{S}^{\text{GTIM}}} \quad & C = \sum_{\mathbf{s}_i \in \mathcal{S}^{\text{GTIM}}} \sum_{\substack{\mathbf{s}_j \in \mathcal{S}^{\text{GTIM}} \\ \mathbf{s}_j \neq \mathbf{s}_i}} d_H(\mathbf{s}_i, \mathbf{s}_j) d_E(\mathbf{s}_i, \mathbf{s}_j) \quad (4.36) \\ \text{subject to:} \quad & |\mathcal{S}^{\text{GTIM}}| = 2^B. \end{aligned}$$

The problem (4.36) can be seen as the problem of choosing 2^B vectors of $[s_{l,0}, s_{l,1}, \dots, s_{l,J-1}]^T$ and labeling them with a B -bit vector. As (4.36) is a combinatoric problem which has G many possible combinations, a meta-heuristic solution for a permutation-based combinatorial optimization problem can be used. However, we will illustrate that a simpler way can be used by using the knowledge of the Gray encoding.

4.5.3 Construction of a Good Set $\mathcal{S}^{\text{GTIM}}$

In this subsection, the construction of a good set $\mathcal{S}^{\text{GTIM}}$ is provided. A simple example in two dimensions (2-D), i.e., $J = 2$, will be presented first, and this is followed by an introduction of several notations. Then, a more detailed algorithm having higher dimensions, i.e., $J > 2$ is given next.

4.5.3.1 Simple Example in 2-D ($J = 2$)

For a better enumeration and illustration, \mathcal{P}_M is redefined as:

$$\mathcal{P}_M = \{m_0, m_1, \dots, m_{M-1} \mid I_a = m_0 < m_1 < \dots < m_{M-1} = I_b\},$$

Now, assume that a uniform M -PAM constellation is used, i.e., $|m_i - m_j| = c, \forall i \neq j \in \{0, 1, \dots, M-1\}$ and a positive constant c . In this example, we use the following collection

of possible codewords:

$$\mathcal{S}^s = \left\{ \begin{bmatrix} 0 \\ 0 \end{bmatrix}, \begin{bmatrix} m_0 \\ 0 \end{bmatrix}, \begin{bmatrix} m_1 \\ 0 \end{bmatrix}, \begin{bmatrix} 0 \\ m_0 \end{bmatrix}, \begin{bmatrix} m_0 \\ m_0 \end{bmatrix}, \begin{bmatrix} m_1 \\ m_0 \end{bmatrix}, \begin{bmatrix} 0 \\ m_1 \end{bmatrix}, \begin{bmatrix} m_0 \\ m_1 \end{bmatrix}, \begin{bmatrix} m_1 \\ m_1 \end{bmatrix} \right\},$$

which represents the case where $M = 2$ and $J = 2$. Suppose that we define $B = 3$ bits, then we should pick $2^3 = 8$ of $|\mathcal{S}^s| = 9$. Now that we have defined \mathcal{S}^s , the design problem can be summarized as follows:

given: M, B, J

choose 2^B of $\mathbf{s}_l \in \mathcal{S}^s$ and label them with binary vector

such that the 2^B \mathbf{s}_l have as large C (see (4.36)) as possible.

The basic operation of the construction algorithm is the set partitioning algorithm denoted by SP. Simple illustrations of the heuristic steps taken in the SP operation are described below.

I) The first step:

Choose 2 sets of $\lfloor (M + 1)^J / 2 \rfloor = 4$ vectors of \mathbf{s}_l such that the Euclidean distance of the center of the mass of two sets are maximum. Then, label each set with a binary value and denote the sets with $\mathbb{P}_{b_0}^{M=2, \tilde{J}=2}$, where $b_0 \in \{0, 1\}$ and \tilde{J} is the number of elements of \mathbf{s}_l which are taken into account. In this case, all elements of \mathbf{s}_l are taken into account at once as $\tilde{J} = J$. The result is illustrated in Figure 4.12(a). The chosen symbol vectors are shown by squares, and the cross marker shows the unchosen symbol vector. It is worth noting here that the elements in the set $\mathbb{P}_{b_0}^{2,2}$ will be labeled as $[b_0 XX]$, where $X \in \{0, 1\}$ denotes a binary digit that is not assigned yet. That is, elements in $\mathbb{P}_1^{2,2}$ will be labeled as [100], [101], [110] or [111] in the final step.

II) The second step:

Partition each $\mathbb{P}_{b_0}^{2,2}$ as in the first step. The outputs are now denoted as $\mathbb{P}_{b_0, b_1}^{2,2}$, where b_0 is followed by $b_1 \in \{0, 1\}$ in the subscripts. Now, each set $\mathbb{P}_{b_0, b_1}^{2,2}$ contains two vectors. The binary mapping of $\mathbb{P}_{b_0, b_1}^{2,2}$ is carried out such that it forms the Gray mapping with its

neighbors. For example:

$$\mathbb{P}_{1,0}^{2,2} = \left\{ \begin{bmatrix} 0 \\ m_0 \end{bmatrix}, \begin{bmatrix} 0 \\ m_1 \end{bmatrix} \right\} \text{ and } \mathbb{P}_{1,1}^{2,2} = \left\{ \begin{bmatrix} m_0 \\ m_1 \end{bmatrix}, \begin{bmatrix} m_1 \\ m_1 \end{bmatrix} \right\}$$

are neighbors to each other, and [10] and [11] forms the Gray mapping. The complete mapping is shown in Figure 4.12(b).

III) The third step:

As only 1 remaining bit needs to be assigned, the final step is to make sure that each element and its neighbors form a Gray mapping. As depicted in Figure 4.12(c), the final chosen constellation symbols and their mappings are denoted as:

$$\tilde{\mathbb{P}}^{2,2} = \left(\begin{bmatrix} 0 \\ 0 \\ 000 \end{bmatrix}, \begin{bmatrix} m_0 \\ 0 \\ 001 \end{bmatrix}, \begin{bmatrix} m_1 \\ m_0 \\ 010 \end{bmatrix}, \begin{bmatrix} m_1 \\ 0 \\ 011 \end{bmatrix}, \begin{bmatrix} 0 \\ m_0 \\ 100 \end{bmatrix}, \begin{bmatrix} 0 \\ m_1 \\ 101 \end{bmatrix}, \begin{bmatrix} m_1 \\ m_1 \\ 110 \end{bmatrix}, \begin{bmatrix} m_0 \\ m_1 \\ 111 \end{bmatrix} \right), \quad (4.37)$$

where each vector corresponds to the binary vectors written below it.

4.5.3.2 Notations

The main goal of this subsection is to generalize the previous notations before formalizing the proposed algorithm for all J . We start by generalizing the notation \mathbb{P} . A set of \tilde{J} -length vectors whose elements are taken from $\{\mathcal{P}_M, \{0\}\}$ is defined as:

$$\mathbb{P}^{M,\tilde{J}} = \left\{ \mathbf{p} = [p_0, p_1, \dots, p_{\tilde{J}-1}]^T \right\}, \text{ where } p_j \in \{\mathcal{P}_M, \{0\}\}.$$

The set $\mathbb{P}^{M,\tilde{J}}$ can be partitioned into $\mathbb{P}^{M,\tilde{J}} = \mathbb{P}_{x_{B-1}}^{M,\tilde{J}} \cup \mathbb{P}_{y_{B-1}}^{M,\tilde{J}} \cup \mathbb{P}_{dc}^{M,\tilde{J}}$, where $x_{B-1} \neq y_{B-1} \in \{0, 1\}$ and they are disjointed from each other. The set $\mathbb{P}_{dc}^{M,\tilde{J}}$ is a set that is not processed for the next step. With respect to our previous example, this set is labeled as a cross marker in Figure 4.12(a). Now, a mean or ‘center of mass’ vector of a subset $\mathbb{P}_{x_{B-1}}^{M,\tilde{J}}$ is defined as:

$$\mathbf{d}_s(\mathbb{P}_{x_{B-1}}^{M,\tilde{J}}) = \frac{1}{|\mathbb{P}_{x_{B-1}}^{M,\tilde{J}}|} \sum_{\mathbf{p} \in \mathbb{P}_{x_{B-1}}^{M,\tilde{J}}} \mathbf{p}, \quad (4.38)$$

which is used to measure the distance between two subsets of $\mathbb{P}^{M,\tilde{J}}$. The subset $\mathbb{P}_{x_B}^{M,\tilde{J}}$ can

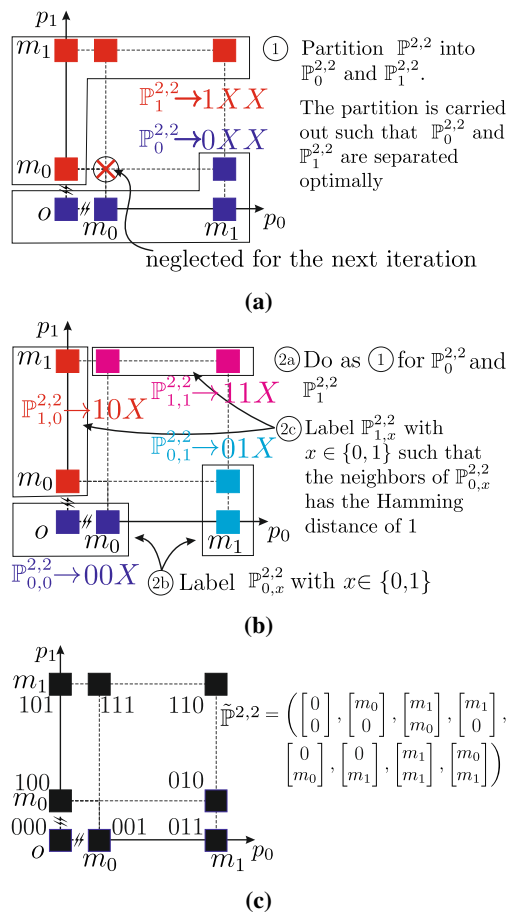


Figure 4.12. (a) The first, (b) the second and (c) the third steps of the set partitioning algorithm.

be further partitioned into $\mathbb{P}_{x_{B-1}}^{M,\tilde{J}} \supset \mathbb{P}_{x_{B-1},x_{B-2}}^{M,\tilde{J}} \cup \mathbb{P}_{x_{B-1},y_{B-2}}^{M,\tilde{J}}$. This partition can be done until the array $[x_{B-1}, x_{B-2}, \dots, x_0]$ is obtained. The subset of $\mathbb{P}^{M,\tilde{J}}$ has a binary vector associated with it, for example with $B = 3$, $\mathbb{P}_{x_{B-1},x_{B-2},x_{B-3}}^{M,\tilde{J}}$ associates with a binary vector $[x_{B-1}, x_{B-2}, x_{B-3}]$.

An *ordered* set \mathcal{B}_B is a collection of B -bit binary vectors that are arranged based on the Gray code, i.e.,:

$$\mathcal{B}_B = (\tilde{\mathbf{b}}_0, \tilde{\mathbf{b}}_1, \dots, \tilde{\mathbf{b}}_{2^B-1}), \quad (4.39)$$

where $\tilde{\mathbf{b}}_i = [\tilde{b}_{i,0}, \tilde{b}_{i,1}, \dots, \tilde{b}_{i,B-1}]^T$, $\tilde{b}_{i,j} \in \{0, 1\}$, $\tilde{b}_{i,0}$ and $\tilde{b}_{i,B-1}$ are the least significant bit (LSB) and the most significant bit (MSB), respectively. A common way to construct \mathcal{B}_B is the iterative and mirroring method from \mathcal{B}_{B-1} [Agrell *et al.*, 2004]. It follows that $[\tilde{b}_{i,0}, \tilde{b}_{i,1}, \dots, \tilde{b}_{i,B-2}]^T = [\tilde{b}_{2^B-1-i,0}, \tilde{b}_{2^B-1-i,1}, \dots, \tilde{b}_{2^B-1-i,B-2}]^T$ for $0 \leq i \leq \left\lfloor \frac{2^B-1}{2} \right\rfloor$, see following examples:

$$\begin{aligned} \mathcal{B}_2 &= \left(\begin{bmatrix} 0 \\ 0 \end{bmatrix}, \begin{bmatrix} 1 \\ 0 \end{bmatrix}, \begin{bmatrix} 1 \\ 1 \end{bmatrix}, \begin{bmatrix} 0 \\ 1 \end{bmatrix} \right), \text{ or} \\ \mathcal{B}_3 &= \left(\begin{bmatrix} 0 \\ 0 \\ 0 \end{bmatrix}, \begin{bmatrix} 1 \\ 0 \\ 0 \end{bmatrix}, \begin{bmatrix} 1 \\ 1 \\ 0 \end{bmatrix}, \begin{bmatrix} 0 \\ 1 \\ 0 \end{bmatrix}, \begin{bmatrix} 0 \\ 1 \\ 1 \end{bmatrix}, \begin{bmatrix} 1 \\ 1 \\ 1 \end{bmatrix}, \begin{bmatrix} 1 \\ 0 \\ 1 \end{bmatrix}, \begin{bmatrix} 0 \\ 0 \\ 1 \end{bmatrix} \right). \end{aligned}$$

This inspires us to change the construction of the set $\mathcal{S}^{\text{GTIM}}$ by means of partitioning the set \mathcal{B}_B .¹ That is, the MSB can be assigned first by following the Gray code without worrying about the other bits. In fact, it can be shown that the bit mapping shown in Figure 4.12 follows the iterative method discussed in [Agrell *et al.*, 2004].

Generally for $J > 2$, we need a container set denoting the elements that have been chosen and labeled. Let the set \mathcal{S} be an ordered set whose elements are indexed by the binary digit \mathbf{b}_l . As an example, see (4.27), where $\mathbf{b}_l = [b_{l,0}, b_{l,1}]^T = [0, 0]^T$ indexes the 0th element, and

¹Note that the name set partitioning is also used in [Ungerboeck, 1982], but ours is different in the terms of the method used to partition and label the set. In addition, the algorithm in [Ungerboeck, 1982] does not discuss a method on how to choose a set of constellation symbols whose cardinality is smaller than the set of all possible constellation symbols. Joint Euclidean-distance and Hamming-distance search is also not discussed in [Ungerboeck, 1982].

$[b_{l,0}, b_{l,1}]^T = [1, 0]^T$ indexes the 1st element. An ordered set \mathbb{S}_{J-j}^M is defined as:

$$\mathbb{S}_{J-j}^M = \left(\begin{bmatrix} \mathbf{x} \\ s_{J-j} \\ \vdots \\ s_{J-2} \\ s_{J-1} \end{bmatrix} \right), \quad s_{J-j} \in \{\mathcal{P}_M, \{0\}\}, \text{ for } j \in \{0, 1, \dots, J-1\},$$

where \mathbf{x} is the $(J-j)$ -length column vector denoting the elements that *have not been defined yet*. In other words, \mathbb{S}_{J-j}^M defines an ordered set where the $(J-j)^{\text{th}}$ to the $(J-1)^{\text{th}}$ elements *have been ordered and labeled*. For example with $M = 3$, $B = 6$, $J = 3$, $j = 1$ and:

$$\mathbb{S}_{3-1}^3 = \left(\begin{bmatrix} \mathbf{x} \\ 0 \\ \textcolor{blue}{00}XXXX \end{bmatrix}, \begin{bmatrix} \mathbf{x} \\ m_0 \\ \textcolor{red}{01}XXXX \end{bmatrix}, \begin{bmatrix} \mathbf{x} \\ m_2 \\ \textcolor{blue}{10}XXXX \end{bmatrix}, \begin{bmatrix} \mathbf{x} \\ m_1 \\ \textcolor{red}{11}XXXX \end{bmatrix} \right). \quad (4.40)$$

means that 2-length column vector \mathbf{x} has not been defined; moreover, the 2nd to the 3rd elements have been ordered and labeled accordingly. The set \mathcal{S} will be assigned as $\mathcal{S} = \mathbb{S}_0^M$ if all elements have been ordered and labeled. We use a convention that if no element has been assigned, then it is denoted by \mathbb{S}_J^M .

4.5.3.3 The Proposed Set Partitioning Algorithm

A complete pseudocode for the proposed set partitioning algorithm is given in Algorithm 1 for a given M , B and J . The main difference with the previous simple example is that for $J > 2$, the operation SP can be invoked multiple times. In addition, \tilde{J} of J elements can be processed at once. The advantage of doing this is that it is more modular and more computationally efficient as the previously-defined mapping set can be reused.

In line 3, J_b denotes a parameter to control the number of steps, so that they are upper bounded by $J - J_b + 1$. The statement $J_b\eta = \lfloor J_b\eta \rfloor$ is used to avoid rounding the number of allocated bits to label \mathbb{S}_0^M . The variable J_{it} is used as a step size for the loop process in line 6 in Algorithm 1. In line 6(h), B_{sp} denotes the number of bits required for labeling the set $\mathbb{S}_{J-(j-\tilde{J})}^M$ during the partitioning and labeling process, which is named as $\text{SP}(\cdot)$ in line 6(i). Specifically, $\text{SP}(\tilde{J}, B_{\text{sp}}, \mathbb{S}_{J-(j-\tilde{J})}^M)$ reads so that the \tilde{J} elements of the vector in the set $\mathbb{S}_{J-(j-\tilde{J})}^M$ will be

Algorithm 1 The proposed set partitioning algorithm parameterized by (M, B, J, J_b)

1. Set M, B and J .
 2. Calculate $\eta = B/J$.
 3. Set J_b such that $J_b\eta = \lfloor J_b\eta \rfloor$ and $J_b \in \{1, 2, \dots, J\}$.
 4. Calculate $J_{it} = \inf(\{k \mid k \in \{1, 2, \dots, J\}, k\eta = \lfloor k\eta \rfloor\})$.
 5. Initialize \mathbb{S}_J^M and assign $j = 0$.
 6. (a) do
 - (b) if $J - j \neq J_b$
 - (c) $\tilde{J} = J_{it}$;
 - (d) else
 - (e) $\tilde{J} = J_b$;
 - (f) end
 - (g) $j = j + \tilde{J}$;
 - (h) $B_{sp} = \tilde{J}\eta$;
 - (i) $\mathbb{S}_{J-j}^M = SP(\tilde{J}, B_{sp}, \mathbb{S}_{J-(j-\tilde{J})}^M)$; // partition $\mathbb{S}_{J-(j-\tilde{J})}^M$
 - (j) while $j < J$
 7. Output $\mathcal{S}^{GTIM} = \mathbb{S}_0^M$.
-

labeled with B_{sp} bits, and the output is denoted as \mathbb{S}_{J-j}^M . The function SP will be formalized in the next subsection (at the first step of the first example). The steps detailed in lines 6(b-i) are repeated until $j = J$. Therefore, if $J_b = J$, then only 1 step is required. Generally, J_b can be interpreted as the number of elements of a vector in \mathbb{S}^M that will be labeled at once in one step. Finally, the algorithm outputs \mathcal{S}^{GTIM} as $\mathcal{S}^{GTIM} = \mathbb{S}_0^M$.

4.5.3.4 More Examples

- I) The algorithm with $(M = 2, B = 3, J = 2, J_b = 2)$:

This configuration refers to the example that is previously discussed and illustrated in Figure 4.12. In this example, the number of loops is one as $J_b = 2$. Algorithm 1 reduces to $\mathcal{S}^{GTIM} = \mathbb{S}_0^2 = SP(2, 3, \mathbb{S}_2^2)$. The steps taken in Figures 4.12(a-c) are formalized as following.

The 1st step (Figure 4.12(a)): The first step is to partition $\mathbb{P}^{2,2}$ into $\mathbb{P}_0^{2,2}$ and $\mathbb{P}_1^{2,2}$ such

that:

$$\left(\mathbb{P}_0^{2,2}, \mathbb{P}_1^{2,2}\right) = \arg \max_{\mathbb{P}_0^{2,2}, \mathbb{P}_1^{2,2}} \left\| \mathbf{d}_S \left(\mathbb{P}_0^{2,2} \right) - \mathbf{d}_S \left(\mathbb{P}_1^{2,2} \right) \right\| \quad (4.41)$$

subject to:

$$\left| \mathbb{P}_0^{2,2} \right| = \left| \mathbb{P}_1^{2,2} \right| = \lfloor (M+1)^J/2 \rfloor, \quad (4.42)$$

$$\mathbb{P}_0^{2,2} \neq \mathbb{P}_1^{2,2} \neq \emptyset, \mathbb{P}_0^{2,2}, \mathbb{P}_1^{2,2} \subset \mathbb{P}^{2,2} \text{ and } \mathbb{P}_0^{2,2} \cap \mathbb{P}_1^{2,2} = \emptyset. \quad (4.43)$$

The expression in (4.41) guarantees that $\mathbb{P}_0^{2,2}$ and $\mathbb{P}_1^{2,2}$ have the farthest distance with the constraints (4.42) and (4.43). The expression in (4.42) indicates that both set $\mathbb{P}_0^{2,2}$ and $\mathbb{P}_1^{2,2}$ must contain $\lfloor (M+1)^J/2 \rfloor$ elements. This is equivalent to:

$$\lfloor \log_2 |\mathbb{P}_0^{2,2}| \rfloor = \lfloor \log_2 |\mathbb{P}_1^{2,2}| \rfloor \geq B_{sp} - 1,$$

which means that the partitioned sets $\mathbb{P}_0^{2,2}$ and $\mathbb{P}_1^{2,2}$ can be at least represented by $B_{sp} - 1$ bits. The vectors in $\mathbb{P}_0^{2,2}$ and $\mathbb{P}_1^{2,2}$ will be assigned with the same $2^{B_{sp}-1}$ binary vectors, which will be each appended by a new binary bit as the MSB. It is intuitive that (4.41) can be found in the outer layer of $\mathbb{P}^{2,2}$, see Figure 4.13 for more examples and observe the positions of a collection of binary vectors that differs only at the MSB. This can be seen in the red and blue markers.

The 2nd step (Figure 4.12(b)): At the 2nd step, the sets $\mathbb{P}_0^{2,2}$ and $\mathbb{P}_1^{2,2}$ can be further partitioned into $\mathbb{P}_{0,0}^{2,2}$, $\mathbb{P}_{0,1}^{2,2}$, $\mathbb{P}_{1,0}^{2,2}$ and $\mathbb{P}_{1,1}^{2,2}$. The arrangement of all the sets is done such that $\mathbb{P}_{0,1}^{2,2}$ is the neighbor of $\mathbb{P}_{1,1}^{2,2}$ as the Hamming distance of the bits associated with both sets is 1. Doing this ensures that the MSB and the next bit position of binary vectors of $\mathbf{s}_l \in \mathbb{P}_{0,1}^{2,2}$ and $\mathbf{s}_l \in \mathbb{P}_{1,1}^{2,2}$ have the Hamming distance of 1.

The 3rd step (Figure 4.12(c)): The same procedures in the 2nd step can be repeated in the 3rd step. Alternatively, we can assign the LSB of the elements of \mathcal{S}^s and arrange it such that it differs only at 1-bit position with their neighbors. The output of the third step is the ordered set $\tilde{\mathbb{P}}^{2,2}$ as shown in Figure 4.12(c). Notice that the Hamming distance between two neighboring binary vectors is 1; moreover, the Hamming distance with the next neighbors is 2 and so on. Translating these processes with respect to (4.36), the function SP ensures that the farther constellation point has a larger Hamming distance. Other examples with $J = 2$ and different values of M and B can be found in Figure 4.13.

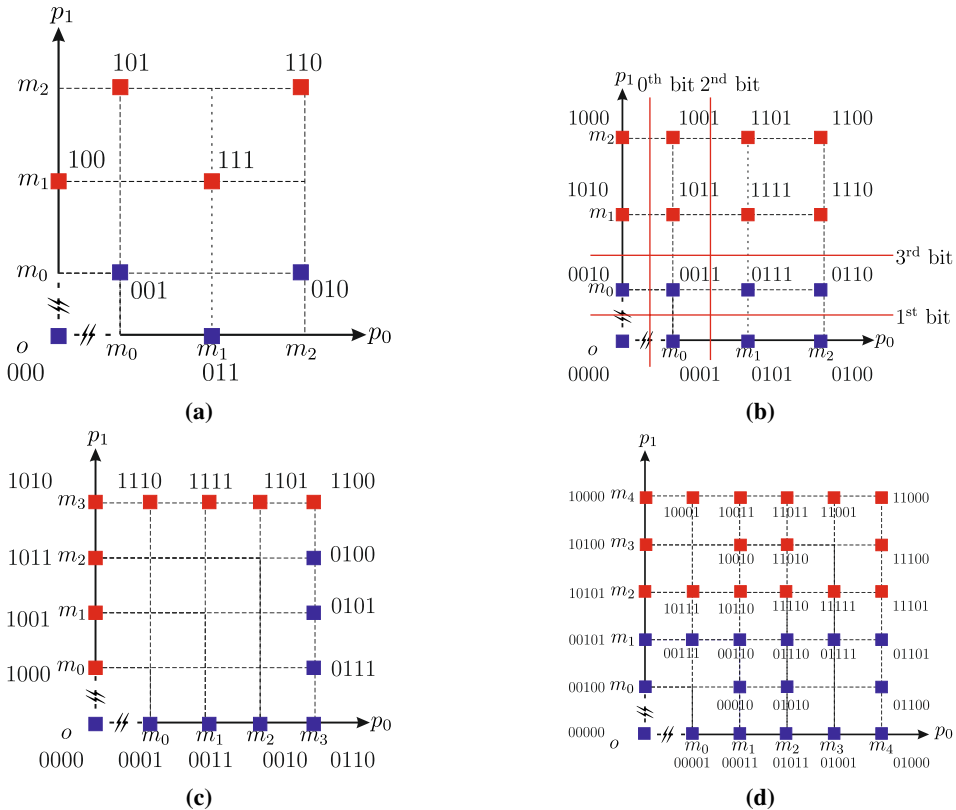


Figure 4.13. $\text{SP}(\cdot)$ with: (a) $M = 3, B = 3$ and $\eta = 1.5$; (b) $M = 3, B = 4$ and $\eta = 2$; (c) $M = 4, B = 4$ and $\eta = 2$; (d) $M = 5, B = 5$ and $\eta = 2.5$.

II) The algorithm with ($M = 2, B = 6, J = 4, J_b = 2$):

Instead of $J = 2$, now we extend the previous example to $J = 4$. In this example, it can be shown that the already-defined codebook can be used to design another codebook with higher dimensions. Furthermore, there are 2 iterations, and at each iteration $\text{SP}(2, 3, \mathbb{S}_{J-(j-2)}^M)$ is performed, which is already illustrated in Figure 4.12. The output of the first iteration, i.e., $\mathbb{S}_{4-2}^M = \text{SP}(2, 3, \mathbb{S}_{4-0}^M)$, is given as:

$$\mathbb{S}_{4-2}^2 = \left(\begin{array}{cccccccc} \begin{bmatrix} \mathbf{x} \\ 0 \\ 0 \end{bmatrix}, & \begin{bmatrix} \mathbf{x} \\ m_0 \\ 0 \end{bmatrix}, & \begin{bmatrix} \mathbf{x} \\ m_1 \\ m_0 \end{bmatrix}, & \begin{bmatrix} \mathbf{x} \\ m_1 \\ 0 \end{bmatrix}, & \begin{bmatrix} \mathbf{x} \\ 0 \\ m_0 \end{bmatrix}, & \begin{bmatrix} \mathbf{x} \\ 0 \\ m_1 \end{bmatrix}, & \begin{bmatrix} \mathbf{x} \\ m_1 \\ m_1 \end{bmatrix}, & \begin{bmatrix} \mathbf{x} \\ m_0 \\ m_1 \end{bmatrix} \\ \textcolor{red}{000XXX} & \textcolor{blue}{001XXX} & 010XXX & 011XXX & 100XXX & 101XXX & 110XXX & 111XXX \end{array} \right).$$

In this case, the length of the vector \mathbf{x} is two. At the last iteration, we have $J_b = 2$ and the output is $\mathcal{S}^{\text{GTIM}} = \mathbb{S}_{4-4}^M$ as expressed as:

$$\mathbb{S}_{4-4}^2 = \left(\begin{array}{cccccccc} \begin{bmatrix} 0 \\ 0 \\ 0 \\ 0 \end{bmatrix}, & \begin{bmatrix} m_0 \\ 0 \\ 0 \\ 0 \end{bmatrix}, & \begin{bmatrix} m_1 \\ m_0 \\ 0 \\ 0 \end{bmatrix}, & \begin{bmatrix} m_1 \\ 0 \\ 0 \\ 0 \end{bmatrix}, & \begin{bmatrix} 0 \\ m_0 \\ 0 \\ 0 \end{bmatrix}, & \begin{bmatrix} 0 \\ m_1 \\ 0 \\ 0 \end{bmatrix}, & \begin{bmatrix} m_1 \\ m_1 \\ 0 \\ 0 \end{bmatrix}, & \begin{bmatrix} m_0 \\ m_1 \\ 0 \\ 0 \end{bmatrix}, \\ \textcolor{red}{000000} & \textcolor{red}{000001} & \textcolor{red}{000010} & \textcolor{red}{000011} & \textcolor{red}{000100} & \textcolor{red}{000101} & \textcolor{red}{000110} & \textcolor{red}{000111} \\ \begin{bmatrix} 0 \\ 0 \\ m_0 \\ 0 \end{bmatrix}, & \begin{bmatrix} m_0 \\ 0 \\ m_0 \\ 0 \end{bmatrix}, & \begin{bmatrix} m_1 \\ m_0 \\ m_0 \\ 0 \end{bmatrix}, & \begin{bmatrix} m_1 \\ 0 \\ m_0 \\ 0 \end{bmatrix}, & \begin{bmatrix} 0 \\ m_0 \\ m_0 \\ 0 \end{bmatrix}, & \begin{bmatrix} 0 \\ m_1 \\ m_0 \\ 0 \end{bmatrix}, & \begin{bmatrix} m_1 \\ m_1 \\ m_0 \\ 0 \end{bmatrix}, & \begin{bmatrix} m_0 \\ m_1 \\ m_0 \\ 0 \end{bmatrix}, \dots \\ \textcolor{blue}{001000} & \textcolor{blue}{001001} & \textcolor{blue}{001010} & \textcolor{blue}{001011} & \textcolor{blue}{001100} & \textcolor{blue}{001101} & \textcolor{blue}{001110} & \textcolor{blue}{001111} \end{array} \right).$$

Notice that the vector \mathbf{x} is replaced with the result as depicted in Figure 4.12(c), and the binary representation is appended by replacing the LSBs with new ordered binary vectors.

 III) The algorithm with ($M = 3, B = 6, J = 3, J_b = 2$):

The main purpose of this example is to visualize the modularity of the algorithm. At the first iteration, the process $\mathbb{S}_{3-1}^3 = \text{SP}(1, 2, \mathbb{S}_{3-0}^3)$ is carried out. The output can be expressed as in (4.40). Visually, it is equivalent to the order and label the symbol s_2 in $\mathcal{S}^{\text{GTIM}}$, which can be shown in Figure 4.14 along s_2 -axis. Then, on each plane with respect to the s_2 -axis, $\mathcal{S}^{\text{GTIM}} = \mathbb{S}_{3-3}^3 = \text{SP}(2, 4, \mathbb{S}_{3-1}^3)$ is performed. Notice that the

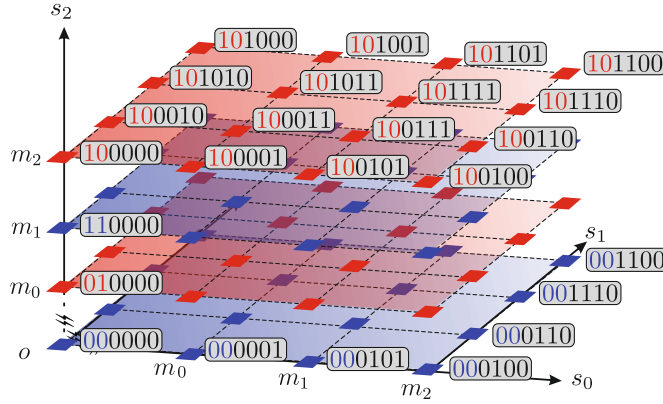


Figure 4.14. An illustration for the proposed algorithm with $(3, 6, 3, 2)$.

constellation for $\text{SP}(2, 4, \mathbb{S}_{3-1}^3)$ is shown in Figure 4.13(b). Therefore, the final result can be seen in Figure 4.14, which shows the arrangement of Figure 4.13(b) on each plane. The location of each plane is denoted by (4.40), which is carried out in the first iteration, i.e., $\text{SP}(1, 2, \mathbb{S}_{3-0}^3)$.

4.5.3.5 Miscellaneous

First, the effect of J_b , which parameterizes Algorithm 1, will be discussed. Recall that the arrangement in Figure 4.13(c) has $J_b = 2$. Alternatively, we can also set $J_b = 1$ for the same problem. The result is shown in Figure 4.15(a). It is obvious that the arrangement in Figure 4.15(a) has a worse BER compared to Figure 4.13(c). This can be seen easily by looking at pairs of symbols that have the Hamming distance of 2. There are pairs with a Hamming distance of 2 in Figure 4.15(a) that have a smaller Euclidean distance than that of Figure 4.13(c). Furthermore, we can also find the same observation with $J_b = 3$ and $J_b = 2$.

It is also worth discussing here that if $|m_0 - I_0| < |m_i - m_j|, \forall i \neq j \in \{0, 1, \dots, M-1\}$ then the BER is limited by $|m_0 - I_0|$. Therefore, in order to maintain the BER gain of SC-GTIM, a minor modification for the function SP is required. The modification is carried out such that the set $\mathbb{P}_{dc}^{M, \tilde{J}}$ is predefined to include the vectors $\mathbf{p} \in \mathbb{P}^{M, \tilde{J}}$ that contain the value m_0 . It means that the vectors containing the value m_0 are not used. Figure 4.15(b) illustrates the aforementioned modification with the red cross, which denotes the unused vectors.

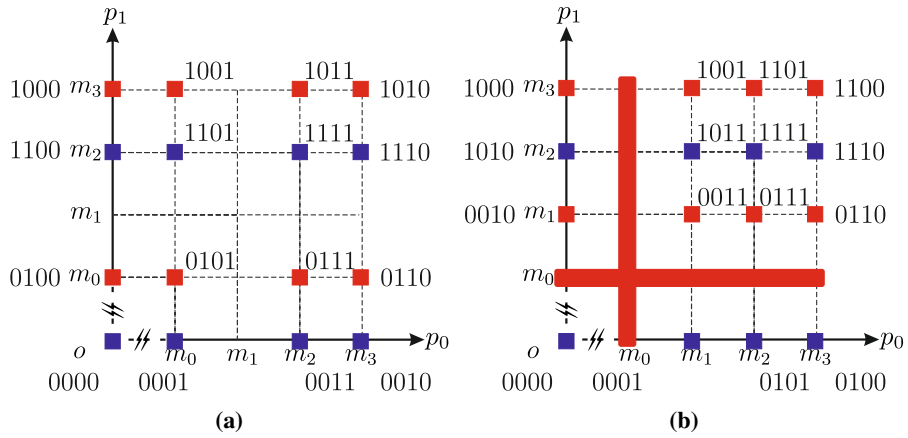


Figure 4.15. (a) An output of Algorithm 1 with (4,4,2,1) and (b) a modified construction of Figure 4.13(c) if $|m_0 - I_0| < |m_i - m_j|, \forall i \neq j \in \{0, 1, \dots, M-1\}$.

4.5.3.6 Performance Evaluation: Single-Carrier Modulation Systems

In this subsection, performance comparisons of single-carrier modulation systems are provided. The assumptions and the system models are taken from the descriptions in Chapter 2. For example, two scenarios depicted in Figure 2.14(a) and Figure 2.14(c) are used. Recall that Figure 2.14(a) shows a realization of a simple office environment with a strong LoS signal, and Figure 2.14(b) shows a link that does not have an LoS. In this subsection, we will focus on these two extreme cases, while in Chapter 4.7, thousands of realizations are used to evaluate the performances. Similar to Chapter 3.6.3, an uplink scenario is assumed. The main reason for this is due to the use of IR spectrum that might be useful for a general study of LiFi outside this thesis because the typical assumption is that the downlink transmission is carried out over the VL spectrum and uplink transmission is carried out over the IR spectrum [Haas *et al.*, 2016; Chen *et al.*, n.d.]. The characteristics of the light emitter and receiver also follow the descriptions in Chapter 2, which include frequency responses and the linear dynamic range. The configuration of the THP system follows the rule of thumb from [Purwita, Chen, *et al.*, 2019], i.e., ϵ in (4.14) is chosen such that the gain of precoder is unity. This case can be achieved if ϵ is set to be ϵ_{th} , where:

$$\epsilon_{\text{th}} = \frac{I_b - I_a}{2} \left(\sqrt{\frac{M+1}{M-1}} - 1 \right). \quad (4.44)$$

Figure 4.16 shows the BER results with different constellation size, M . Note that the CP length is 64. The legend 'Theoretical AWGN' refers to the BER of M -PAM of uncoded AWGN

channels. Its value is taken from [Proakis, 2007], i.e.,:

$$P_b^{\text{AWGN}} = \frac{2}{\log_2(M)} \left(1 - \frac{1}{M}\right) Q \left(\sqrt{\frac{6 \log_2 M}{M^2 - 1} \frac{E_b}{N_0}} \right), \quad (4.45)$$

where $Q(\cdot)$ denotes the Q -function. Analytical BERs are denoted by the legends 'theory'. BER of PAM-SCFDE follows that from [Purwita *et al.*, 2020]. That is,

$$P_b^{\text{PAM-SCFDE}} \approx \frac{2}{\log_2 M} \left(1 - \frac{1}{M}\right) Q \left(\sqrt{\frac{1.5(I_b - I_a)^2 \log_2(M)}{(M-1)^2 \left(2(I_a^2 + I_a I_b + I_b^2) + \frac{(I_b - I_a)^2}{M-1}\right)} \frac{E_b}{N_0}} \right). \quad (4.46)$$

Meanwhile, the analytical BER for SC-GTIM uses its average PEP as shown (4.31).

A general observation from Figure 4.16 is that, within the set of enhanced single carrier modulation systems, there is no system that is dominant over the other. However, it is expected that the vanilla version is generally inferior compared to the improved ones. Another observation is that the degradation rate of the DFE system is faster than others as the constellation size increases, which shows the effect of error propagations. By comparing the THP results to the DFE results, notice that the relative performance is flipped. That is, the THP system is worse at the low spectral efficiency region, but it is better at the medium spectral efficiency region. It has been explained in [Purwita, Chen, *et al.*, 2019] that this fact is due to the effect of ϵ as introduced in (4.14). Based on (4.44), ϵ_{th} is monotonically decreasing with respect to M , which means that at a low M , ϵ_{th} is larger than that at a high M . Having a large ϵ_{th} causes a smaller linear region at the output of precoder, which further reduces the error performance [Purwita, Chen, *et al.*, 2019]. Therefore, the advantage of THP systems can be obtained at a moderate-to-high spectral efficiency region [Purwita, Chen, *et al.*, 2019]. In this regard, we can benefit from the additional symbol from SC-GTIM. Hence, it can be seen from Figure 4.16 that SC-GTIM outperforms the others at a lower spectral efficiency region. Figure 4.16 also shows that the relative error performance of a single-carrier modulation system compared to the others is consistent as the user moves away from the AP.

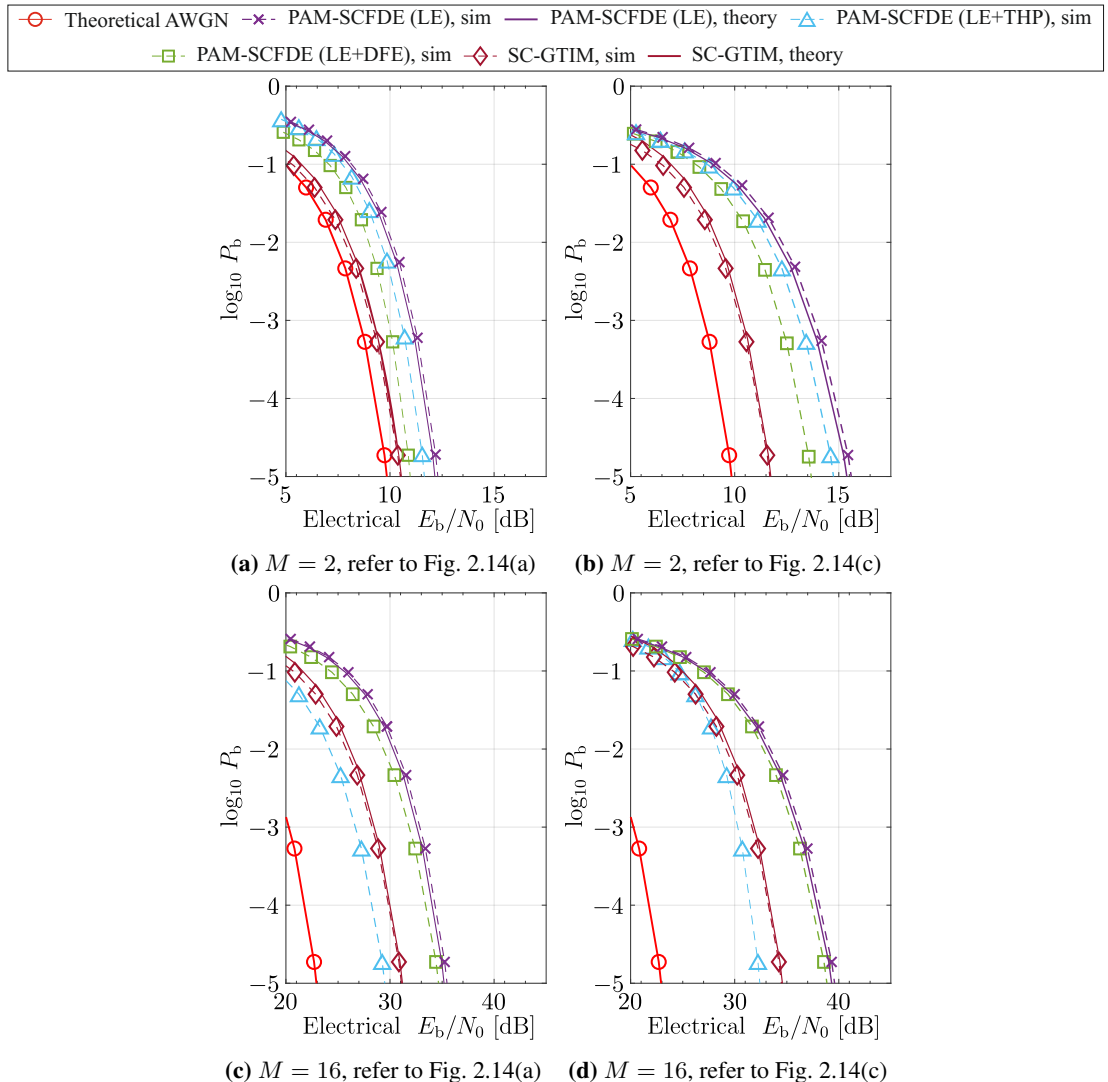


Figure 4.16. BER comparisons of single carrier modulation systems with respect to the scenarios depicted in Figure 2.14(a) and Figure 2.14(c).

4.6 IEEE 802.11bb-Compliant OFDM Systems

In this section, the discussion switches to multi carrier modulation systems. First, this section begins with the common mode of IEEE 802.11bb [Serafimovski, Han, Weszely, *et al.*, 2019]. Right after that, an improved version, which also utilizes the output waveform of an IEEE 802.11ax, called IQ-WDM [Purwita & Haas, 2020a], is discussed.

4.6.1 The Common Mode of IEEE 802.11bb

Prior to the decision of the common mode of IEEE 802.11bb, there were two main PHY proposals, i.e.,:

1. the light communications (LC)-optimized PHY [Jungnickel *et al.*, 2019], which is now an optional mode of IEEE 802.11bb, and
2. the existing PHY for LC [Serafimovski, Han, Haas, *et al.*, 2019], which is now the common mode of IEEE 802.11bb.

The latter is chosen as the common mode mainly due to the fact that the flatness test with a signal bandwidth of 20 MHz conducted over the benchmarked TGbb reference channel models [Uysal *et al.*, 2018] show flat channels in most cases [Purwita *et al.*, 2019; Purwita & Haas, 2020b]. Consequently, in most cases, computing resources will be wasted to run the adaptive bit-and-power allocations. Another reason is that it is more straightforward to implement a LiFi system, which should support multiple users, by reusing an existing WiFi chipset. Note that at the time of the discussion of these PHY proposal being held, the LC-optimized PHY, which is based on [ITU-T G.9991, 2019], does not support a multi-user communication. Hence, more effort is required to map the 802.11 MAC frames to the G.vlc PHY packets. Therefore, one of the important decisions made for the common mode is that the mandatory PHY of IEEE 802.11bb will use the high efficiency (HE) waveform of IEEE 802.11ax.

Another important decision is the wavelength for the mandatory, common mode of IEEE 802.11b. It has been decided that the wavelength range from 800 nm to 1,000 nm will be used for transmission. The main reason for this is due to the responsivity of Silicon-based PDs being higher in this range compared to that in the VL range as shown in Figure 2.1.

The block diagram of the mandatory PHY is shown in Figure 4.17. The IQ waveform that

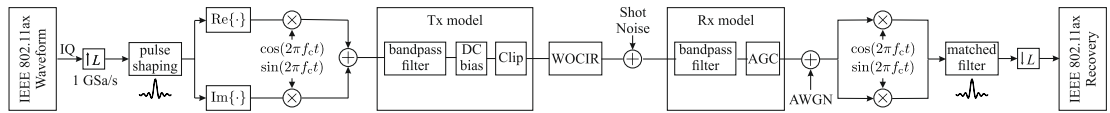


Figure 4.17. The mandatory PHY of IEEE 802.11bb: frequency up-and-down conversion method.

complies with that of IEEE 802.11ax [IEEE P802.11 TGax, 2018] is generated. In this thesis, in order to make sure that the waveform complies with the technical specification of IEEE 802.11ax [IEEE P802.11 TGax, 2018], the WLAN toolbox from MATLAB[®] [MATLAB[®], 2020] is used. Then, the waveform is upsampled to 1 GSa/s. The upsampling ratio is chosen based on the sampling time of the TGbb reference channel model [Uysal *et al.*, 2018]. Then a pulse shaping is added afterward. The frequency conversion is then conducted so that the baseband IQ waveform is centered at f_c . Both Tx and Rx frontend models are already described in Ch 2. The upconverted signal is transmitted over a wireless optical channel impulse response (WOCIR) with the sampling time of 1 ns. AWGN and shot noise models are added next. Finally, the downconversion, match filtering, and downsampling are conducted before recovering the transmitted waveform.

Just recently, the center frequency f_c has been agreed in TGbb, and the corresponding motion is documented in [Purwita, Rossius, *et al.*, 2020]. There have been a long discussion on it, e.g., [Purwita & Haas, 2020b; Purwita, Haas, Serafimovski, Afgani, *et al.*, 2020; Purwita, Haas, Serafimovski, & Berner, 2020; Rossius *et al.*, 2020; Serafimovski *et al.*, 2020]. Based on [Purwita, Rossius, *et al.*, 2020], given that the signal bandwidth is B , then the center frequency is assumed to be $f_c = B/2 + 16$ MHz for $B \in \{20, 40, 80, 160\}$ MHz. The constant 16 MHz is exhaustively searched over all realizations of TGbb reference channel models [Uysal *et al.*, 2018]. An important observation from the exhaustive search done in [Purwita & Haas, 2020b; Purwita, Haas, Serafimovski, Afgani, *et al.*, 2020; Purwita, Haas, Serafimovski, & Berner, 2020] is that f_c cannot be too close to the DC frequency due to the spectral leakage. The center frequency f_c cannot be too far from DC frequency either due to the LPF characteristic of LiFi channel [Jungnickel *et al.*, 2002].

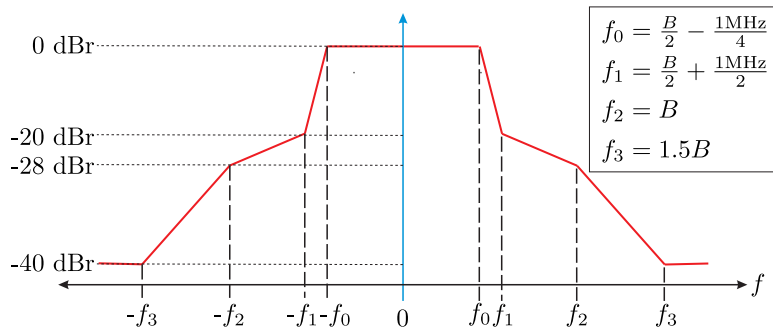


Figure 4.18. The spectrum mask of the IEEE 802.11ax OFDM waveform [IEEE P802.11 TGax, 2018]. B denotes the signal bandwidth, where $B \in \{20, 40, 80, 160\}$ MHz.

4.6.2 IQ-WDM

4.6.2.1 Motivation

In order to see the motivation of IQ-WDM, it is important to show a spectrum mask of the IEEE 802.11ax OFDM waveform as depicted in Figure 4.18. In addition, it is imperative to highlight the characteristics of the wireless optical channel. It has been concluded that the diffuse channel (see (2.6) with $k = 1$) has an LPF characteristic. For example, Figure 4.19 shows the normalized magnitude responses of channels shown in Figures 2.14 that are calculated by using `owcsimpy`. The blue and red curves in Figure 4.19 associate to the scenario depicted in Figure 2.14(b) and (c), respectively. Recall that the scenario depicted in Figure 2.14(b) has a LoS link, while the scenario depicted in Figure 2.14(c) does not. It can be seen that the channel has an LPF characteristic. Suppose the signal bandwidth is $B = 20$ MHz, $f_c = 26$ MHz, and an IEEE 802.11bb-compliant LiFi system is applied in those three cases, then the system will perform badly in the third case, due to the high attenuation at the frequency range around 20 MHz. In order to support this argument, Figure 4.20 shows packet error ratios (PERs) by using the packet length of 1,458 bytes that are transmitted over the channel Figure 4.19 for the case 3. Note that the use of PER and the packet length follows the description in the TGbb methodology document [Bober *et al.*, 2019]. We can see that the error performance is much worse compared to that when the center frequency is close to the DC region. It is worth noting here that even in the region near DC, we can see a degradation of PER. The main reason for this is due to the aliasing at that region, which is illustrated by Figure 4.21. The sidelobes are intersecting at the region near DC.

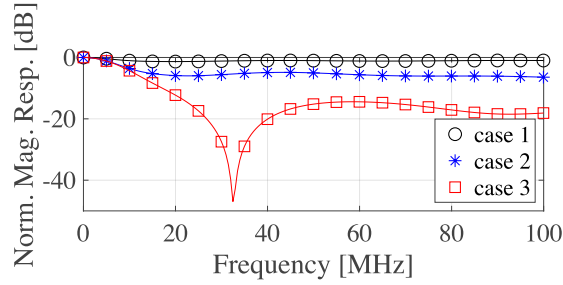


Figure 4.19. The normalized magnitude responses of the CIRs shown in Figures 2.15(b), (d), and (f).

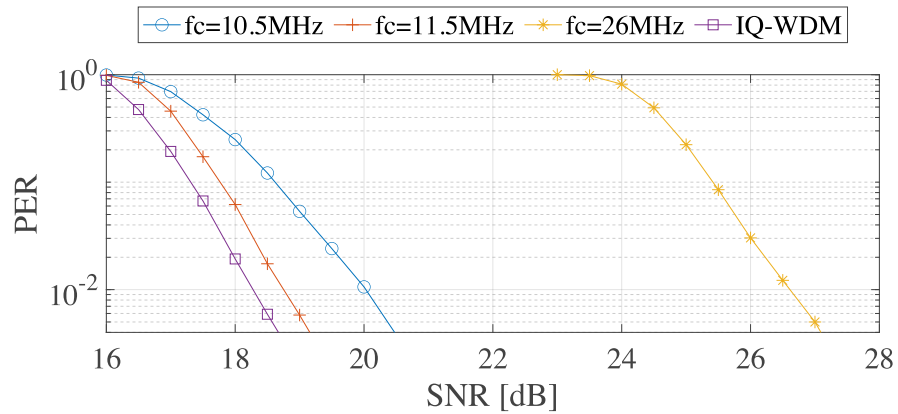


Figure 4.20. PERs of PHY of IEEE 802.11bb over the channel depicted in Figure 4.18 for case 3, 64-QAM, and the coding rate of 3/4. Note that the PER performance of IQ-WDM is

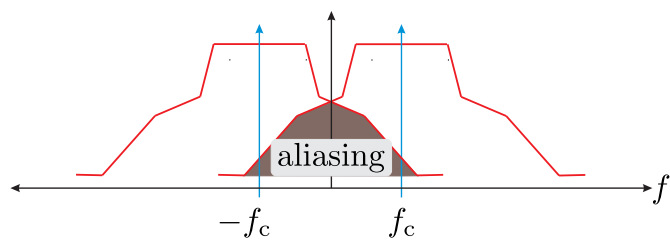


Figure 4.21. Aliasing phenomenon of the PHY common mode IEEE 802.11bb.

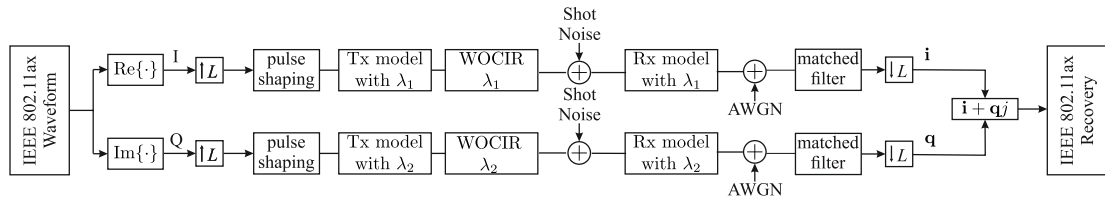


Figure 4.22. The block diagram of IQ-WDM.

4.6.2.2 Solution

IQ-WDM circumvents the above problem by keeping the waveform centered at the DC. The IQ signal is transmitted over 2 different wavelengths, denoted by λ_1 and λ_2 , as depicted in Figure 4.22. Other than using the frontends that operate at λ_1 and λ_2 , other processing blocks are kept the same as those shown in Figure 4.17. In [Purwita & Haas, 2020a], the issues with gain and delay imbalances are discussed. The gain imbalance comes from the fact that the reflectivities of the indoor surfaces are varied depending on the wavelength. Different responsivities of PDs, for example as shown in Figure 2.1, also cause the gain imbalance. Other than a gain imbalance, different distances between each pair of emitters and a PD yields the delay imbalance. It is shown in [Purwita & Haas, 2020a] that if positions of the light emitters and PDs in a mobile device are close to each other (e.g., around 5 cm), then the gain and delay imbalances are negligible. This conclusion is taken by comparing PERs for different scenarios.

The PER is obtained by using two different wavelengths, i.e., $\lambda_1 = 850$ nm and $\lambda_2 = 940$ nm. Notice that in this scenario, a 0.5 dB gain can be achieved with respect to the PHY common mode of IEEE 802.11bb with $f_c = 11.5$ MHz. More than 6 dB gain can be achieved compared to the PHY common mode of IEEE 802.11bb with $f_c = 26$ MHz, which suffers from a high attenuation at the frequency around 30 MHz. In the next section, comparisons of both single and multi carrier systems are provided.

4.7 Performance Comparison

Both single and multi carrier modulation schemes have been discussed in this chapter. Inspired by [Nuwanpriya *et al.*, 2015], both modulation techniques are simultaneously compared in this section. Figure 4.23 depicts the comparisons. The simulation results, which are shown by markers only, are obtained by averaging the BER results at 10^{-5} over 10,000 channel real-

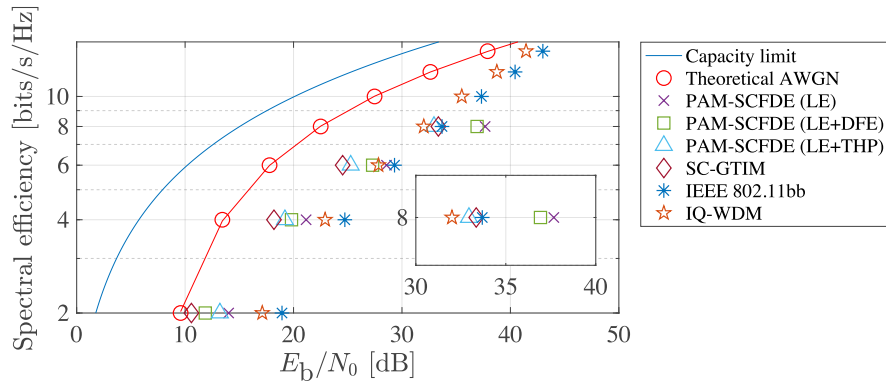


Figure 4.23. Performance comparisons of different modulation techniques at BER of 10^{-5} .

izations in the simple office environment as discussed in Ch 2.3.3. The reason for taking the average over many channel realizations is to draw a general conclusion and compare all modulation schemes. For this comparison, the BERs of the PHY of IEEE 802.11bb and IQ-WDM are calculated without the use of forward error correction (FEC). The metric E_b/N_0 is obtained based on [Bober *et al.*, 2019], i.e.,:

$$\frac{E_b}{N_0} = \text{SNR} + \frac{f_{\text{samp}}}{f_{\text{sym}}} \log_2 M, \quad (4.47)$$

where f_{samp} denotes the sampling rate, which is 1 Gsamples/s, and f_{sym} denotes a symbol rate. The capacity limit in Figure 4.23 refers to [Proakis, 2007, 4.6-10]. Other assumptions, such as the frequency responses of light emitter and receiver, use the models described in Chapter 2.

A general conclusion from Figure 4.23 is similar to that of [Nuwanpriya *et al.*, 2015]. That is, single-carrier modulation techniques are superior in the low-to-medium spectral efficiency. Within this range, the improved versions of PAM-SCFDE are generally better (up to 4 dB) than that of the conventional one. Adding a DFE improves PAM-SCFDE in a low spectral efficiency. However, the improvement is diminishing as the spectral efficiency goes higher due to the error propagation. This is where the THP systems perform best. For example, at the spectral efficiency of 8 bps/Hz, the gain of the THP system is around 3.6 dB compared to 0.2 dB, which is the gain of the DFE system. As SC-GTIM benefits from larger Euclidean and Hamming distances, it is better than the others up to the spectral efficiency of 6 bps/Hz. At the spectral efficiency of 8 bps/Hz, the THP system is 0.1 dB better.

The performance comparisons of IQ-WDM and the common mode PHY show the superiority

of IQ-WDM. That is, IQ-WDM is 2-dB better than that of the common mode, which suffers from both the aliasing and the LPF characteristics of the LiFi channels. However, the IQ-WDM still uses twice the transmitter chain.

4.8 Summary

In this chapter, both single and multi carrier modulation schemes are discussed. PAM-SCFDE is used as a foundation for its enhanced versions, i.e., PAM-SCFDE with DFE and THP. While the improved version can benefit from DFE at the low spectral efficiency region, it suffers from the error propagation at the medium spectral efficiency region. At this range, the THP system is robust against the error propagation. PAM-SCFDE is also enhanced by adopting IM, which is referred to SC-GTIM. Due to larger Euclidean and Hamming distances, SC-GTIM has better error performance compared to the others. At the medium-to-high spectral efficiency region, the multi-carrier schemes outperform the single-carrier ones. In this chapter, the common mode PHY of IEEE 802.11bb and its enhanced version, called IQ-WDM, are discussed. Due to the aliasing at near DC frequency and the LPF characteristics of LiFi channels, IQ-WDM outperforms the common mode by 2 dB at the expense of doubling the transmitter chain.

Chapter 5

Hybrid WiFi-LiFi: Determining the LiFi Offloading Capability

5.1 Introduction

This chapter aims to answer the following question:

“What is the offload potential of a LiFi network in a hybrid WiFi-LiFi network architecture?”

Indeed this question is very general, and the problem formulation will be provided in the following sections. The main motivation of this study is to quantize the complementary role of LiFi to RF communications. WiFi is chosen as the RF communication because:

- (i) based on [CommScope, 2018], an estimated 80% of mobile traffic originates and terminates from/to indoors, and
- (ii) WiFi plays a central role in the provision of indoor connectivity [CommScope, 2018].

The central role of WiFi is also supported by reports published in [Cisco, 2020]. It is predicted that:

- (i) by 2022, 59% of global mobile data traffic (cellular) will be offloaded to WiFi, which is up from 54% in 2017, and
- (ii) by 2022, 51% of total IP traffic will originate from WiFi, which is up from 43% in 2017.

Therefore, this chapter seeks to answer how much LiFi can help WiFi.

In this chapter, contributions and related works of this chapter are presented in the following sections. Detailed problem formulation regarding the offloading efficiency is discussed in Section 5.4. Scenarios under evaluation are described in Section 5.5. Traffic models based on

which the offloading efficiency is calculated are elaborated in Section 5.6. Section 5.7 discussed an abstraction of the PHY layer processing block to enable large network emulations. Finally, the offloading efficiency results are presented in Section 5.8. A summary of this chapter is provided in the last section.

5.2 Contributions of This Chapter

The main contribution of this topic is to use the results from the previous chapters in order to calculate the offloading efficiency. It means that the offloading efficiency is evaluated by using realistic assumptions, e.g., random mobility of users, random orientation of mobile devices, and random blockages. Having a realistic assumption is also the primary motivation to use the common mode PHY of IEEE 802.11bb. One of key novelty in this chapter is the use of real TCP/IP stack to evaluate large networks to calculate the offloading efficiency. Next section discusses related works with regards to the offloading capability of LiFi in hybrid WiFi and LiFi networks.

5.3 Related Works

The latest survey paper of hybrid WiFi-LiFi systems can be found in [Wu *et al.*, 2020]. Extensive effort has been devoted to study the load balancing issues in hybrid WiFi and LiFi networks, see [Li *et al.*, 2015; Y. Wang & Haas, 2015; Ma & Zhang, 2018; Obeed *et al.*, 2018]. The main motivation of these studies is similar. In indoor environments, coverage areas of WiFi and LiFi overlap. WiFi typically has a wider coverage area. Therefore, in hybrid WiFi-LiFi networks, WiFi might carry all mobile traffic as LiFi is vulnerable to blocking objects. Meanwhile, based on [Stefan *et al.*, 2013], LiFi has a higher area spectral efficiency. Therefore, LiFi can potentially help to offload the data traffic from WiFi when LiFi signals are sufficiently strong. The goals of load balancing algorithms vary from optimizing the resource allocation, maximizing the throughput, or minimizing network congestion. Different assumptions, such as mobile or static users and the existence of blocking objects, are also considered.

The studies above are all theoretical. Several other studies focus on the practical implementation of hybrid WiFi-LiFi systems, e.g., [Shao *et al.*, 2014; Alshaer & Haas, 2016; Liu *et al.*, 2018; Haas *et al.*, 2020]. Studies in [Shao *et al.*, 2014; Alshaer & Haas, 2016; Haas *et al.*, 2020]

use the SDN paradigm, where control and data planes are decoupled. Meanwhile, MPTCP is used in [Liu *et al.*, 2018] to enable multi-connectivity to both WiFi and LiFi networks simultaneously.

The approach taken in this chapter is in between theoretical and practical approaches. That is, the scalability advantage of the theoretical approach in terms of the number of APs and STAs is maintained. Also, the accuracy advantage of the practical approach is emulated by means of Linux namespaces¹. By using the Linux namespaces, multiple independent instances can be generated, and each instance has full access to the Linux filesystems, such as access to the TCP/IP stack and other Linux utilities, e.g., `hostapd` and `dhcpd`, which are used to emulate APs. The wireless channel is emulated by a Linux simulation tool called `wmediumd`², which can simulate a packet error rate and a transmission delay. The PHY layer is abstracted by means of a link-to-system mapping [Brueninghaus *et al.*, 2005]. This approach is similar to that of Mininet-WiFi³. In this chapter, the Mininet-WiFi will be extended to include LiFi and `owcsimpy` by adding the PHY layer abstraction of LiFi and modifying `wmediumd`. With these additional features, the Mininet-WiFi is re-branded as Mininet-LiFi. This emulation approach enables the use of MPTCP for multi-connectivity of WiFi and LiFi networks, horizontal handovers, and accessing real servers over the Internet. To the best of the author’s knowledge, a similar approach has not been done before, and Mininet-LiFi can be used as a platform to answer the question raised in Section 5.1.

Other than MPTCP, there are a few other multi-connectivity technologies, such as fast session transfer (FST), which is used in the IEEE 802.11ad (millimeter wave) [IEEE P802.11 TGad, 2012]. FST is used when the 60 GHz link is disrupted, for example, due to a blockage event. In that case, on-going communications are migrated to the 2.4 GHz or 5 GHz band. However, the negotiation causes the on-going data transfer to be held temporarily. Hence, FST does not support a seamless handover. Another downside of FST that is related to the study in this chapter is that FST is a MAC layer feature, which is implemented in a hardware. This adds another complexity for the emulation approach in this chapter. There are other multi-connectivity technologies other than MPTCP and FST, such as multipath virtual private network (VPN). However, MPTCP will be used in this chapter mainly due to the recommendation that was already made by the 3rd generation partnership project (3GPP) in [3GPP, 2020]. More details on

¹<http://man7.org/linux/man-pages/man7/namespaces.7.html>

²<https://github.com/bcopeland/wmediumd>

³<https://github.com/intrig-unicamp/mininet-wifi>

this will be discussed next.

5.4 Problem Formulation

Before detailing the question in Section 5.1, a future scenario will be described. In the future, mobile devices are predicted to support a multi-connectivity feature, see visions of 6G in [Saad *et al.*, 2019; Giordani *et al.*, 2020]. In the recent release (release 16) of the 3GPP architecture [3GPP, 2020], a 5G core network is envisioned to be connected with an untrusted non-3GPP access network via a non-3GPP interworking function. WiFi and LiFi can be parts of the untrusted non-3GPP access network. A functionality called access traffic steering, switching and splitting (ATSSS) is also standardized in the same release. The ATSSS allows a concurrent use of different access technologies (wired and wireless) to support seamless handover and data aggregation. An implementation of the ATSSS is MPTCP [Tessares, 2019]. Therefore, a mobile device in this chapter is assumed to be MPTCP-enabled. It is worth noting here that there is already a commercial mobile device that supports MPTCP, e.g., Apple iPhones with iOS 7 and above [Apple, 2017].

The contribution of LiFi is measured by a metric called an *offloading efficiency* [Lee *et al.*, 2013], which is defined as:

$$\text{offloading efficiency} = \frac{\text{the total bytes transmitted through LiFi}}{\text{the total bytes generated}}.$$

Furthermore, only mobile data traffic is emulated in this chapter. In addition, only on-the-spot offloading is considered here due to the nature of MPTCP that supports multi-connectivity and seamless handover between wireless access technologies. Another offloading is the delayed offloading [Lee *et al.*, 2013], which is not considered in this thesis because of the use of PHY IEEE 802.11bb, which adopts that of IEEE 802.11ax. Therefore, from the point of view of carriers, the users utilize the WiFi technology, and the users will not be charged with additional cost from cellular operators. It is stated in [Lee *et al.*, 2013] that this extra cost typically motivates users to choose the delayed offloading.

Lastly, the size of bytes that are measured is obtained by probing the TCP segment's data field. Then, the portion of data that goes through a LiFi channel can be differentiated from the source IP address that binds the LiFi interface. Note that we do not distinguish segments that need to be retransmitted due to congestions. In addition, only TCP traffic is measured in this thesis

since it represents 85% of the total Internet traffic [McCreary, 2020].

5.5 Channel Model

5.5.1 Scenario

In this chapter, the scenarios will be based on the descriptions specified in TGax [Merlin *et al.*, 2015]. This is because many organizations within the task group have agreed on scenarios defined in [Merlin *et al.*, 2015], and they can be easily adopted with additional LiFi APs. Note that TGbb also publishes many reference channel models for LiFi in [Uysal *et al.*, 2018], but it is difficult to include WiFi APs as the scenarios in [Uysal *et al.*, 2018] only consider an indoor room. Meanwhile, scenarios in [Merlin *et al.*, 2015] consider multiple rooms in a building.

In this chapter, two scenarios from TGax described in [Merlin *et al.*, 2015] are adopted, namely the residential and the enterprise scenarios. In the residential scenario, a five-story building with 2×10 apartments on each floor, and each apartment's dimensions are $10 \text{ m} \times 10 \text{ m} \times 3 \text{ m}$ is assumed. While in the enterprise scenario, eight offices with the dimensions are $20 \text{ m} \times 20 \text{ m} \times 3 \text{ m}$ per office are assumed. Figure 5.1 shows the illustrations of both scenarios.

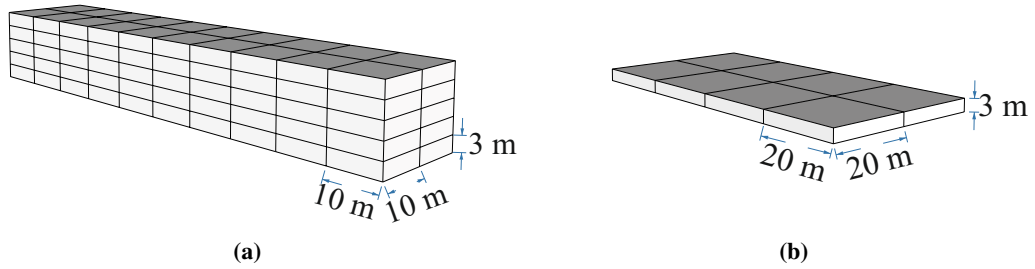


Figure 5.1. (a) The residential scenario: a five-story building with 2×10 apartments in each floor, and the dimensions of each apartment are $10 \text{ m} \times 10 \text{ m} \times 3 \text{ m}$. (b) The enterprise scenario that comprises 8 offices whose dimensions are $20 \text{ m} \times 20 \text{ m} \times 3 \text{ m}$ per office.

Based on the TGax document [Merlin *et al.*, 2015], the number of APs is fixed, i.e., one AP in an apartment in the residential scenario and four APs in an office in the enterprise scenario. In addition, the APs are randomly located within a room located in the residential scenario, while they are fixed in an office in the enterprise scenario. All STAs are assumed to employ both the IEEE 802.11ax and the IEEE 802.11bb. In this chapter, the number and locations of STAs are varied in order to incorporate random orientations, mobility, and blockage. Objects in the rooms are randomly generated. For example, realizations of an apartment and an office

are shown in Figure 5.2. Both realizations illustrate a uniform placement of APs and random generation of human models with different activities while using their mobile devices.

The number of people in the small room in the residential scenario is modeled as a Bernoulli distribution. In the living room, the number of people follows the Poisson distribution with a mean of 3. The activity of each person is modeled as a uniform distribution over a feasible set of options. If a realization is not feasible, then a rejection sampling is used. The location of each person also follows a uniform distribution over a set of feasible locations. For the enterprise scenario, people are modeled at each desk and this follows the Bernoulli distribution. The number of people who stand in an office room follows the Poisson distribution with a mean of 5.

5.5.2 WiFi Channel Model

The channel model of WiFi follows [Merlin *et al.*, 2015]. The transmit power of an STA is assumed to be 15 dBm per antenna. The transmit power of an AP is 20 dBm per antenna. The noise figure is 7 dB. When the 2.4 GHz band is used, 20 MHz channels are assumed, and the carrier frequency is 2.4 GHz. Meanwhile, when the 5 GHz band is used, 80 MHz channels are considered, and the carrier frequency is 5 GHz.

The pathloss model for the residential scenario is [Merlin *et al.*, 2015]:

$$P_L(d, f_c) = 40.05 + 20 \log_{10}(f_c/2.4 \text{ GHz}) + 20 \log_{10}(\min(d, 5)) + \mathbb{1}(d > 5)35 \log_{10}(d/5) + 18.3F^{\frac{(F+2)}{(F+1)} - 0.46} + 5W + 5Hf_c/2.4 \text{ GHz}, \quad (5.1)$$

where d is max(the Euclidean distance, 1) in m, f_c is the carrier frequency, F is the number of floors traversed, W is the number of wall traversed, and H is the number of humans traversed. The term $5Hf_c/2.4 \text{ GHz}$ is added to replace the log-normal shadowing model in [Merlin *et al.*, 2015]. Also, it is added to provide a fair comparison with the LiFi channel. It provides a fair comparison as both WiFi and LiFi channel models share the same human models, e.g., the number of human models and their direction in the room. The 5 dB attenuation is based on the measurements that are reported in [Januszkiewicz, 2018]. The pathloss model for the enterprise

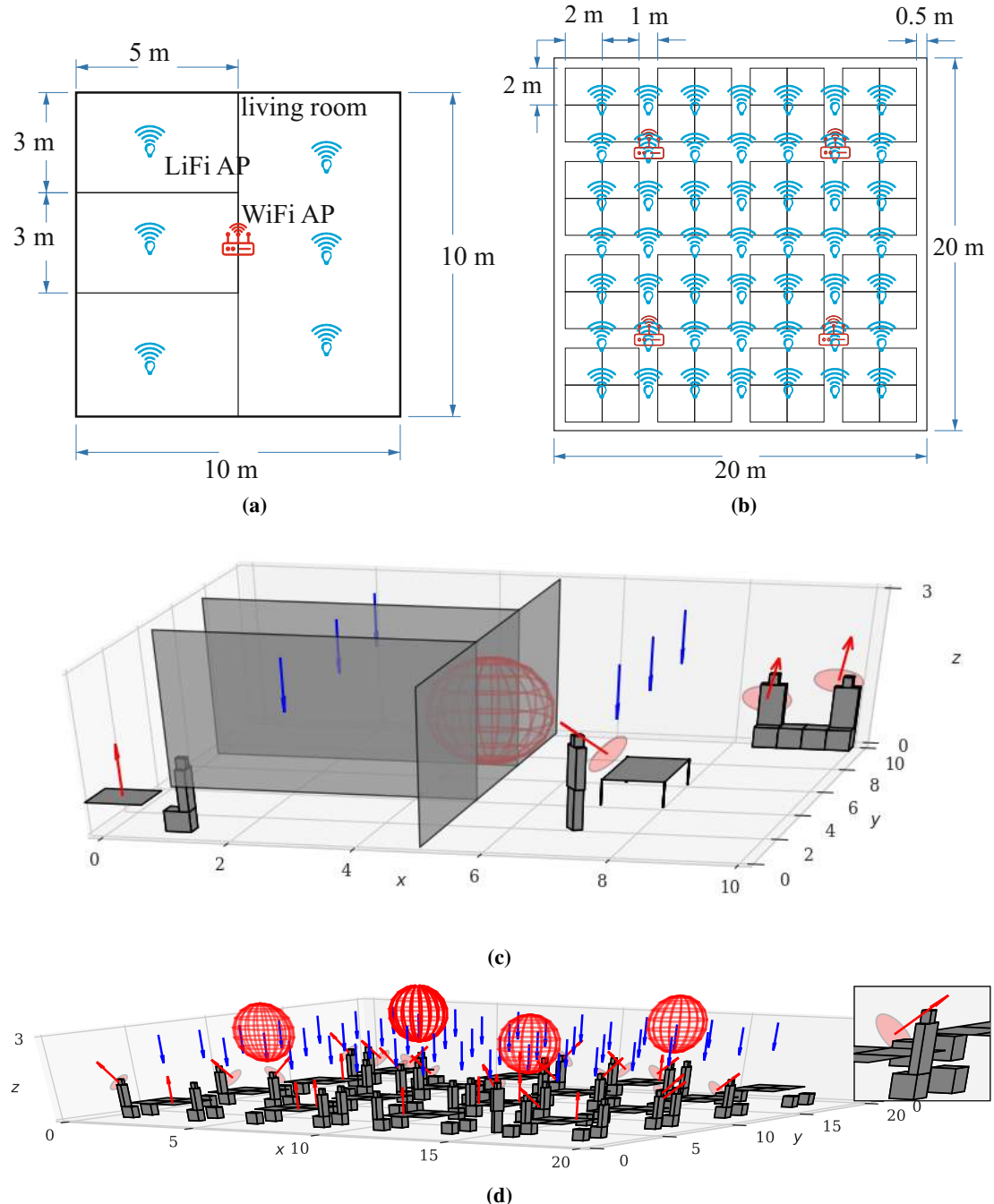


Figure 5.2. (a) A floor plan of a realization of the interior of an apartment in the residential scenario. (b)) A floor plan of a realization of the interior of an office in the enterprise scenario. (c) The 3D realization of the apartment using `owcsimpy`. (d) The 3D realization of the office using `owcsimpy`.

scenario is [Merlin *et al.*, 2015]:

$$P_L(d, f_c) = 40.05 + 20 \log_{10}(f_c/2.4 \text{ GHz}) + 20 \log_{10}(\min(d, 10)) + \\ \mathbb{1}(d > 10)35 \log_{10}(d/10) + 7W + 5H f_c/2.4 \text{ GHz}, \quad (5.2)$$

where the effects of the number of floors traversed are not included.

5.5.3 LiFi Channel Model

The LiFi channel model is implemented by using `owcsimpy`, which has been discussed extensively in Chapter 2 and Appendix A. The transmit power of the STA follows the linear region of the light emitter, which is from 25 mW (approximately 14 dBm) to 30 mW (approximately 15 dBm). The orientation model of STAs follows the RP model discussed in Chapter 3.

It is assumed that the output waveform of PHY is at the 5 GHz band due to the high performance and the small coverage nature of LiFi. As the bandwidth is 80 MHz, then all LiFi APs use the channel number 36, 40, 44, and 48 [IEEE P802.11 TGax, 2018]. Based on [Tsonev *et al.*, 2017], the PSD of the white noise is set to be $6.19 \times 10^{-14} \text{ V}^2/\text{Hz}$.

5.6 Traffic Model

A conventional way to model traffic in a system-level simulation is by generating an artificial application layer data that follows a certain traffic model. For example, TGbb that follows the traffic model of IEEE 802.11 High Efficiency - Task Group “ax” (TGax) as specified in the methodology document [Porat *et al.*, 2016] defines a web browsing or hypertext transfer protocol (HTTP) traffic model. The document uses the ON-OFF model which was initially introduced in [Deng, 1996]. The ON state models a situation where a user requests a hypertext markup language (HTML) page, while the OFF state models the reading time of a user. During a request or in the ON state, various sizes of packets are received by a user. These different sizes denote the different sizes of content that is being requested within an HTML page that contains, for example, images, advertisements, JavaScript scripts, etc. The empirical model of web traffic is detailed in [Porat *et al.*, 2016]. However, this model was measured by using the HTTP 1.0/1.1, while currently most browsers already add HTTP/2 [Deveri, 2020a] and HTTP/3 [Deveri, 2020b]. In addition, the model describes an object size following a truncated

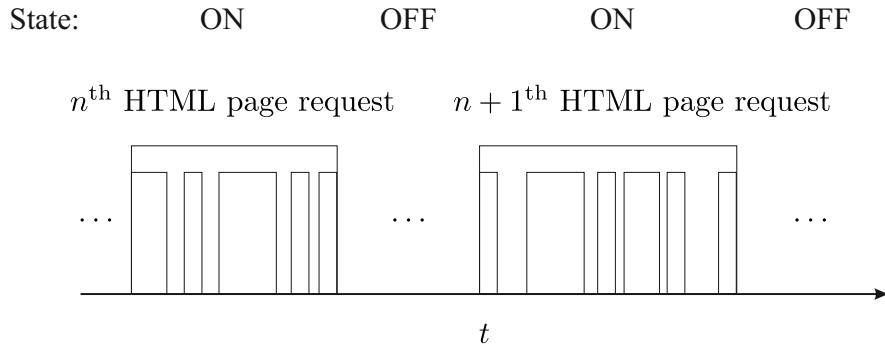


Figure 5.3. The ON-OFF model for modeling the web traffic.

Log-normal distribution with fixed parameters. The contents of the current HTML pages are probably richer, e.g., they contain embedded videos, higher-resolution images, etc. Therefore, the model might not be valid. The same justification also applies to other traffic models, such as the file transfer protocol (FTP), video streaming, and game traffic models. Hence, in this thesis, we take a slightly different approach.

Owing to the Linux namespaces, instead of using all model descriptions in [Porat *et al.*, 2016], we can emulate some parts and use the model for the rest. This emulation method is depicted in Figure 5.4. Given a scenario, e.g., a residential or an enterprise scenario, the WiFi and LiFi networks at each room are emulated by Mininet–LiFi. This Mininet–LiFi is then connected to a network interface card (NIC), e.g., an ethernet card or a WiFi card interfaces. Using this method, all instances of the Linux namespaces can access the Internet. Therefore, with this method, we might not need to use the traffic models defined in [Porat *et al.*, 2016]. In order to determine a file size of an HTML page, the top 50 websites in the Alexa list [Alexa, 2020] are picked randomly. A geometric distribution with a mean of 2 is used. The top 50 websites in the Alexa list contain search engines, video streaming, social networking, discussion, and e-commerce websites. For the search engines, another top 50 most searched keywords can be used based on, for example, Google Trend data⁴. The duration of the OFF states for each traffic is determined based on the description that is defined in [Porat *et al.*, 2016]. For example, the reading time for the web traffic follows an exponential distribution with a mean of 30 s. Then, a Bernoulli trial with the success probability of 0.5 is used to determine if a user requests another additional content from the same server or other servers. The reason for this choice is that it has not been defined in the methodology document. However, in the future, details on simulating

⁴<https://trends.google.com/trends/>

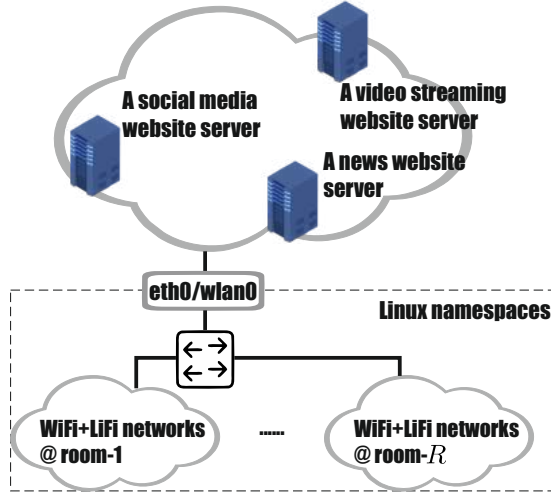


Figure 5.4. A description to emulate traffic models.

a mix of traffic in the document can include users' behavior, such as a dwell time as studied in [Liu *et al.*, 2010], which is outside the scope of this thesis. The mean reading time of 30 s and the success probability of 0.5 are only used for traffic other than those coming from video streaming website servers. The exception will be defined next.

It is worth mentioning here that this emulation method is straightforward. The main challenge comes from scenarios where a user requests a content from a video streaming website server, such as YouTube™. The reason for this is that the access to the servers is emulated by means of scripts or command-line interfaces (CLIs), such as `curl`⁵, which supports many protocols, e.g., HTTP, FTP, real-time streaming protocol (RTSP), etc. However, modern video streaming servers including YouTube™ run dynamic adaptive streaming over HTTP (DASH), where the quality of video can be adaptively changed depending on the bandwidth of users. To the best of the author's knowledge, there is no tool that can near-realistically emulate such traffic. Therefore, instead of streaming the contents, open source tools such as `youtube-dl`⁶ and `youtube-upload`⁷ are used to download them. In this case, we set a success probability of 0.8. Using this method, we can roughly emulate the scenario where a user transitions between different videos. These numbers reflect the experimental result reported in [Liu *et al.*, 2010] which states that a user tends to dwell in, for example, an entertainment website compared to news or an educational website.

⁵<https://curl.haxx.se/>

⁶<https://github.com/ytdl-org/youtube-dl>

⁷<https://github.com/tokland/youtube-upload/>

5.7 Link-to-System Mapping

As we will emulate large networks depicted in Figure 5.4, simulating full physical layer blocks is time-consuming and computationally expensive. Hence, the physical layer needs to be abstracted. One of the approaches is link-to-system mapping [Brueninghaus *et al.*, 2005]. The main goal of link-to-system mapping is to predict the instantaneous link performance of OFDM systems. To be specific, the role of a PHY abstraction method is to predict the coded PER for a given received channel realization. In order to predict the coded PER, the post-processing SINR values (after equalization and before a forward error correction decoder) are used as the input to the PHY abstraction mapping. The link-level PER is predicted by calculating an effective SINR, SINR_{eff} , which is a function of all post-processing SINR values. This mapping process is termed as ESM. The ESM PHY abstraction compresses the vector of received SINR values of all sub-carriers to a single effective SINR value, which can then be further mapped to a PER. Based on the PER, a Bernoulli trial is carried out to determine if a packet is dropped or not. This link-to-system mapping procedure is described in Figure 5.5.

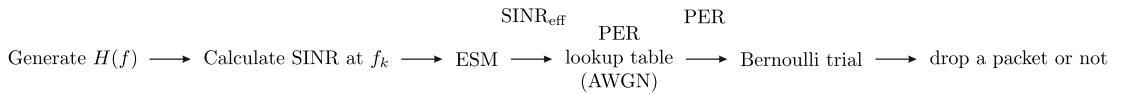


Figure 5.5. The PHY link-to-system mapping work flow.

Up to this point, some of the steps have been explained. For example, the channels $H(f)$ are generated using `owcsimpy`. The SINR per sub-carrier f_n can be obtained by using two methods. The first one is that we can use the output of the equalizer in the PHY layer blocks of IEEE 802.11ax, which is still relatively quick compared to the running time of a low-density parity-check (LDPC) decoder. The second method is by using the following relationship. Suppose $x(t)$ is a random signal that is filtered by a linear time-invariant (LTI) filter having a frequency response $H(f)$, then the PSD of the output denoted by $P_y(f)$ is:

$$P_y(f) = |H(f)|^2 P_x(f),$$

where $P_x(f)$ is the PSD of $x(t)$. In this thesis, the former method is used. The PER lookup table over AWGN channels is available in the appendix of [Porat *et al.*, 2016]. This lookup table is stored in the `wmediummd`. Similarly, the Bernoulli trial is also carried in the `wmediummd`. The rest of this section discusses the ESM for TGbb. Note that the ESM for TGax has been available on [Porat *et al.*, 2016].

In general, the ESM function can be defined as:

$$\text{SINR}_{\text{eff}} = \alpha_1 f^{-1} \left(\frac{1}{K} \sum_{k=1}^K f(\text{SINR}_n / \alpha_2) \right), \quad (5.3)$$

where SINR_n denotes the SINR at n^{th} sub-carrier, f is an invertible function, α_1 and α_2 are two fitting parameters to be determined later. There are several types of ESM, but there are two types that are mostly used, i.e., exponential effective SINR metric (EESM) [3GPP TR 25.892, 2004; Ericsson, 2003] and mutual information effective SINR metric (MIESM) [Jung-Fu Cheng, 2004]. In this thesis, the MIESM will be used based on [Brueninghaus *et al.*, 2005]. Based on [Jung-Fu Cheng, 2004], the mapping function for M -quadrature amplitude modulation (QAM) with $\alpha_1 = \alpha_2 = \beta$ is defined as:

$$f(\text{SINR}_n; M) = \log_2 M - \frac{1}{M} \sum_{m=1}^M \mathbb{E}_U \left(\log_2 \left(1 + \sum_{k=1, k \neq m}^M \exp \left(- \frac{|X_k - X_m + U|^2 - |U|^2}{\beta / \text{SINR}_n} \right) \right) \right),$$

where U is zero mean complex Gaussian with variance $1/(2\text{SINR}_n)$ per component, and X_m and X_k are the M -QAM constellation symbols. Then, SINR_{eff} can be calculated as:

$$\text{SINR}_{\text{eff}}(\beta) = \beta f^{-1} \left(\frac{1}{N} \sum_{n=1}^N f(\text{SINR}_n / \beta; M); M \right).$$

Given a lookup table (LUT) of PERs calculated on AWGN channels for each modulation and coding scheme (MCS), then an expected PER, denoted by PER_{E} , is defined as:

$$\text{PER}_{\text{E}}(\beta) = \text{PER}_{\text{LUT}}(\text{SINR}_{\text{eff}}(\beta); \text{MCS}).$$

A measured PER is denoted by PER_{M} . Then, the optimized β is determined as follows:

$$\beta^* = \arg \min_{\beta} \sum_{c=1}^C |\text{PER}_{\text{E},c}(\beta) - \text{PER}_{\text{M},c}|^2, \quad (5.4)$$

where c denotes the c^{th} channel realization.

An exhaustive search is carried out for each scenario. Twenty thousand packets are generated for each channel realization with a packet length of 1,458 bytes [Porat *et al.*, 2016]. The PHY

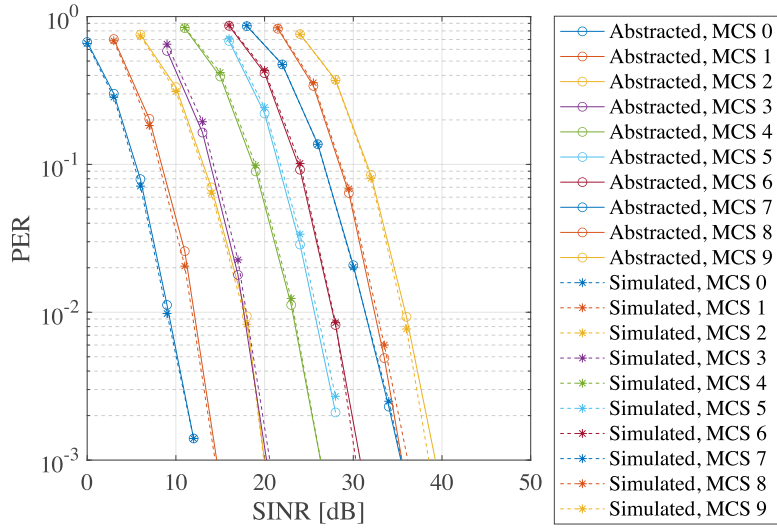


Figure 5.6. Link level simulations for the residential scenario: simulated vs. abstracted. Note that the abstraction scenario refers to the use of the ESM function.

of IEEE 802.11ax supports two FECs. In this thesis, we assume the LDPC instead of the binary convolutional codes due to the performance. The comparisons between the simulated and the abstracted link-level simulations with $B = 20$ MHz can be seen in Figure 5.6 and Figure 5.7. The optimal parameters are $\beta^* = 1.13$ and $\beta^* = 1.07$ for the residential and enterprise scenarios, respectively. With these results, we should become confident that the PHY abstraction is sufficiently accurate.

Now, the question is ‘what if a packet has a length greater than 1,458 bytes? If that is the case, how we decide whether the packet is dropped or not.’ In this case, the packet is partitioned into multiple of 1,458 bytes, say K . Note that the maximum length of MAC protocol data unit (MPDU) is 11,454 bytes. Then, the PER is calculated for each partition. Based on [Porat *et al.*, 2016], the packet is removed if there is at least a partition that is dropped based on a Bernoulli trial applied to the corresponding partition. In the next subsection, we are ready to address the question about the contribution of LiFi in hybrid WiFi and LiFi networks.

5.8 Performance Evaluation

A realization in the residential scenario is shown in Figure 5.8(a). It is assumed that the mobile user moves according to the RWP while reading on the mobile device. The mobile user’s traffic is made deterministic in this case, such that the mobile user downloads a large file while mov-

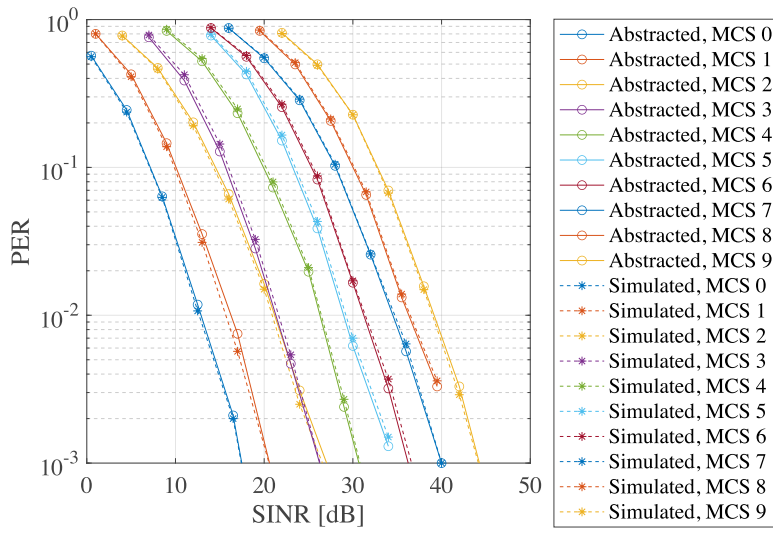


Figure 5.7. Link level simulations for the enterprise scenario: simulated vs. abstracted. Note that the abstraction scenario refers to the use of the ESM function.

ing. The reason for this is to show the simultaneous connectivity of MPTCP. The corresponding data rate is shown in Figure 5.8(b). Notice that at around 5 s, the LiFi link is disconnected due to self blockage. Another observation that can be drawn from Figure 5.8(b) is that while connected to a LiFi AP, the data rate of the LiFi interface is most likely higher than that of the WiFi interface. Lastly, it should be noted here that in order to emulate hundreds of Mbps connections, the emulation is carried out in compute instances of cloud providers that support up to 25 Gbps network bandwidth, for example, the Amazon elastic compute cloud.

Figure 5.9 shows heatmaps of the average data rate for all scenarios and networks. Unlike the previous specific result, the results are taken by averaging many samples that are generated from different traffics and user movements. Following the description in Chapter 3, three random mobility models are assumed, i.e., random waypoint [Johnson & Maltz, 1996], random direction [Royer *et al.*, 2001], the truncated Levy-walk model [Hong *et al.*, 2008]. Note that the blank spots show the infeasible region where the user never moves to the spots, which corresponds to the locations of solid objects, e.g., desks, chairs, and walls. The small spots correspond to the data rates that are measured when the users are sitting. From these figures, a ‘spatial coverage’ of each network can be estimated. Fitting the samples with the multivariate Gaussian mixture distributions gives the standard deviation of around 1.2 m for LiFi networks, and 6.3 m for WiFi networks. These results lead to the offloading efficiency as shown in Figure 5.10. The offloading efficiency means are 64.54% and 75.85% for the residential and enterprise scenarios,

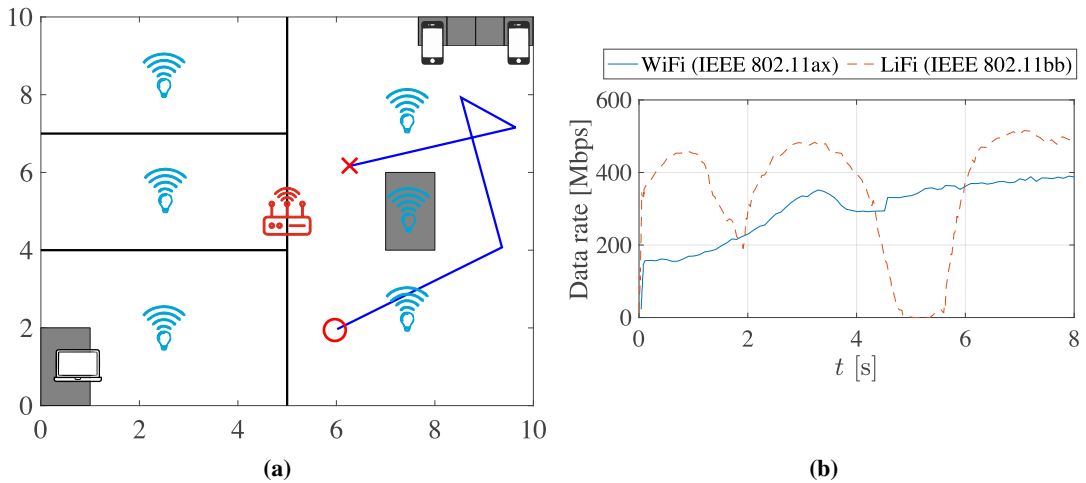


Figure 5.8. (a) A sample of realizations in the residential scenario, where the legends of the mobility of the user follows those of Figure 3.12 and Figure 5.2. The laptop and phone icons show the existence of other users in the sample. (b) The measured data rate of the mobile user.

respectively. Higher efficiency is obtained in the enterprise scenario due to the higher density of LiFi APs. These efficiencies show that out of 59% of the global mobile traffic that will be offloaded to WiFi based on [Cisco, 2020], up to 75% can be carried to LiFi. Therefore, LiFi is a strong candidate to complement WiFi in the near future.

5.9 Summary

In this last technical chapter of this thesis, results from the previous chapters, i.e., the frontend and channel models from Chapter 2, the random orientation model from Chapter 3, and the common mode PHY of IEEE 802.11bb from Chapter 4, are used to investigate the contribution of LiFi in hybrid WiFi and LiFi networks. To study the contribution of LiFi, hybrid WiFi and LiFi networks are emulated using Linux namespaces, where the TCP/IP stack can be used for real data communications. First, the PHY of IEEE 802.11bb is abstracted by means of link-to-system mapping. By using this abstraction, then given an SINR, the PER can be estimated and used to decide whether a packet is dropped or not. Then, real data traffic by accessing real website servers is also performed. The multi-connectivity of WiFi and LiFi interfaces is handled using MPTCP, which also supports seamless handover if one of the links is broken. Using this method, the hybrid WiFi and LiFi networks can be mimicked. In this chapter, we quantify the contribution of LiFi in hybrid networks by measuring the offloading efficiency, which is defined as the ratio of the number of bytes transferred over LiFi to the total number of

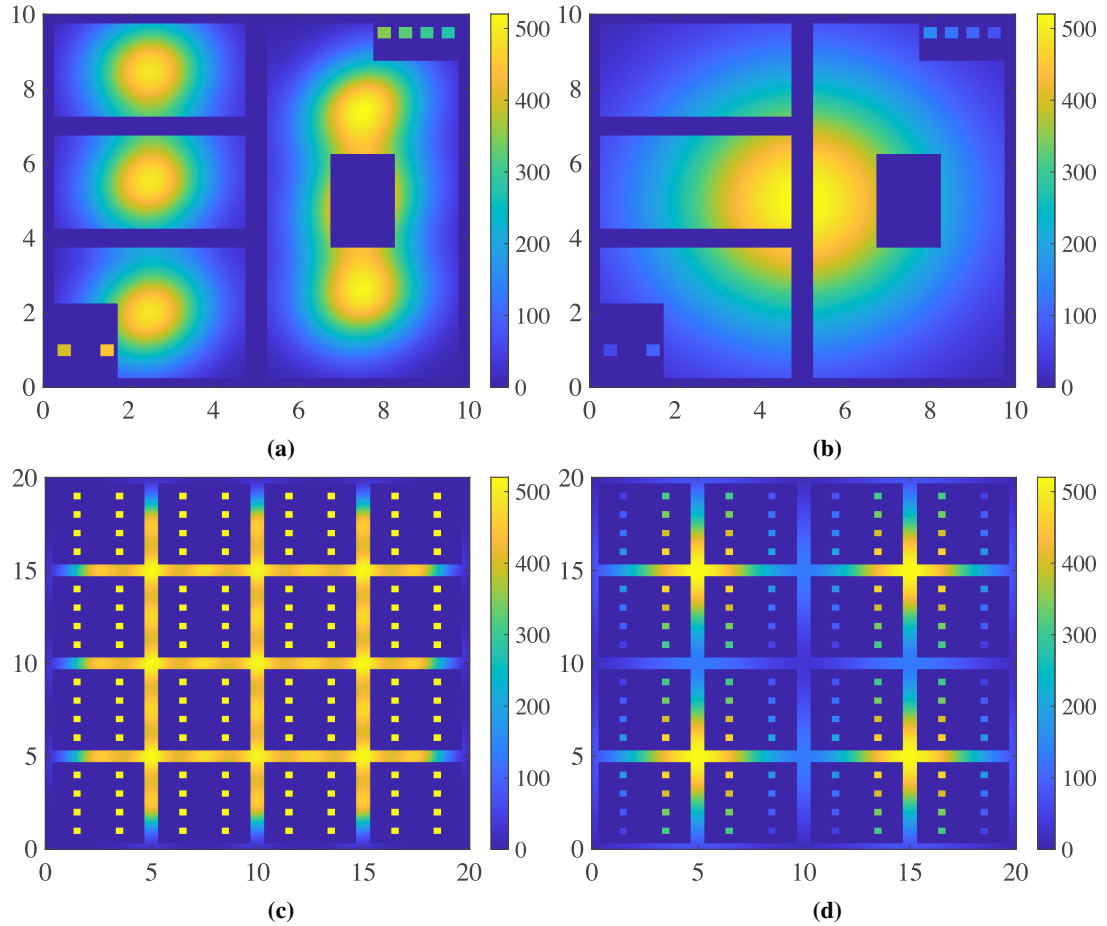


Figure 5.9. Average data rate (Mbps) in: (a) the residential scenario for the LiFi networks, (b) the residential scenario for the WiFi networks, (c) the enterprise scenario for the LiFi networks, and (d) the enterprise scenario for the WiFi networks.

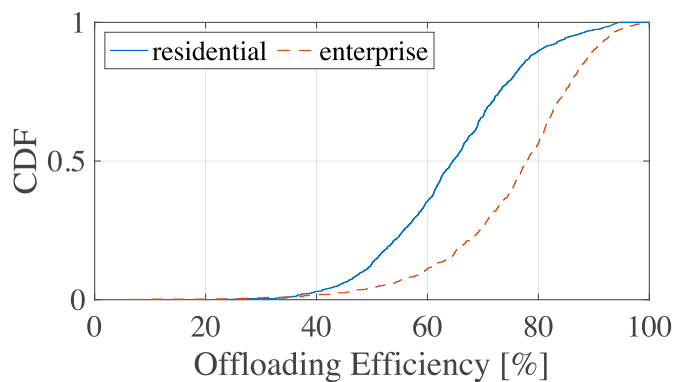


Figure 5.10. Offloading efficiency.

bytes. We conclude that the offloading efficiencies of 64.54% and 75.85% can be achieved for both residential and enterprise scenarios, respectively. These results show the benefit of LiFi to complement RF networks, e.g., WiFi, in the near future.

Chapter 6

Conclusions and Future Research

6.1 Conclusions

In this thesis, the offloading efficiency is used to measure the contribution of LiFi in hybrid WiFi and LiFi networks. In order to compute this metric, near-realistic channel models, i.e., random blockage and random orientation models, are needed. In addition, discussions on the LiFi modulation techniques that may be used in future are required. Therefore, the contributions of this thesis includes these near-realistic channel models, studies of LiFi modulation techniques, and calculating the offloading efficiency. To this end, this thesis is organized such that chapters are written based on the contributions.

In Chapter 2, in addition to the discussions of the LiFi system and channel models, one of the contribution of this thesis, i.e., `owcsimpy`, is introduced. The primary contribution of `owcsimpy` is that it can be used to easily generate random blocking objects. In `owcsimpy`, an arbitrary 3D object is modeled as a collection of 2D faces, and each face holds a few attributes, such as its Lambertian propagation mode, FoV, location, normal vector, and surface area. In addition, `owcsimpy` is designed to be lightweight and open (not commercially-licensed). Therefore, `owcsimpy` can be easily deployed in many virtual servers across different regions provided by a cloud provider. Consequently, generating thousands of CIRs becomes straightforward. One of the main advantages is that, for example, the offloading efficiency and the error performance of a LiFi modulation technique can be evaluated over many CIR realizations.

In Chapter 3, another contribution of this thesis is presented, i.e., a random orientation model of mobile devices. The random orientation model is obtained based on real measurements. It has been shown that the random orientation model resembles a harmonic RP. The random orientation model from Chapter 3 and the random blockage model from Chapter 2 can be combined with existing random mobility models, such as RWP or the truncated Levy-walk model. A combination of these models is incorporated to evaluate a coherence time of LiFi channel in indoor room scenarios. The coherence time is defined as a time interval over which a CIR does not change significantly. Therefore, knowing this value can be important, such as

in hybrid WiFi and LiFi networks employing the SDN paradigm. Specifically, the placement of LiFi APs can be located such that the delay and the latency between a LiFi AP and an SDN controller is less than the coherence time. The reason for this is to avoid an outdated rule from the SDN controller to the LiFi AP. In Chapter 3, it was shown that the coherence time of a LiFi channel in indoor room scenarios is most of the time greater than 40 ms, which is the average delay of an SDN rule from the time that it is generated until it can be applied in existing SDN-enabled switches. Therefore, system designers who are equipped with the knowledge of the coherence time can properly deploy LiFi APs in hybrid WiFi-LiFi networks in the real world.

In Chapter 4, both single-carrier and multi-carrier modulation techniques are investigated. PAM-SCFDE is used as a foundation for the single-carrier modulation. Improvements are carried out by adding non-linear filters, i.e., DFE and THP. In addition, IM is applied to PAM-SCFDE, which is referred to PAM-SCTIM. However, directly applying IM to PAM-SCFDE results in a sub-optimal performance. Then, a generalization of PAM-SCTIM is proposed by freeing the constraints of PAM-SCTIM. Regarding the multi-carrier modulation, it has been shown that the common mode PHY of IEEE 802.11bb suffers from the low-pass filter characteristic of the wireless optical channel, then IQ-WDM is proposed. Instead of applying frequency up-conversion, IQ-WDM transmits the baseband waveform over two different wavelengths. Comparisons of both single-carrier and multi-carrier modulation techniques are presented at the end of Chapter 4. Up to 3 dB gain is achieved by the improved versions of PAM-SCFDE in the low-to-moderate spectral efficiency region. In the high spectral efficiency region, 2 dB gain can be achieved by IQ-WDM with respect to the common mode PHY of IEEE 802.11bb.

In Chapter 5, the common mode PHY of IEEE 802.11bb is used to calculate the offloading efficiency. As the PHY layer of IEEE 802.11bb is assumed to follow that of IEEE 802.11ax, the current TCP/IP stack can be assumed to be compatible with the MAC and PHY layers of IEEE 802.11bb-based LiFi. Furthermore, MPTCP can be applied to emulate the multi-connectivity of both WiFi and LiFi networks. Seamless handover can also be applied by using MPTCP. Using a real TCP/IP stack can enable us to access many websites without directly modeling the traffic. However, emulating such big networks is computationally expensive. Therefore, the PHY layer needs to be abstracted by means of link-to-system mapping. By using this approach and generating many samples, it has been found that the offloading efficiency can reach up to 64.54% and 75.85% for residential and enterprise scenarios, respectively. Having these numbers means that LiFi can potentially unburden WiFi, which will be predicted to handle

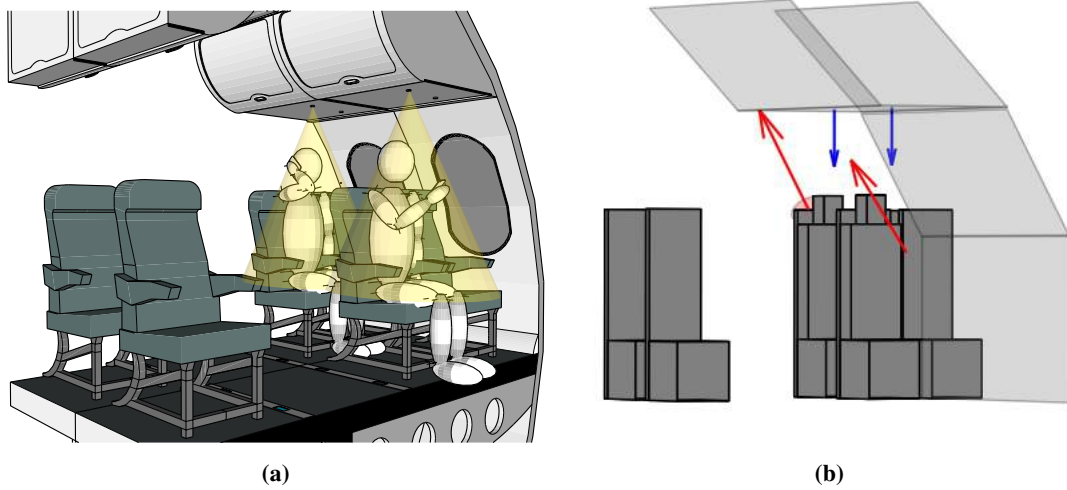


Figure 6.1. An aircraft cabin model that can be modeled by `owcsimpy`.

more than 50% of the total mobile traffic by 2022. Hence, LiFi is a powerful candidate to complement WiFi in the future.

6.2 Future Research

The following discusses the thesis' limitations, as well as its limitations and how to resolve these.

- `owcsimpy`

As the backend of `owcsimpy` currently depends on the deterministic approach, which only supports the diffuse reflection, then `owcsimpy` can be improved by implementing the ray-tracing method that can consider specular reflections. In addition, other than indoor scenarios, the front-end modules of `owcsimpy` can also be used to model objects in an aircraft cabin as depicted in Figure 6.1. Studies that need a dataset of images that are captured by CCTVs can be simulated with the help of `owcsimpy`. An example of such a scenario is fusion-based indoor positioning systems [Guo *et al.*, 2020] when WiFi, LiFi, and CCTVs are used. Figure 6.2 shows an example of the emulated images from the enterprise scenario. Such blocky objects can be thought of as outputs of object-recognition softwares.

- Random orientation model

A more accurate random orientation model is a model that can capture the dependency

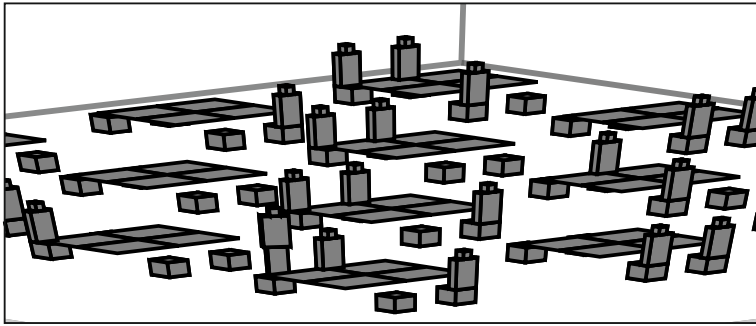


Figure 6.2. The emulated image that is captured by one of the CCTVs.

of the orientation of a mobile device and the mobility pattern of a user. In reality, this random behavior also depends on the locations of APs as well as the traffic size being requested. For example, in order to provide high quality content, a content creator requires a reliable Internet connection. One way to ensure such a connection is to have the creator move close to an AP, e.g., a LiFi AP. In order to capture all these dependencies, LiFi APs need to be widely deployed in many premises to conduct a large-scale experiment. A smaller-scale, controlled experiment can also be conducted. However, LiFi APs are still required.

- Modulation systems

As PAM-SCFDE has been improved by enhancing the linear equalizer with non-linear equalizers as well as optimizing the codebook, the next natural extension is to upgrade the pulse shaping. Pulse shaping can also be used to shift the center frequency of the common-mode PHY of IEEE 802.11bb. Recall that, based on the discussions in [Purwita & Haas, 2020b; Purwita, Haas, Serafimovski, Afgani, *et al.*, 2020; Purwita, Haas, Serafimovski, & Berner, 2020; Rossius *et al.*, 2020; Serafimovski *et al.*, 2020], the main cause of the center frequency being far from DC is because of the use of a spectrum mask in order to find the optimal center frequency. There is a high-end WiFi chipset, for example from Qualcomm as discussed in [Purwita, Haas, Serafimovski, & Berner, 2020], that has a narrower spectrum compared to the spectrum mask, then analog pulse shaping can be used to improve the waveform of the common-mode PHY.

- Hybrid WiFi-LiFi: Determining the LiFi Offloading Capability

The metric offloading efficiency has been widely adopted as it is very intuitive and straightforward, see [Lee *et al.*, 2013] and references therein. Other than the offload-

ing efficiency, other metrics such as offloading overhead, quality of experience, or power saving can be also considered [Rebecchi *et al.*, 2015]. In addition, the offloading efficiency is calculated based on today’s IP-based networks, which are also known as ‘best-effort’ networks. This assumption might not be true in the future due to, for example, 5G use cases, i.e., enhanced mobile-broadband, massive machine-type communications, and ultra-reliable and low latency. Therefore, the current emulation method can be extended to include LiFi-enabled internet-of-things devices. Furthermore, the single-carrier modulation systems, which are power-efficient, can be used. Once these use cases can be emulated, machine learning algorithms and the SDN paradigm can be integrated to emulate autonomous traffic management with the current setup.

Appendix A

owcsimpy: A Library for Generating Wireless Optical CIRs

A.1 Introduction

A popular software to generate wireless optical CIRs is Zemax® [Zemax, 2020]. The main disadvantage of Zemax® is that it is not portable due to its commercial license. This portability is important in the case where many samples of CIRs need to be generated as in Chapter 3. Relying only on several Zemax®-installed machines to generate many samples is time-consuming. Other available softwares can be found in [Carruthers & Kannan, 2002a; Rahaim, 2018]. Both of them are written in MATLAB®, which is also commercially licensed. The other limitation is boxes or planes in [Carruthers & Kannan, 2002a; Rahaim, 2018] can only be defined such that they point to either *x*-or-*y*-axes, see [Carruthers & Kannan, 2002b, Figs 1 and 10]. This can be problematic if a mobile user is assumed to be able to move in arbitrary directions on the *x*-and-*y* plane. In addition, only the time-domain approach based on [Carruthers & Kannan, 2002b] is implemented.

owcsimpy is an open-source, lightweight library to generate CIRs. One of the advantages of owcsimpy is that it can be easily deployed in many cloud computing instances of infrastructure as a service (IaaS), e.g., Amazon AWS, Microsoft Azure, or Google Cloud Platform. Diverse applications of owcsimpy range from modeling complex indoor scenarios, the study of LiFi channels (e.g., coherence time) with random mobility and random orientation assumptions, and the application of a machine learning to VLP with near-realistic scenarios. Near-realistic scenarios with random blockages by arbitrary 3D objects (such as human models or furniture) can be considered. Random mobility of users and randomly-oriented LiFi-enabled devices can also be incorporated.

In the next section, key features of owcsimpy are discussed. Then, the use of owcsimpy to generate some geometry models is presentend. The main purpose is to give an high-level introduction of how geometry models, such as human models, are generated.

A.2 Key Features of **owcsimpy**

Based on Section 2.2.2, we need the following features.

- f.1** (*creating 3D objects*) Various 3D objects, such as humans, furniture, or indoor rooms, are needed in order to have more realistic scenarios.
- f.2** (*partitioning*) Based on (2.6), summing up to N indicates the partitioning of a bigger object into smaller objects, which are denoted by the elemental objects ε_i as depicted in Figure 2.4(a). For example, any arbitrary 3D object can also be partitioned into many 2D planes or 3D meshes by means of, for example, the 3D Delaunay triangulation.
- f.3** (*attributing*) Based on (2.3) and (2.4), each partitioned object from **f.2** has a few attributes, such as the position and normal vectors, the mode number, the detection areas, etc, see Figure 2.4(b).
- f.4** (*geometric operations*) Based on (2.3), (2.4), and (2.7), basic geometric operations, such as calculating the Euclidean distance, irradiance and incidence angles, and checking if the LoS of two elemental objects is blocked (i.e., V_{ij}), are needed. In addition, a validation function is also needed in order to check the feasibility if two objects are intersecting to each other.
- f.5** (*CIR calculation*) Equations (2.5), (2.6), and (2.7), show the need of high-speed computations for the numerical-intense functions.

Inspired by web developments, the above features are implemented in either frontend and backend modules, see Figure A.1 for an illustration. Features that are better visible to users and less computationally intensive are implemented in the frontend. Examples of such features are **f.1**, **f.2**, and **f.3**. Therefore, users can: (i) decide the scenario-under-test (**f.1**), e.g., dimensions of a room, number of humans and furniture, etc.; (ii) set the attributes of objects (**f.3**), e.g., the mode number, the FoV, or wavelength-dependent reflectivities of reflecting surfaces (such as walls, floor, or ceiling); (iii) observe the partitioned objects (**f.2**). The outputs of the frontend are objects such as small 2D planes, LEDs, and PDs with their attributes. Then, based on these output objects, the features **f.4** and **f.5** are implemented in the backend.

In the current version of **owcsimpy**, i.e., v0.0.1, the frontend is implemented by using Python, which supports the object-oriented programming (OOP) by default. The use of OOP eases the

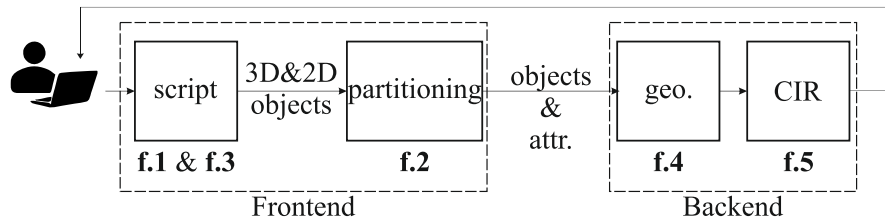


Figure A.1. Description of `owcsimpy` v0.0.1. Note: attr. is short for attributes, and geo. is short for geometry.

implementation of the frontend due to the fact that partitioned objects should inherit some of the attributes from their parent objects. Moreover, using Python also helps to extend the functionality of `owcsimpy`, for example, an integration with a machine learning library (which is dominated by Python), system-level simulators (e.g., ns-3 or mininet), and a 3D computer-aided design (CAD) (e.g., FreeCAD 3D or SketchUp). The frontend implementation of `owcsimpy` is shown in Figure A.2. Figure A.2(a) shows an example of applying the Delaunay triangulation to an arbitrary 3D object. Meanwhile, Figure A.2(b) shows a human model with blocky and pixelated objects that are already partitioned. These blocky and pixelated objects are inspired by Minecraft¹. The different transparency levels show that different parts of the human are covered with differential materials that have different reflectivities. In addition, the red and black arrows show the orientation of a mobile device and the direction the human is facing, respectively. Throughout the thesis, we assume blocky and pixelated objects as in Figure A.2(b) due to its low dependency to other libraries. The reason for this is that an early reason for the development of `owcsimpy` was due to the requirement of an efficiently generating many samples CIRs with different indoor scenarios. A lightweight approach helps the users to deploy `owcsimpy` in many computing instances of IaaS.

The backend of `owcsimpy` is implemented in a low-level programming language due to its computationally intensive requirement. `owcsimpy` uses C with additional libraries such as OpenMP (for multi-threading), BLAS, and LAPACK (for linear algebra operations). Three different algorithms are implemented in `owcsimpy`, i.e., [Carruthers & Kannan, 2002b], [Schulze, 2016], and [Jungnickel *et al.*, 2002].

Before explaining use cases of `owcsimpy`, we would like to emphasize that `owcsimpy` is developed with modularity in mind. In addition to the deterministic approaches as in [Carruthers & Kannan, 2002b], [Schulze, 2016], and [Jungnickel *et al.*, 2002], a stochastic approach, such

¹<https://www.minecraft.net/en-us/>

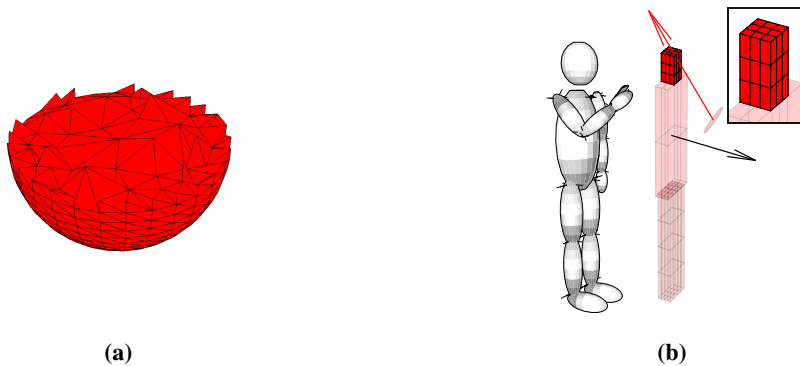


Figure A.2. (a) An example of the Delaunay triangulation to an arbitrary 3D object, and (b) a blocky and pixelated human model.

as the ray-tracing approach, can be implemented in the backend without affecting the frontend. Specular reflection can also be included by modifying the backend. Moreover, 3D objects can be created by means of a graphical user interface (GUI) instead of scripting with the expense of dependency to other libraries. Lastly, `owcsimpy` is distributed as a set of libraries instead of a standalone software for the sake of portability ('write once run everywhere'). Another reason is that users can collaborate with each other and flexibly integrate `owcsimpy` with other external libraries to enable advanced studies of LiFi.

A.3 Generating Geometry Models

An example of a cuboid, which is a basic building block of arbitrary 3D objects in this thesis, is shown in Figure A.3. Listing A.1 shows a Python snippet to generate the cuboid. As shown in the Python snippet, the cuboid is tilted by 30° and has the dimensions of $2 \times 1 \times 1 \text{ m}^3$. Moreover, all sides of the cuboid have the reflectivity value of 0.5. The arrows on each side in Figure A.3 show their orientations. From the combinations of planes and cuboids, a more complicated scenario can be generated, for example as shown in Figure A.4. Figure A.4(a) shows an illustration of a small indoor room, where a user sits while reading on a mobile device. Figure A.4(b) shows its corresponding models by using `owcsimpy`. In this case, the human's body and head are models by using cuboids. A chair is also modeled by a cuboid. A desk is simply modeled by a plane. Other objects, such as LEDs and PDs, are modeled by vectors.

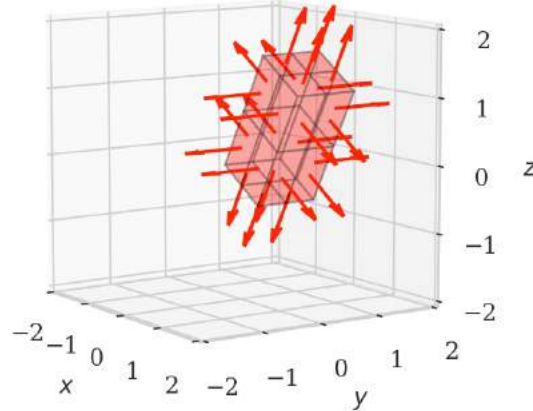


Figure A.3. An example of a cuboid whose sides are partitioned into 2×2 planes.

```

1 cube = Cube(
2     Vector(np.array([1,np.deg2rad(90),np.deg2rad(90)])),
3     ctrPoint = np.array([0.5,0.5,0.5]),
4     dimensions = [2,1,1],
5     RodriguesAngle = np.deg2rad(30),
6     reflectivities={'p0':0.5,'p1':0.5,'p2':0.5,
7                      'p3':0.5,'p4':0.5,'p5':0.5}
8 )
9 planes = cube.getPartition(2)
10 fig,ax = draw(planets=planes,alphas=0.2,
11                 xlim=[-2,2],ylim=[-2,2],zlim=[-2,2],
12                 azim=-34,elev=9
13 )
14

```

Listing A.1. A Python snippet to generate a cuboid shown in Figure A.3

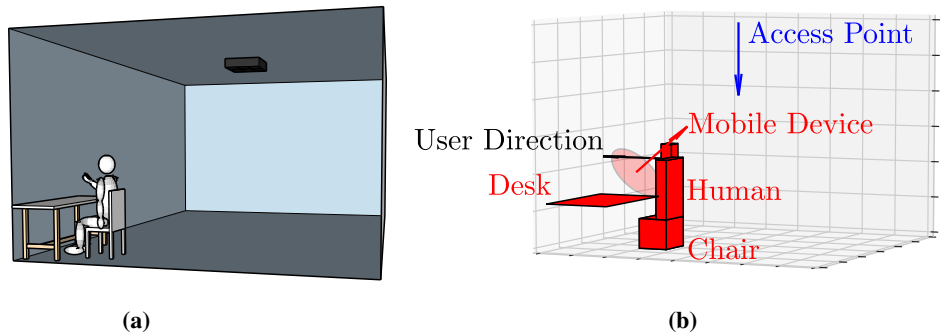


Figure A.4. (a) A 3D model of a small office environment, and (b) its corresponding model used in `owcsimpy`.

Appendix B

Brief Overview of Lomb-Scargle Periodograms

In this appendix, a brief overview of the Lomb-Scargle periodograms is presented. This overview focuses on the difference between the conventional periodograms and the Lomb-Scargle periodograms. More detailed discussions can be found in [Scargle, 1982; VanderPlas, 2018].

Suppose that a signal $X(t)$ is sampled, and it is denoted by $X(t_j)$, where $j \in \{1, 2, \dots, N\}$. Then, the conventional periodogram of $X(t_j)$ is defined by:

$$\begin{aligned} P_X(\omega) &= \frac{1}{N} \left| \sum_{j=1}^N X(t_j) \exp(-i\omega t_j) \right| \\ &= \frac{1}{N} \left[\left(\sum_{j=1}^N X(t_j) \cos(\omega t_j) \right)^2 + \left(\sum_{j=1}^N X(t_j) \sin(\omega t_j) \right)^2 \right]. \end{aligned} \quad (\text{B.1})$$

Scargle proposed a generalized form of the above expression with t_j being arbitrary (not necessarily evenly-spaced) as:

$$P_X(\omega) = \frac{A^2}{2} \left(\sum_{j=1}^N X(t_j) \cos(\omega(t_j - \tau)) \right)^2 + \frac{B^2}{2} \left(\sum_{j=1}^N X(t_j) \sin(\omega(t_j - \tau)) \right)^2. \quad (\text{B.2})$$

The parameters A , B , and τ are determined such that (i) (B.2) reduces to (B.1) if t_j is evenly spaced, and (ii) the periodogram is time-translation invariance. The Lomb-Scargle periodogram is defined as:

$$P_X(\omega) = \frac{1}{2} \left\{ \frac{\left(\sum_{j=1}^N X(t_j) \cos(\omega(t_j - \tau)) \right)^2}{\sum_{j=1}^N \cos^2(\omega(t_j - \tau))} + \frac{\left(\sum_{j=1}^N X(t_j) \sin(\omega(t_j - \tau)) \right)^2}{\sum_{j=1}^N \sin^2(\omega(t_j - \tau))} \right\}, \quad (\text{B.3})$$

where:

$$\tau = \frac{1}{2\omega} \tan^{-1} \left(\frac{\sum_{j=1}^N \sin(2\omega t_j)}{\sum_{j=1}^N \cos(2\omega t_j)} \right).$$

By using elementary trigonometry and defining:

$$\omega_n = \frac{2\pi n}{T},$$

where T is the time interval of $X(t)$, if t_j is evenly spaced, then:

$$\begin{aligned} \sum_{j=1}^N \sin(2\omega_n t_j) &= 0 \implies \tau = 0, \text{ and} \\ \sum_{j=1}^N \cos^2(\omega_n t_j) &= \sum_{j=1}^N \sin^2(\omega_n t_j) = N/2. \end{aligned}$$

Therefore, in this case (B.2) is equivalent (B.1).

Appendix C

Brief Overview of the IEEE 802.11ax

C.1 Introduction

In this thesis, OFDM-based systems are used for multicarrier systems. Furthermore, the baseband waveform is assumed to be compliant with the IEEE 802.11ax. For the sake of completeness, this chapter mainly provides the important feature of the IEEE 802.11ax that is relevant to this thesis.

C.2 Features

The IEEE 802.11ax operates in the 2.4 GHz and 5 GHz unlicensed bands. In the future, the 6 GHz unlicensed band can also be used for the IEEE 802.11ax. The IEEE 802.11ax supports the bandwidths of 20 MHz, 40 MHz, 80 MHz, 80+80 MHz (two non-adjacent 80 MHz channels), and 160 MHz. The fast fourier transform (FFT) sizes are either 256, 512, 1024, or 2048 with the subcarrier spacing of 78.125 kHz. One of the main feature of the IEEE 802.11ax is the use of orthogonal frequency-division multiple access (OFDMA), which mitigate the frequency selectivity issue with the IEEE 802.11ac with the bandwidth greater than 40 MHz channels [Khorov, Kiryanov, Lyakhov, & Bianchi, 2019]. The OFDMA in the IEEE 802.11ax is a frame-based [Khorov *et al.*, 2019]. That is, multiuser frames occupies different subcarriers for the entire frame duration. In order to maintain the backward compatibility, the OFDMA is applied on top of the carrier sense multiple access with collision avoidance (CSMA/CA). It means that, for example, an AP has an access to the channel by means of CSMA/CA, then the AP can employ the OFDMA. In addition, the IEEE 802.11ax also supports a multiuser multiple-input, multiple-output (MIMO). The IEEE 802.11ax introduces a new MCS, with the maximum constellation size of 1024-QAM. Forward error corrections that are used in the IEEE 802.11ax are convolutional coded or low-density parity-check codes with the highest coding rate of 5/6. Moreover, the maximum number of spatial streams is 8. The IEEE 802.11ax offers a theoretical maximum data rate of 9.6 Gbps.

With regards to this thesis, a new feature of the IEEE 802.11ax is the use of multiuser MIMO or OFDMA for uplink transmissions. This amendment is postponed in the previous IEEE 802.11ac amendment due to the need of further investigation on the tight synchronization of uplink multiuser transmissions. The synchronization in the IEEE 802.11ax is carried out based on a new type of control frame, namely *trigger frame*. That is, an AP sends a trigger frame, which contains information such as MCS indexes, the guard interval or the number of allocated tones, known as resource unit (RU), for the stations. Then, a short inter frame space (SIFS) after that the stations transmits to the AP. The SIFS can be either $10\ \mu s$ or $16\ \mu s$. Based on [Naik, Bhattacharai, & Park, 2018], an acceptable delay difference of the received frames for the multiuser uplink transmissions is less than $3\ \mu s$. It is worth noting here that, the IEEE 802.11ax targets both indoor and outdoor scenarios. In order to mitigate the Doppler effects that are suffered by fast moving stations, e.g., cars, the IEEE 802.11ax introduces *midambles*, which are placed between payload data. In addition, an MMSE-successive interference cancellation (SIC) is employed in the AP to decode the received frame. Therefore, in terms of delay, there should be no problem in terms of delay differences of received frames.

In the IEEE 802.11ax, there are other improvements on the length of the guard interval, the symbol duration, the power management, and many others. Discussions of these improvements are outside the scope of this thesis. A good summary of these new features can be found in [Khorov *et al.*, 2019].

References

- 3GPP. (2020). *3rd Generation Partnership Project; Technical Specification Group Services and System Aspects; System architecture for the 5G System (5GS); Stage 2 (Release 16)*. https://www.3gpp.org/ftp/Specs/archive/23_series/23.501/23501-g40.zip.
- 3GPP TR 25.892. (2004). *Feasibility Study for OFDM for UTRAN enhancement (release 6)v1.1.0*.
- Abu-alhiga, R., & Haas, H. (2009, Sept). Subcarrier-index modulation OFDM. In *2009 IEEE 20th International Symposium on Personal, Indoor and Mobile Radio Communications* (p. 177-181). Tokyo, Japan. doi: 10.1109/PIMRC.2009.5449882
- Acolatse, K., Bar-Ness, Y., & Wilson, S. K. (2011, January). Novel Techniques of Single-Carrier Frequency-Domain Equalization for Optical Wireless Communications. , *2011*. doi: 10.1155/2011/393768
- Agrell, E., Lassing, J., Strom, E. G., & Ottosson, T. (2004, Dec). On the optimality of the binary reflected Gray code. *IEEE Transactions on Information Theory*, *50*(12), 3170-3182. doi: 10.1109/TIT.2004.838367
- Al-Kinani, A., Wang, C., Zhou, L., & Zhang, W. (2018). Optical Wireless Communication Channel Measurements and Models. *IEEE Communications Surveys Tutorials*, *20*(3), 1939-1962.
- Alexa. (2020). *The top 500 sites on the web*. <https://www.alexa.com/topsites>.
- Alshaer, H., & Haas, H. (2016). SDN-enabled Li-Fi/Wi-Fi wireless medium access technologies integration framework. In *2016 IEEE Conference on Standards for Communications and Networking (CSCN)* (p. 1-6). Berlin, Germany.
- Anamalamudi, S., Sangi, A. R., Alkatheiri, M., Muhaya, F. T. B., & Liu, C. (2018). 5G-WLAN Security. In *A Comprehensive Guide to 5G Security* (p. 143–163). doi: 10.1002/9781119293071.ch7
- Apple. (2017). *Use Multipath TCP to create backup connections for iOS*. <https://support.apple.com/en-us/HT201373>.
- Arfaoui, M. A., Soltani, M. D., Tavakkolia, I., Ghrayeb, A., Assi, C., Haas, H., & Safari, M. (2019). SNR Statistics of Indoor Mobile VLC Users with Random Device Orientation. In *2019 IEEE International Conference on Communications Workshops (ICC Workshops)* (p. 1-6). Shanghai, China.
- Armstrong, J., & Lowery, A. J. (2006). Power efficient optical OFDM. *Electronics Letters*, *42*(6), 370-372.
- Baisch, S., & Bokelmann, G. H. (1999). Spectral analysis with incomplete time series: an example from seismology. *Computers & Geosciences*, *25*(7), 739 - 750.
- Barry, J. R., Kahn, J. M., Krause, W. J., Lee, E. A., & Messerschmitt, D. G. (1993, April). Simulation of multipath impulse response for indoor wireless optical channels. *IEEE Journal on Selected Areas in Communications*, *11*(3), 367-379. doi: 10.1109/49.219552
- Basar, E. (2018, March). Orbital Angular Momentum With Index Modulation. *IEEE Transactions on Wireless Communications*, *17*(3), 2029-2037. doi: 10.1109/TWC.2017.2787992

- Basar, E., Wen, M., Mesleh, R., Renzo, M. D., Xiao, Y., & Haas, H. (2017). Index Modulation Techniques for Next-Generation Wireless Networks. *IEEE Access*, 5, 16693-16746. doi: 10.1109/ACCESS.2017.2737528
- Bello, P. (1963, December). Characterization of randomly time-variant linear channels. *IEEE Transactions on Communications Systems*, 11(4), 360-393. doi: 10.1109/TCOM.1963.1088793
- Bernadó, L., Zemen, T., Tufvesson, F., Molisch, A. F., & Mecklenbräuker, C. F. (2012, Sep.). The (in-) validity of the WSSUS assumption in vehicular radio channels. In *2012 IEEE 23rd International Symposium on Personal, Indoor and Mobile Radio Communications - (PIMRC)* (p. 1757-1762). Sydney, NSW, Australia. doi: 10.1109/PIMRC.2012.6362634
- Bian, R., Tavakkolnia, I., & Haas, H. (2019). 15.73 Gb/s Visible Light Communication With Off-the-Shelf LEDs. *Journal of Lightwave Technology*, 37(10), 2418-2424.
- Bober, K. L., Jungnickel, V., Hinrichs, M., & Serafimofski, N. (2019). *TGbb: Evaluation methodology for PHY and MAC proposals*. <https://mentor.ieee.org/802.11/dcn/19/11-19-0187-04-00bb-evaluation-methodology-for-phy-and-mac-proposals.docx>.
- Brueninghaus, K., Astely, D., Salzer, T., Visuri, S., Alexiou, A., Karger, S., & Seraji, G. . (2005). Link performance models for system level simulations of broadband radio access systems. In *2005 IEEE 16th International Symposium on Personal, Indoor and Mobile Radio Communications* (Vol. 4, p. 2306-2311 Vol. 4). Berlin, Germany.
- BSI British Standards Std. (2008, September). *BS EN 62471:2008-Photobiological Safety of Lamps and Lamp Systems*.
- Bykhovsky, D. (2018, May). Coherence distance in indoor optical wireless communication channels. *Optics Letters*, 43(10), 2248–2251. doi: 10.1364/OL.43.002248
- Bykhovsky, D., & Arnon, S. (2014). An experimental comparison of different bit-and-power-allocation algorithms for dco-ofdm. *Journal of Lightwave Technology*, 32(8), 1559-1564.
- Carruthers, J. B., & Kahn, J. M. (1994). Multiple-subcarrier modulation for non-directed wireless infrared communication. In *1994 IEEE GLOBECOM. Communications: The Global Bridge* (Vol. 2, p. 1055-1059 vol.2). San Francisco, CA, USA, USA.
- Carruthers, J. B., & Kannan, P. (2002a). *IRSIMIT- Infrared Impulse Response Simulator by Iterations*. <http://iss.bu.edu/bwc/irsimit/>.
- Carruthers, J. B., & Kannan, P. (2002b, May). Iterative site-based modeling for wireless infrared channels. *IEEE Transactions on Antennas and Propagation*, 50(5), 759-765. doi: 10.1109/TAP.2002.1011244
- Chen, C., Basnayaka, D., Purwita, A. A., Wu, X., & Haas, H. (n.d.). Wireless Infrared-based LiFi Uplink Transmission with Link Blockage and Random Device Orientation. *IEEE Transactions on Communications (accepted)*.
- Chen, C., Basnayaka, D., Purwita, A. A., Wu, X., & Haas, H. (2019). *Physical Layer Performance Evaluation of Wireless Infrared-based LiFi Uplink*.
- Chen, C., Basnayaka, D. A., & Haas, H. (2016, Jan). Downlink Performance of Optical Attocell Networks. *Journal of Lightwave Technology*, 34(1), 137-156. doi: 10.1109/JLT.2015.2511015
- Chen, C., & Haas, H. (2017). Performance Evaluation of Downlink Cooperative Multipoint Joint Transmission in LiFi Systems. In *2017 IEEE Globecom Workshops (GC Wkshps)* (p. 1-6). Singapore, Singapore.

- Chen, C., Soltani, M. D., Safari, M., Purwita, A. A., Wu, X., & Haas, H. (2019). An Omnidirectional User Equipment Configuration to Support Mobility in LiFi Networks. In *2019 IEEE International Conference on Communications Workshops (ICC Workshops)* (p. 1-6). Shanghai, China.
- Chen, C., Zhong, W.-D., & Wu, D. (2017, Jan). Non-Hermitian Symmetry Orthogonal Frequency Division Multiplexing for Multiple-Input Multiple-Output Visible Light Communications. *Journal of Optical Communications and Networking*, 9(1), 36–44. doi: 10.1364/JOCN.9.000036
- Chen, J., Tavakkolia, I., Chen, C., Wang, Z., & Haas, H. (2020). The Movement-Rotation (MR) Correlation Function and Coherence Distance of VLC Channels. *Journal of Lightwave Technology*, 1-1.
- Choi, J. (2017, May). Single-carrier index modulation and CS detection. In *2017 IEEE International Conference on Communications (ICC)* (p. 1-6). Paris, France. doi: 10.1109/ICC.2017.7996385
- Chowdhury, M. Z., Hasan, M. K., Shahjalal, M., Hossan, M. T., & Jang, Y. M. (2020). Optical Wireless Hybrid Networks: Trends, Opportunities, Challenges, and Research Directions. *IEEE Communications Surveys Tutorials*, 22(2), 930-966.
- Chowdhury, M. Z., Hossan, M. T., Islam, A., & Jang, Y. M. (2018). A Comparative Survey of Optical Wireless Technologies: Architectures and Applications. *IEEE Access*, 6, 9819-9840.
- Chun, H., Gomez, A., Faulkner, G., & O'Brien, D. (2018, Jun). A spectrally efficient equalization technique for optical sources with direct modulation. *Optics Letters*, 43(11), 2708–2711. doi: 10.1364/OL.43.002708
- Cisco. (2020, March). *Cisco Annual Internet Report (2018–2023) White Paper*. White Paper.
- Cogalan, T., & Haas, H. (2017). Why would 5G need optical wireless communications? In *2017 IEEE 28th Annual International Symposium on Personal, Indoor, and Mobile Radio Communications (PIMRC)* (p. 1-6).
- CommScope. (2018). *Smart Building Activity*. <https://www.commscope.com/globalassets/digizuite/3296-smart-building-ebook-co-109520-en.pdf?r=1>. (accessed October 30, 2020)
- Cooksey, C. C., & Allen, D. W. (2013, May). Reflectance measurements of human skin from the ultraviolet to the shortwave infrared (250 nm to 2500 nm). In *Proceedings of SPIE Defense, Security & Sensing*. Baltimore, MD.
- Cox, J. H., Chung, J., Donovan, S., Ivey, J., Clark, R. J., Riley, G., & Owen, H. L. (2017). Advancing Software-Defined Networks: A Survey. *IEEE Access*, 5, 25487-25526.
- Dehghani Soltani, M., Purwita, A. A., Tavakkolia, I., Haas, H., & Safari, M. (2019). Impact of Device Orientation on Error Performance of LiFi Systems. *IEEE Access*, 7, 41690-41701.
- Deng, S. (1996). Empirical model of WWW document arrivals at access link. In *Proceedings of ICC/SUPERCOMM '96 - International Conference on Communications* (Vol. 3, p. 1797-1802 vol.3). Dallas, TX, USA.
- Deveri, A. (2020a). *HTTP/2 protocol*. <https://caniuse.com/#search=http2>.
- Deveri, A. (2020b). *HTTP/3 protocol*. <https://caniuse.com/#search=http3>.
- Dick, O. (2017). From healthy to pathology through a fall in dynamical complexity of involuntary oscillations of the human hand. *Neurocomputing*, 243, 142 - 154.
- Edmund Optics®. (2020). *Basic Principles of Silicon Detectors*. <https://www.edmundoptics.com/knowledge-center/application-notes/>

- testing-and-detection/basic-principles-of-silicon-detectors/. (accessed October 30, 2020)
- Ericsson. (2003). Effective SNR mapping for modelling frame error rates in multiple-state channels. *3GPP2-C30-20030429-010*.
- Eroğlu, Y. S., Yapıcı, Y., & Güvenç, I. (2019). Impact of Random Receiver Orientation on Visible Light Communications Channel. *IEEE Transactions on Communications*, 67(2), 1313-1325.
- FCC. (2010, Oct). *Mobile Broadband: The Benefits of Additional Spectrum*. FCC Staff Technical Paper.
- Fernando, N., Hong, Y., & Viterbo, E. (2011). Flip-OFDM for optical wireless communications. In *2011 IEEE Information Theory Workshop* (p. 5-9). Paraty, Brazil.
- Fischer, R. (2002). *Precoding and Signal Shaping for Digital Transmission*. Wiley.
- Ford, A., Raiciu, C., Handley, M., Barre, S., & Iyengar, J. (2011). *Architectural guidelines for multipath tcp development*. <https://tools.ietf.org/html/rfc6182>.
- Gfeller, F. R., & Bapst, U. (1979). Wireless in-house data communication via diffuse infrared radiation. *Proceedings of the IEEE*, 67(11), 1474-1486.
- Ghassemlooy, Z., Popoola, W., & Rajbhandari, S. (2018). *Optical wireless communications: System and channel modelling with matlab* (2nd ed.). USA: CRC Press, Inc.
- Giordani, M., Polese, M., Mezzavilla, M., Rangan, S., & Zorzi, M. (2020). Toward 6G Networks: Use Cases and Technologies. *IEEE Communications Magazine*, 58(3), 55-61.
- Gresty, M., & Buckwell, D. (1990). Spectral analysis of tremor: understanding the results. *Journal of Neurology, Neurosurgery & Psychiatry*, 53(11), 976-981. doi: 10.1136/jnnp.53.11.976
- Grobe, L., Jungnickel, V., Langer, K., Haardt, M., & Wolf, M. (2016). On the impact of highpass filtering when using PAM-FDE for visible light communication. In *2016 IEEE Wireless Communications and Networking Conference* (p. 1-7). Doha, Qata.
- Guo, X., Ansari, N., Hu, F., Shao, Y., Elikplim, N. R., & Li, L. (2020). A Survey on Fusion-Based Indoor Positioning. *IEEE Communications Surveys Tutorials*, 22(1), 566-594.
- Haas, H., & Abu-Alhiga, R. I. T. (2016, January 27). *Encoding method by conveying coded bit information on patterns of different modulation schemes on orthogonal resource units* (No. EP2476210B1). Edinburgh, UK.
- Haas, H., Yin, L., Chen, C., Videv, S., Parol, D., Poves, E., ... Islim, M. S. (2020). Introduction to indoor networking concepts and challenges in LiFi. *IEEE/OSA Journal of Optical Communications and Networking*, 12(2), A190-A203.
- Haas, H., Yin, L., Wang, Y., & Chen, C. (2016, March). What is LiFi? *Journal of Lightwave Technology*, 34(6), 1533-1544. doi: 10.1109/JLT.2015.2510021
- Harashima, H., & Miyakawa, H. (1972, Aug). Matched-Transmission Technique for Channels With Intersymbol Interference. *IEEE Transactions on Communications*, 20(4), 774-780. doi: 10.1109/TCOM.1972.1091221
- He, K., Khalid, J., Gember-Jacobson, A., Das, S., Prakash, C., Akella, A., ... Thottan, M. (2015). Measuring Control Plane Latency in SDN-Enabled Switches. In *Proceedings of the 1st ACM SIGCOMM Symposium on Software Defined Networking Research*. New York, NY, USA: Association for Computing Machinery. doi: 10.1145/2774993.2775069
- Herdin, M., Czink, N., Ozcelik, H., & Bonek, E. (2005, May). Correlation matrix distance, a meaningful measure for evaluation of non-stationary MIMO channels. In *2005 IEEE*

- 61st Vehicular Technology Conference* (Vol. 1, p. 136-140 Vol. 1). Stockholm, Sweden. doi: 10.1109/VETECS.2005.1543265
- Hinrichs, M., Hilt, J., Hellwig, P., Jungnickel, V., & Bober, K. L. (2019). *TGbb PHY proposal*. <https://mentor.ieee.org/802.11/dcn/19/11-19-0087-01-00bb-optical-frontend-model-for-phy-simulation.docx>.
- Hong, S., Rhee, I., Kim, S. J., Lee, K., & Chong, S. (2008). Routing Performance Analysis of Human-Driven Delay Tolerant Networks Using the Truncated Levy Walk Model. In *Proceedings of the 1st ACM SIGMOBILE Workshop on Mobility Models* (p. 25–32). New York, NY, USA: Association for Computing Machinery. doi: 10.1145/1374688.1374694
- Hsieh, C., & Shiu, D. (2006). Single Carrier Modulation with Frequency Domain Equalization for Intensity Modulation-Direct Detection Channels with Intersymbol Interference. In *2006 IEEE 17th International Symposium on Personal, Indoor and Mobile Radio Communications* (p. 1-5). Helsinki, Finland.
- IEEE 802.15 TG 13. (2019, September). *IEEE 802.15 WPANTM task group 13 (TG13) multi-gigabit/s optical wireless communications*. <http://www.ieee802.org/15/pub/TG13.html>.
- IEEE 802.15 TG 7m. (2019, September). *IEEE 802.15 WPANTM 15.7 maintenance: Short-range optical wireless communications task group (TG 7m)*. http://www.ieee802.org/15/pub/IEEE%20802_15%20WPAN%2015_7%20Revision1%20Task%20Group.htm.
- IEEE P802.11 TGad. (2012). IEEE Standard for Information technology—Telecommunications and information exchange between systems—Local and metropolitan area networks—Specific requirements—Part 11: Wireless LAN Medium Access Control (MAC) and Physical Layer (PHY) Specifications Amendment 3: Enhancements for Very High Throughput in the 60 GHz Band. *IEEE Std 802.11ad-2012 (Amendment to IEEE Std 802.11-2012, as amended by IEEE Std 802.11ae-2012 and IEEE Std 802.11aa-2012)*, 1-628.
- IEEE P802.11 TGax. (2018, July). IEEE draft standard for information technology – telecommunications and information exchange between systems local and metropolitan area networks – specific requirements part 11: Wireless LAN medium access control (MAC) and physical layer (PHY) specifications amendment enhancements for high efficiency WLAN. *IEEE P802.11ax/D3.0, June 2018*, 1-682.
- International Electrotechnical Commission. (1993). *CEI/IEC 825-1: Safety of Laser Product*.
- Ishikawa, N., Sugiura, S., & Hanzo, L. (2018, thirdquarter). 50 Years of Permutation, Spatial and Index Modulation: From Classic RF to Visible Light Communications and Data Storage. *IEEE Communications Surveys Tutorials*, 20(3), 1905-1938. doi: 10.1109/COMST.2018.2815642
- ITU-T G.9991. (2019). High-speed indoor visible light communication transceiver – System architecture, physical layer and data link layer specification. *Rec. ITU-T G.9991, International Telecommunications Union*.
- Januszkiewicz, L. (2018). Analysis of Human Body Shadowing Effect on Wireless Sensor Networks Operating in the 2.4 GHz Band. *Sensors (Basel, Switzerland)*, 18(10), 3412.
- Johnson, D. B., & Maltz, D. A. (1996). Dynamic Source Routing in Ad Hoc Wireless Network. In *Mobile Computing* (Vol. 353). Imielinski and Korth, Eds. Kluwer Academic Publishers.
- Jung-Fu Cheng. (2004). Coding performance of various type-I HARQ schemes with BICM. In *International Symposium onInformation Theory, 2004. ISIT 2004. Proceedings*. (p. 319-

- 319). Chicago, IL, USA.
- Jungnickel, V., Bober, K. L., Hinrichs, M., Vazquez, M. M., Dauphinee, L., Molinero, S. I., ... Emmelmann, M. (2019). *LC-optimized PHY proposal for TGbb*. <https://mentor.ieee.org/802.11/dcn/19/11-19-1053-02-00bb-lc-optimized-phy-proposal-for-tgbb.pptx>.
- Jungnickel, V., Pohl, V., Nonnig, S., & von Helmolt, C. (2002, April). A physical model of the wireless infrared communication channel. *IEEE Journal on Selected Areas in Communications*, 20(3), 631-640. doi: 10.1109/49.995522
- Kahn, J. M., & Barry, J. R. (1997, Feb). Wireless infrared communications. *Proceedings of the IEEE*, 85(2), 265-298. doi: 10.1109/5.554222
- Kahn, J. M., Krause, W. J., & Carruthers, J. B. (1995). Experimental characterization of non-directed indoor infrared channels. *IEEE Transactions on Communications*, 43(2/3/4), 1613-1623.
- Khalid, A. M., Cossu, G., Corsini, R., Choudhury, P., & Ciaramella, E. (2012). 1-Gb/s Transmission Over a Phosphorescent White LED by Using Rate-Adaptive Discrete Multitone Modulation. *IEEE Photonics Journal*, 4(5), 1465-1473.
- Khalighi, M. A., Long, S., Bourennane, S., & Ghassemlooy, Z. (2017). PAM- and CAP-based transmission schemes for visible-light communications. *IEEE Access*, 5, 27002-27013. doi: 10.1109/ACCESS.2017.2765181
- Khallaaf, H. S., El-Fiqi, A. E., Elwekeil, M., Shalaby, H. M. H., & Obayya, S. S. A. (2017). Efficiency of opportunistic cellular/LiFi traffic offloading. In *2017 19th International Conference on Transparent Optical Networks (ICTON)* (p. 1-4). Girona, Spain.
- Khorov, E., Kiryanov, A., Lyakhov, A., & Bianchi, G. (2019). A Tutorial on IEEE 802.11ax High Efficiency WLANs. *IEEE Communications Surveys Tutorials*, 21(1), 197-216.
- Kim, D., Park, J. K., & Kim, J. T. (2019). Three-Dimensional VLC Positioning System Model and Method Considering Receiver Tilt. *IEEE Access*, 7, 132205-132216.
- Kim, J. G., Yu, H. K., Mariappan, V., & Cha, J. S. (2019). *VLC based Simulation Results in Enterprise and Industrial Environment*. <https://mentor.ieee.org/802.11/dcn/19/11-19-0875-02-00bb-vlc-based-simulation-results-in-enterprise-and-industrial-environment.pptx>.
- Kokaly, R., et al. (2017). *USGS Spectral Library Version 7*. https://crustal.usgs.gov/speclab/data/GIFplots/GIFplots_splib07a/ChapterA_ArtificialMaterials/splib07a_Cotton_Fabric_GDS437_White_ASDFRA_AREF.gif.
- Komine, T., Lee, J. H., Haruyama, S., & Nakagawa, M. (2009). Adaptive equalization system for visible light wireless communication utilizing multiple white LED lighting equipment. *IEEE Transactions on Wireless Communications*, 8(6), 2892-2900.
- Komine, T., Tanaka, Y., Haruyama, S., & Nakagawa, M. (2001). Basic Study on Visible-Light Communication using Light Emitting Diode Illuminationn. In *Proc. of 8th International Symposium on Microwave and Optical Technology (ISMOT 2001)* (p. 45-48). Montreal, Canadaa.
- Lee, K., Lee, J., Yi, Y., Rhee, I., & Chong, S. (2013). Mobile Data Offloading: How Much Can WiFi Deliver? *IEEE/ACM Transactions on Networking*, 21(2), 536-550.
- Lee, K., Park, H., & Barry, J. R. (2011). Indoor Channel Characteristics for Visible Light Communications. *IEEE Communications Letters*, 15(2), 217-219.
- Leibowitz, B. S., Boser, B. E., & Pister, K. S. J. (2001). CMOS smart pixel for free-space optical communication. In N. Sampat, J. Canosa, M. M. Blouke, J. Canosa, & N. Sampat

- (Eds.), *Sensors and Camera Systems for Scientific, Industrial, and Digital Photography Applications II* (Vol. 4306, pp. 308 – 318). SPIE. doi: 10.1117/12.426966
- Li, X., Zhang, R., & Hanzo, L. (2015). Cooperative Load Balancing in Hybrid Visible Light Communications and WiFi. *IEEE Transactions on Communications*, 63(4), 1319-1329.
- Liu, C., White, R. W., & Dumais, S. (2010). Understanding Web Browsing Behaviors through Weibull Analysis of Dwell Time. In *Proceedings of the 33rd International ACM SIGIR Conference on Research and Development in Information Retrieval* (p. 379–386). New York, NY, USA: Association for Computing Machinery.
- Liu, Y., Qin, X., Zhang, T., Zhu, T., Chen, X., & Wei, G. (2018). Decoupled TCP extension for VLC hybrid network. *IEEE/OSA Journal of Optical Communications and Networking*, 10(5), 563-572.
- Lu, Q., Ji, X., & Huang, K. (2014). Clipping distortion analysis and optimal power allocation for aco-ofdm based visible light communication. In *2014 4th IEEE International Conference on Information Science and Technology* (p. 320-323). Shenzhen, China.
- Ma, W., & Zhang, L. (2018). QoE-Driven Optimized Load Balancing Design for Hybrid LiFi and WiFi Networks. *IEEE Communications Letters*, 22(11), 2354-2357.
- MATLAB®. (2020). *WLAN Toolbox*. <https://uk.mathworks.com/help/wlan/>.
- Matz, G. (2005, Sep.). On non-WSSUS wireless fading channels. *IEEE Transactions on Wireless Communications*, 4(5), 2465-2478. doi: 10.1109/TWC.2005.853905
- McCreary, S. (2020). *Trends in Wide Area IP Traffic Patterns*. <https://www.caida.org/publications/papers/2000/AIX0005/AIX0005.html>.
- Merlin, S., Barriac, G., Sampath, H., Cariou, L., Derham, T., Rouzic, J.-P. L., ... Wang, X. (2015). *TGax Simulation Scenarios*. <https://mentor.ieee.org/802.11/dcn/14/11-14-0980-16-00ax-simulation-scenarios.docx>.
- Mesleh, R., Haas, H., Ahn, C. W., & Yun, S. (2006, Oct). Spatial Modulation - A New Low Complexity Spectral Efficiency Enhancing Technique. In *2006 First International Conference on Communications and Networking in China* (p. 1-5). Beijing, China. doi: 10.1109/CHINACOM.2006.344658
- Mesleh, R. Y., Haas, H., Sinanovic, S., Ahn, C. W., & Yun, S. (2008, July). Spatial Modulation. *IEEE Transactions on Vehicular Technology*, 57(4), 2228-2241. doi: 10.1109/TVT.2007.912136
- Miramirkhani, F., Uysal, M., & Panayirci, E. (2015). Novel channel models for visible light communications. In B. B. Dingel & K. Tsukamoto (Eds.), *Broadband Access Communication Technologies IX* (Vol. 9387, pp. 150 – 162). SPIE. doi: 10.1117/12.2077565
- Naik, G., Bhattacharai, S., & Park, J. (2018). Performance Analysis of Uplink Multi-User OFDMA in IEEE 802.11ax. In *2018 IEEE International Conference on Communications (ICC)* (p. 1-6).
- Nakao, M., Ishihara, T., & Sugiura, S. (2017, Feb). Single-Carrier Frequency-Domain Equalization With Index Modulation. *IEEE Communications Letters*, 21(2), 298-301. doi: 10.1109/LCOMM.2016.2626447
- Nuwanpriya, A., Grant, A., Ho, S., & Luo, L. (2012). Position Modulating OFDM for optical wireless communications. In *2012 IEEE Globecom Workshops* (p. 1219-1223). Anaheim, CA, USA.
- Nuwanpriya, A., Ho, S. W., Zhang, J. A., Grant, A. J., & Luo, L. (2015, July). PAM-SCFDE for Optical Wireless Communications. *Journal of Lightwave Technology*, 33(14), 2938-2949. doi: 10.1109/JLT.2015.2424456

- Obeed, M., Salhab, A. M., Zummo, S. A., & Alouini, M. (2018). Joint optimization of power allocation and load balancing for hybrid vlc/rf networks. *IEEE/OSA Journal of Optical Communications and Networking*, 10(5), 553-562.
- Paier, A., Zemen, T., Bernado, L., Matz, G., Karedal, J., Czink, N., ... Mecklenbrauker, C. F. (2008, Feb). Non-WSSUS vehicular channel characterization in highway and urban scenarios at 5.2GHz using the local scattering function. In *2008 International ITG Workshop on Smart Antennas* (p. 9-15). Vienna, Austria. doi: 10.1109/WSA.2008.4475530
- Palomar, D. P., Cioffi, J. M., & Lagunas, M. A. (2003, Sept). Joint Tx-Rx beamforming design for multicarrier MIMO channels: a unified framework for convex optimization. *IEEE Transactions on Signal Processing*, 51(9), 2381-2401. doi: 10.1109/TSP.2003.815393
- Peng, B., & Kürner, T. (2017, May). Three-Dimensional Angle of Arrival Estimation in Dynamic Indoor Terahertz Channels Using a Forward-Backward Algorithm. *IEEE Transaction on Vehicular Technology*, 66(5), 3798-3811. doi: 10.1109/TVT.2016.2599488
- Popoola, W. O., Poves, E., & Haas, H. (2013, May). Error Performance of Generalised Space Shift Keying for Indoor Visible Light Communications. *IEEE Transactions on Communications*, 61(5), 1968-1976. doi: 10.1109/TCOMM.2013.022713.120501
- Porat, R., Fischer, M., Merlin, S., Vermani, S., Au, E., Yangxun, D., ... Oteri, K. (2016). *11ax Evaluation Methodology*. <https://mentor.ieee.org/802.11/dcn/18/11-18-1582-04-00bb-ieee-802-11bb-reference-channel-models-for-indoor-environments.pdf>.
- Proakis. (2007). *Digital communications 5th edition*. McGraw Hill.
- Purwita, A., Haas, H., Serafimovski, N., Afgani, M., Berner, S., Walker, D., ... Miramirkhani, F. (2020). *Proposed Center Frequency for the Common Mode Mandatory PHY*. <https://mentor.ieee.org/802.11/dcn/20/11-20-0572-00-00bb-proposed-center-frequency-mandatory-phy.pptx>.
- Purwita, A., Haas, H., Serafimovski, N., & Berner, S. (2020). *Proposed Center Frequency for the Common Mode Mandatory PHY*. <https://mentor.ieee.org/802.11/dcn/20/11-20-0815-00-00bb-proposed-center-frequency-for-common-mode-mandatory-phy.pptx>.
- Purwita, A., Rossius, A., Haas, H., Serafimovski, N., Afgani, M., Berner, S., ... Uysal, M. (2020). *Proposals and related work on Center Frequency for the Common Mode Mandatory PHY*. <https://mentor.ieee.org/802.11/dcn/20/11-20-1449-03-00bb-proposals-and-related-work-on-center-frequency-for-the-common-mode-mandatory-phy.pptx>.
- Purwita, A., Videv, S., Haas, H., & Serafimofski, N. (2019, September). *Spectral Flatness Test of the TGbb's Reference Channel Models with HE Waveform*. Retrieved from <https://mentor.ieee.org/802.11/dcn/19/11-19-1639-01-00bb-spectral-flatness-test-of-the-tgbb-refrence-channel-models-with-he-waveform.pptx>
- Purwita, A. A. (2020). *owcsimpy: a Python simulator for optical wireless communications*. <https://github.com/ardimasp/owcsimpy>. (accessed October 30, 2020)
- Purwita, A. A., Chen, C., Safari, M., & Haas, H. (2019). Cyclic-Prefixed System with PAM using DFE and THP for Uplink Transmission in LiFi. In *ICC 2019 - 2019 IEEE International Conference on Communications (ICC)* (p. 1-6). Shanghai, China.
- Purwita, A. A., Dehghani Soltani, M., Safari, M., & Haas, H. (2018). Impact of terminal orientation on performance in LiFi systems. In *2018 IEEE Wireless Communications and Networking Conference (WCNC)* (p. 1-6). Barcelona, Spain.

- Purwita, A. A., & Haas, H. (2020a). IQ-WDM for IEEE 802.11bb-based LiFi. In *2020 IEEE Wireless Communications and Networking Conference (WCNC)* (p. 1-6). Seoul, Korea (South).
- Purwita, A. A., & Haas, H. (2020b). Studies of Flatness of LiFi Channel for IEEE 802.11bb. In *2020 IEEE Wireless Communications and Networking Conference (WCNC)* (p. 1-6). Seoul, Korea (South).
- Purwita, A. A., Soltani, M. D., Safari, M., & Haas, H. (2018). Handover Probability of Hybrid LiFi/RF-Based Networks with Randomly-Oriented Devices. In *2018 IEEE 87th Vehicular Technology Conference (VTC Spring)* (p. 1-5). Porto, Portugal.
- Purwita, A. A., Soltani, M. D., Safari, M., & Haas, H. (2019). Terminal Orientation in OFDM-Based LiFi Systems. *IEEE Transactions on Wireless Communications*, 18(8), 4003-4016.
- Purwita, A. A., Yesilkaya, A., Cogalan, T., Safari, M., & Haas, H. (2019). Generalized Time Slot Index Modulation for LiFi. In *2019 IEEE 30th Annual International Symposium on Personal, Indoor and Mobile Radio Communications (PIMRC)* (p. 1-7). Istanbul, Turkey.
- Purwita, A. A., Yesilkaya, A., Safari, M., & Haas, H. (2020). Generalized Time Slot Index Modulation for Optical Wireless Communications. *IEEE Transactions on Communications*, 68(6), 3706-3719.
- Rahaim, M. (2018). *Communication and Lighting Environment Simulation (CandLES)*. <https://github.com/UCaNLabUMB/CandLES>.
- Rebecchi, F., Dias de Amorim, M., Conan, V., Passarella, A., Bruno, R., & Conti, M. (2015). Data Offloading Techniques in Cellular Networks: A Survey. *IEEE Communications Surveys Tutorials*, 17(2), 580-603.
- Roberts, D. H., Lehar, J., & Dreher, J. W. (1987, Apr). Time Series Analysis with Clean - Part One - Derivation of a Spectrum. *Astronomical Journal*, 93, 968. doi: 10.1086/114383
- Rossius, A., Berner, S., Weszely, T., Purwita, A., Haas, H., Serafimovski, N., ... Han, C. (2020). *Experimental results for TGbb centre frequency discussion*. <https://mentor.ieee.org/802.11/dcn/20/11-20-1037-00-00bb-experimental-results-for-tgbb-centre-freq-discussion.pptx>.
- Royer, E. M., Melliar-Smith, P. M., & Moser, L. E. (2001, June). An analysis of the optimum node density for ad hoc mobile networks. In *ICC 2001. IEEE International Conference on Communications. Conference Record (Cat. No.01CH37240)* (Vol. 3, p. 857-861 vol.3). Helsinki, Finland. doi: 10.1109/ICC.2001.937360
- Saad, W., Bennis, M., & Chen, M. (2019). A Vision of 6G Wireless Systems: Applications, Trends, Technologies, and Open Research Problems. *IEEE Network*, 1-9.
- Scaglione, A., Giannakis, G. B., & Barbarossa, S. (1999, Jul). Redundant filterbank precoders and equalizers. I. Unification and optimal designs. *IEEE Transactions on Signal Processing*, 47(7), 1988-2006. doi: 10.1109/78.771047
- Scargle, J. D. (1982, December). Studies in astronomical time series analysis. II - Statistical aspects of spectral analysis of unevenly spaced data. *Astrophysical Journal*, 263, 835-853. doi: 10.1086/160554
- Schulze, H. (2016, June). Frequency-Domain Simulation of the Indoor Wireless Optical Communication Channel. *IEEE Transactions on Communications*, 64(6), 2551-2562. doi: 10.1109/TCOMM.2016.2556684
- Serafimovski, N., Han, C., Berner, S., Weszely, T., Afgani, M., Haas, H., & Purwita, A. (2020). *TGbb common PHY mode and LC HE PHY mode center*

- frequency discussion.* <https://mentor.ieee.org/802.11/dcn/20/11-20-1162-00-00bb-tgbb-common-phy-mode-and-1c-he-phy-mode-center-frequency-discussion.pptx>.
- Serafimovski, N., Han, C., Haas, H., Edwards, R., Baur, E., Bazin, S., & Ryan, M. (2019). *TGbb PHY proposal.* <https://mentor.ieee.org/802.11/dcn/19/11-19-1206-01-00bb-proposed-common-mode-phy-for-tgbb.pptx>.
- Serafimovski, N., Han, C., Weszely, T., Videv, S., Purwita, A., Dehghani, M., ... Haas, H. (2019). *Proposal for common-mode mandatory PHY.* <https://mentor.ieee.org/802.11/dcn/19/11-19-1625-04-00bb-proposed-common-mode-mandatory-phy.pptx>.
- Shao, S., Khreishah, A., Rahaim, M. B., Elgala, H., Ayyash, M., Little, T. D. C., & Wu, J. (2014). An Indoor Hybrid WiFi-VLC Internet Access System. In *2014 IEEE 11th International Conference on Mobile Ad Hoc and Sensor Systems* (p. 569-574). Philadelphia, PA, USA.
- Soltani, M. D., Arfaoui, M. A., Tavakkolnia, I., Ghrayeb, A., Safari, M., Assi, C. M., ... Haas, H. (2019). Bidirectional Optical Spatial Modulation for Mobile Users: Toward a Practical Design for LiFi Systems. *IEEE Journal on Selected Areas in Communications*, 37(9), 2069-2086.
- Soltani, M. D., Purwita, A. A., Zeng, Z., Haas, H., & Safari, M. (2019). Modeling the Random Orientation of Mobile Devices: Measurement, Analysis and LiFi Use Case. *IEEE Transactions on Communications*, 67(3), 2157-2172.
- Soltani, M. D., Zeng, Z., Tavakkolnia, I., Haas, H., & Safari, M. (2019). Random Receiver Orientation Effect on Channel Gain in LiFi Systems. In *2019 IEEE Wireless Communications and Networking Conference (WCNC)* (p. 1-6). Marrakesh, Morocco.
- Stefan, I., Burchardt, H., & Haas, H. (2013). Area spectral efficiency performance comparison between VLC and RF femtocell networks. In *2013 IEEE International Conference on Communications (ICC)* (p. 3825-3829).
- Street, A. M., Samaras, K., Obrien, D. C., & Edwards, D. J. (1997). Closed form expressions for baseline wander effects in wireless IR applications. *Electronics Letters*, 33(12), 1060-1062.
- Sugiura, S., Ishihara, T., & Nakao, M. (2017). State-of-the-Art Design of Index Modulation in the Space, Time, and Frequency Domains: Benefits and Fundamental Limitations. *IEEE Access*, 5, 21774-21790. doi: 10.1109/ACCESS.2017.2763978
- Tavakkolnia, I., Soltani, M. D., Arfaoui, M. A., Ghrayeb, A., Assi, C., Safari, M., & Haas, H. (2019). MIMO System with Multi-Directional Receiver in Optical Wireless Communications. In *2019 IEEE International Conference on Communications Workshops (ICC Workshops)* (p. 1-6). Shanghai, China.
- Tessares. (2019). *Opening the way for convergence in the 5G era with MPTCP.* <https://www.tessares.net/papers/>.
- Tomlinson, M. (1971, March). New automatic equaliser employing modulo arithmetic. *Electronics Letters*, 7(5), 138-139. doi: 10.1049/el:19710089
- Tse, D., & Viswanath, P. (2005). *Fundamentals of Wireless Communication*. USA: Cambridge University Press.
- Tsonev, D., & Haas, H. (2014). Avoiding spectral efficiency loss in unipolar OFDM for optical wireless communication. In *2014 IEEE International Conference on Communications (ICC)* (p. 3336-3341). Sydney, NSW, Australia.
- Tsonev, D., Serafimovski, N., Uysal, M., Baykas, T., & Jungnickel, V. (2017). *Light*

- Communications (LC) for 802.11: Link Margin Calculations.* Retrieved from <https://mentor.ieee.org/802.11/dcn/17/11-17-0479-00-001c-lc-tig-link-margin-calculations.docx>
- Tsonev, D., Sinanovic, S., & Haas, H. (2012). Novel Unipolar Orthogonal Frequency Division Multiplexing (U-OFDM) for Optical Wireless. In *2012 IEEE 75th Vehicular Technology Conference (VTC Spring)* (p. 1-5). Yokohama, Japan.
- Turan, B., & Ucar, S. (2017). Vehicular Visible Light Communications. In J.-Y. Wang (Ed.), *Visible light communications* (chap. 7). Rijeka: IntechOpen. doi: 10.5772/intechopen.69536
- Ungerboeck, G. (1982, Jan). Channel coding with multilevel/phase signals. *IEEE Transactions on Information Theory*, 28(1), 55-67. doi: 10.1109/TIT.1982.1056454
- Uysal, M., Miramirkhani, F., Baykas, T., & Qaraqe, K. (2018). *IEEE 802.11bb Reference Channel Models for Indoor Environments.* <https://mentor.ieee.org/802.11/dcn/18/11-18-1582-04-00bb-ieee-802-11bb-reference-channel-models-for-indoor-environments.pdf>.
- VanderPlas, J. T. (2018, may). Understanding the Lomb–Scargle Periodogram. *The Astrophysical Journal Supplement Series*, 236(1), 16. doi: 10.3847/1538-4365/aab766
- Verdu, S. (2002, June). Spectral efficiency in the wideband regime. *IEEE Transactions on Information Theory*, 48(6), 1319-1343. doi: 10.1109/TIT.2002.1003824
- Vieyra Software. (2020). *Physics toolbox sensor suite.* <https://play.google.com/store/apps/details?id=com.christianvieyra.physicstoolboxsuite>. (accessed October 30, 2020)
- Vučić, J., Kottke, C., Nerreter, S., Langer, K., & Walewski, J. W. (2010). 513 Mbit/s Visible Light Communications Link Based on DMT-Modulation of a White LED. *Journal of Lightwave Technology*, 28(24), 3512-3518.
- Wang, J., Jiang, C., Zhang, H., Zhang, X., Leung, V. C. M., & Hanzo, L. (2018). Learning-Aided Network Association for Hybrid Indoor LiFi-WiFi Systems. *IEEE Transactions on Vehicular Technology*, 67(4), 3561-3574.
- Wang, Y., & Haas, H. (2015). Dynamic Load Balancing With Handover in Hybrid Li-Fi and Wi-Fi Networks. *Journal of Lightwave Technology*, 33(22), 4671-4682.
- Wang, Y., Wu, X., & Haas, H. (2017). Load Balancing Game With Shadowing Effect for Indoor Hybrid LiFi/RF Networks. *IEEE Transactions on Wireless Communications*, 16(4), 2366-2378.
- Wei, L., Zhang, H., & Yu, B. (2016). Optimal bit-and-power allocation algorithm for VLC-OFDM system. *Electronics Letters*, 52(12), 1036-1037.
- Weyl, H. (1949). Inequalities between the Two Kinds of Eigenvalues of a Linear Transformation. *Proceedings of the National Academy of Sciences of the United States of America*, 35(7), 408-411.
- Wu, X., Soltani, M. D., Zhou, L., Safari, M., & Haas, H. (2020). *Hybrid LiFi and WiFi Networks: A Survey.*
- Xie, E., He, X., Islim, M. S., Purwita, A. A., McKendry, J. J. D., Gu, E., ... Dawson, M. D. (2019). High-Speed Visible Light Communication Based on a III-Nitride Series-Biased Micro-LED Array. *Journal of Lightwave Technology*, 37(4), 1180-1186.
- Xu, F., Davidson, T. N., Zhang, J.-K., & Wong, K. M. (2006, March). Design of block transceivers with decision feedback detection. *IEEE Transactions on Signal Processing*, 54(3), 965-978. doi: 10.1109/TSP.2005.861779

- Zemax. (2020). *Opticstudio®*. <https://www.zemax.com/products/opticstudio>. (accessed October 30, 2020)
- Zeng, Z., Soltani, M. D., Haas, H., & Safari, M. (2018). Orientation model of mobile device for indoor vlc and millimetre wave systems. In *2018 IEEE 88th Vehicular Technology Conference (VTC-Fall)* (p. 1-6). Chicago, USA.
- Zhang, Z., Xiao, Y., Ma, Z., Xiao, M., Ding, Z., Lei, X., ... Fan, P. (2019). 6G Wireless Networks: Vision, Requirements, Architecture, and Key Technologies. *IEEE Vehicular Technology Magazine*, 14(3), 28-41.
- Zhengguo, S., Yijun, Z., & Yanyu, Z. (2012). The DMT-Based Bit-Power Allocation Algorithms in the Visible Light Communication. In *2012 Second International Conference on Business Computing and Global Informatization* (p. 572-575). Shanghai, China.